Morphological and Structure-Property Analyses of Poly(arylene ether sulfone)-Based Random and Multiblock Copolymers for Fuel Cells

Anand Shreyans Badami

Dissertation submitted to the faculty of the Virginia Polytechnic Institute and State University in partial fulfillment of the requirements for the degree of

Doctor of Philosophy
In
Macromolecular Science and Engineering

James E. McGrath
Richey M. Davis
Eugene G. Joseph
Judy S. Riffle
Garth L. Wilkes

October 15, 2007
Blacksburg, VA

Keywords: proton exchange membrane, sulfonated polymers, molecular weight, block length, high temperature, linkage group

Morphological and Structure-Property Analyses of Poly(arylene ether sulfone)-Based Random and Multiblock Copolymers for Fuel Cells

Anand Shreyans Badami

ABSTRACT

The commercialization of proton exchange membrane (PEM) fuel cells depends largely upon the development of PEMs whose properties are enhanced over current perfluorinated sulfonic acid PEMs. Understanding how a PEM's molecular weight and morphology affect its relevant performance properties is essential to this effort. Changes in molecular weight were found to have little effect on the phase separated morphologies, water uptake, and proton conductivities of random copolymers. Changes in block length, however, have a pronounced effect on multiblock copolymers, affecting surface and bulk morphologies, water uptake, proton conductivity, and hydrolytic stability, suggesting that multiblock copolymer PEM properties may be optimized by changes in morphology.

A major goal of current proton exchange membrane fuel cell research involves developing high temperature membranes that can operate at ~120 °C and low humidites. Multiblock copolymers synthesized from 100% disulfonated poly(arylene ether sulfone) (BPSH100) and naphthalene polyimide (PI) oligomers may be an alternative. At block lengths of ~15 kg/mol they displayed no morphological changes up to 120 °C or even higher. Water desorption was observed to decrease with increasing block length. The copolymers exhibited little to no water loss during a 200 °C isotherm in contrast to random BPSH copolymers and Nafion. A BPSH100-PI multiblock copolymer with large block length appears to have morphological stability and retain water at temperatures exceeding 120 °C, suggesting its candidacy as a high temperature PEM.

A growing number of alternative PEM research efforts involve multiblock copolymer chemistries, but little emphasis is placed on the methods used to couple the oligomers. Fluorinated linkage groups can help increase block efficiency during coupling, but their effect on a PEM is not well-known. The choice of linkage type, hexafluorobenzene (HFB) vs. decafluorobiphenyl (DFBP), appears to have small but observable influences on multiblock copolymers with disulfonated and unsulfonated poly(arylene ether sulfone) oligomers. DFBP linkages promote greater phase separation than HFB linkages, resulting in increased stiffness, decreased ductility, and increased proton conductivity at low humidities. DFBP linkages also promote more surface

enrichment of fluorine, causing changes in surface morphology and slightly increased water desorption, but determining the impact on actual fuel cell performance requires further research.

Author's Acknowledgements

The author must first thank Dr. James McGrath for his guidance and wisdom over the past three years. I am forever indebted to him for asking me to work for him. Deciding to do so was one of the best decisions I have made in my life thus far.

I would also like to thank my committee members, Dr. Richey M. Davis, Dr. Eugene G. Joseph, Dr. Judy S. Riffle, and Dr. Garth L. Wilkes for their continued technical guidance through my doctoral studies and critical review of my work. My dissertation is better as the result of their input and I am confident my future career will be too.

Special thanks are also extended to Steve McCartney of the ICTAS Nanoscale Characterization and Fabrication Laboratory for training me in AFM, SEM, TEM, and microtoming. I am grateful for his patience with me as I ascended the learning curve for each technique as well as his talent for making the innumerable number of hours I spent in the microscopy lab a more enjoyable experience.

Additionally, I must thank my fellow group members and others whose help enabled the completion of the work in this dissertation and beyond:

- Natalie Arnett, Dr. Yanxiang Li, Dr. Hang Wang, Xiang Yu, and especially Hae-Seung (Harry) Lee for synthesizing samples for me to characterize,
- Abhishek Roy and Ozma Lane for valuable discussions about characterization,
- Rachael van Houten for always letting me use her Bunsen burner, and
- Dr. Mehmet Sankir for making my time in Davidson Hall anything but boring.

Finally, I am extremely appreciative of the administrative prowess of Laurie Good and Millie Ryan, both of whom have helped me in a myriad of ways. I thank my family and friends for keeping me sane and reminding me of the important things in life whenever I work too hard. Greatest thanks goes to the Holy Trinity for their abundant love, graces, and blessings. AMDG!

Table of Contents

Table of Figures

Table of Tables

Chapter 1. Literature Review

1.1 Fuel Cells

1.1.1 Definition of a fuel cell

A fuel cell is an energy conversion device that converts the chemical energy of a fuel into electrical energy when needed [1]. In contrast to batteries and some other electrochemical cells, fuel is oxidized at the anode of a fuel cell and oxidant is reduced at its cathode while current is carried between the electrodes by ions in an electrolyte separator. What makes fuel cells different from batteries and other electrochemical cells is that the fuel (e.g. hydrogen, methanol, or methane) and oxidant (e.g. air, oxygen, or hydrogen peroxide) are not housed within the cell, but continuously supplied from an external source. The ideal fuel for a fuel cell is hydrogen and air with byproduct water vapor as exhaust. Under certain conditions, other fuels like methanol and natural gas may be directly converted, but otherwise they must be first reformed to create hydrogen, which requires additional energy and equipment. Each fuel used in a fuel cell has its own electrochemical reactions associated with it. The basic overall reaction of a H_2-O_2 fuel cell (eq. 1) yields a theoretical voltage of 1.229 V.

$$H_2 + ½O_2 \longrightarrow H_2O \quad (1)$$

This reaction is a summary of the reactions that happen at the anode and the cathode of the cell. Equations 2 through 5 describe these individual reactions for acidic electrolytes (the focus of this review).

$$\text{Anode:} \quad H_2 - 2e^- \longrightarrow 2H^+ \quad (2)$$

$$\text{Cathode:} \quad O_2 + 2H^+ + 2e^- \longrightarrow H_2O_2 \quad (3)$$

$$H_2O_2 + 2H^+ + 2e^- \longrightarrow 2H2O \quad (4)$$

$$\text{Overall:} \quad O_2 + 4H^+ + 4e^- \longrightarrow 2H_2O \quad (5)$$

A schematic diagram of a polymer electrolyte fuel cell (PEMFC) is presented in Figure 1.1. Fuel is fed to the anode of the cell while oxygen in the form of air is fed to the cathode. The hydrogen fuel is oxidized upon contacting the anode and dissociates into protons and electrons (eq. 2). The electrons travel from the anode to the cathode via an external circuit, creating an electrical current in the process. Meanwhile, the protons diffuse through the polymer

electrolyte membrane (PEM) from the anode to the cathode. This protonic movement occurs through the hydrated channels within the PEM by either or both of two methods: structure diffusion or vehicular diffusion [2]. In structure diffusion, protons are transported from one water molecule to another through the hydrated regions of the membrane. In vehicular diffusion, protons attach themselves to water molecules by hydrogen bonding and are carried through the membrane by the motion of the water molecule. Once the protons reach the cathode, they react with the electrons and the oxygen from the air in a reduction reaction (eqs 3,4) that generates water and waste heat.

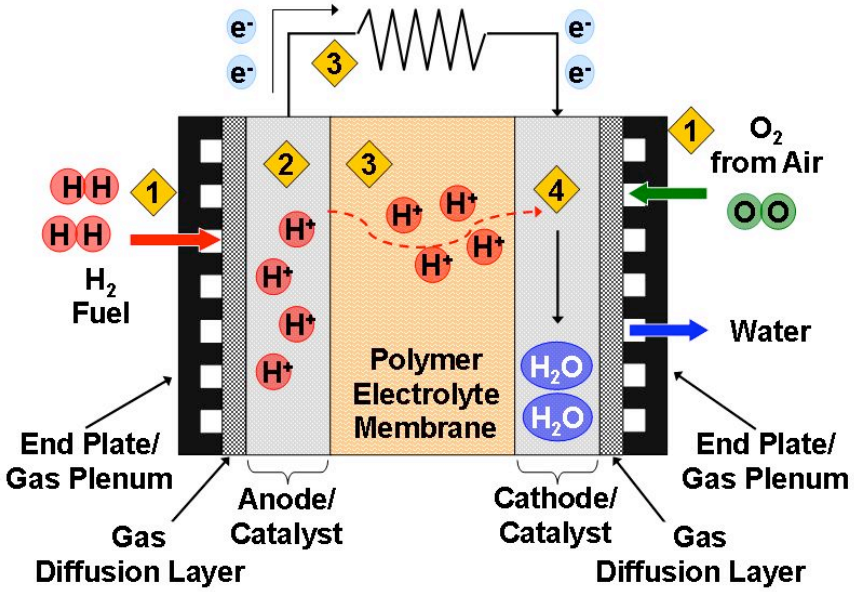

Figure 1.1. Schematic diagram of a polymer electrolyte fuel cell (PEMFC). When reactant gases are fed to the electrodes (1), hydrogen gas is oxidized (2) and its hydrated protons diffuse through the polymer electrolyte membrane while the electrons are conducted through an external circuit to create current (3). Oxygen reduced at the cathode combined with the protons and electrons creates water as a byproduct and waste heat (4).

Essential to the operation and performance of a fuel cell are the design of its components, specifically its electrolyte, the two electrodes between which it is sandwiched, and the catalysts loaded onto the electrodes [1]. The fuel cell electrolyte is an ion-conducting material which separates the anode from the cathode and prevents a short circuit between the electrodes. An electrolyte may be a polymer, liquid, ceramic, or molten salt, depending on the fuel cell (see section 1.1.2). The electrodes of a fuel cell, in addition to providing a stable interface between the electrolyte and the reactant gases, also catalyze the redox reactions at the electrodes and conduct electrons from or to the reaction sites. This makes the "three-phase boundary" between

the electrolyte, electrode, and reactant gas (i.e. porosity of the electrode and wetting of both electrolyte and electrode) an important design parameter to ensure desirable operation and performance. Catalysts are introduced into the electrodes to accelerate both the dissociation rate of the hydrogen at the anode (eq. 2) as well as the decomposition rate of the stable H_2O_2 intermediate generated at the cathode (eqs. 3,4). The H_2O_2 intermediate lowers cell voltage and corrodes the carbonaceous electrodes. The most commonly utilized catalysts in low-temperature fuel cells are platinum or its alloys. As a result of faster reaction kinetics of hydrogen dissociation, the amount of platinum or platinum alloy loaded on the anode (~0.1 mg/cm^2) is considerably less than the amount loaded on the cathode (~0.5 mg/cm^2). Nanostructured platinum and its alloys are often distributed on porous carbon with high surface area to reduce their extremely high cost. Reducing catalyst loadings, improving CO tolerance, and identifying alternative catalysts are ways in which research seeks to lower the cost of low-temperature fuel cells.

Fuel efficiencies of fuel cells are quite high (up to 60-70%) and can be even higher (up to 90%) when the waste heat from the cell is utilized, but the type of fuel used is important [1]. Pure hydrogen gas is the fuel of choice for low-temperature fuel cells because, unlike high-temperature fuel cells which can use hydrocarbon fuels like gasoline or methane directly, low-temperature fuel cells require hydrocarbon fuels to be reformed into hydrogen in a separate process before the fuel can be fed to the anode. Any residual CO_2, H_2S, or CO remaining in the reformed fuel may "poison" the electrode by blocking the platinum catalyst. When the energy required to reform hydrocarbon fuels is considered, the calculated efficiency of the fuel cell is lowered.

Most fuel cell systems are comprised of several components. At the heart of a fuel cell is the membrane electrode assembly (MEA), comprised of the two catalyst-loaded electrodes bonded on either side of the electrolyte. This MEA is sandwiched between porous PTFE-coated carbon paper gas diffusion layers (GDLs) and grooved conductivity collector plates through which the feed gas and exhaust flow. A single fuel cell is comprised of an MEA, two GDLs, and two conductivity collector plates. Since the voltage from a single cell is low, multiple cells are connected in series between bipolar conductivity collector plates (grooved on both sides) to provide sufficient power for various applications. This multiple series of cells is termed a fuel cell stack and will vary by fuel cell type and application. A fuel cell system, or fuel cell power

plant, is comprised of a fuel cell stack as well as several accessory systems [1]. These systems may be responsible for: storing, conditioning, and reforming fuel; thermal management; water supply and removal; system control and instrumentation; and the supply and control of reactants—balancing fuel and air stoichiometry, metering reactant feeds, exhausting reaction products, and controlling pressure across the separator membranes. The system may also have a power conditioning unit which converts the direct current generated by the system into alternating current. All of these components reduce the volume efficiency of the system because the fuel cell stack, where energy conversion occurs, ultimately occupies less than half of the total volume of the system.

1.1.2 Types of fuel cells

The first fuel cell was invented by Sir William Grove in 1839 [3]. It consisted of a series of fifty "cells," each filled with dilute sulfuric acid and two inverted glass tubes, one filled with oxygen and the other with hydrogen. A one-quarter inch wide platinized platina foil ran down the middle of each tube so that when immersed, the acid traveled up the foil by capillary action to expose the acid to the foil surface and the gas within the tube. When the foil within the oxygen-filled tube of each cell was connected to the hydrogen-filled tube of the next cell in series, the device produced enough current to electrolyze water, or in Grove's words, "to effect decomposition of water by means of its composition." Grove noted that "the chief difficulty was to obtain anything like a notable surface of action" (i.e. the "three-phase boundary"). Multiple developments in fuel cell design followed this first innovation, culminating in the fuel cell designs currently used today.

Several types of fuel cells exist today. They are differentiated by electrolyte type and operating temperature (Table 1.1.1). Fuel cells are generally divided into two classes: low temperature (ca. <200 °C) and high temperature (ca. >450 °C) [1]. Acidic or alkaline electrolytes are usually used in low-temperature fuel cells. Temperature is an important factor in fuel cell design and performance [4]. Low temperature operation enables a fuel cell to start up and shut down frequently and quickly, while high temperature operation is preferable for operating with reformed fuels because it improves the kinetics of the electrode reactions within the cell. As temperature increases, the electrodes of a fuel cell become increasingly more tolerant to carbon monoxide (CO) in the fuel and may even be able to use it as a fuel (internal

reforming) at higher temperatures. Higher temperatures eliminate the necessity of noble metal catalysts; however, they place more severe demands on the materials of construction of the cell.

Generally speaking, there are six major types of fuel cells. They are the alkaline fuel cell (AFC), the polymer electrolyte fuel cell (PEMFC) and its variant the direct methanol fuel cell (DMFC), the phosphoric acid cell (PAFC), the molten carbonate fuel cell (MCFC), and the solid oxide fuel cell (SOFC). The main characteristics of each type are summarized in Table 1.1.

Table 1.1. Characteristics of fuel cell types [1]

Type	Operating Temp, °C	Electrolyte	Anode Composition/ Cathode Composition	Fuel	Oxidant
AFC	ambient-90	aqueous KOH	carbon/Pt catalyst (both)	pure H_2	O_2 or air
PEMFC	ambient-90	acidic polymer	carbon/Pt catalyst (both)	pure H_2	O_2 or air
DMFC	25-90	acidic polymer	carbon/Pt catalyst (both)	methanol or methanol-water	O_2 or air
PAFC	180-220 (~200 best)	Phosphoric acid in SiC matrix	carbon/Pt catalyst (both)	pure H_2	O_2 or air
MCFC	350-650 (550 best)	Molten Li_2CO_3 in $LiAlO_2$- ceramic	porous Ni/ porous NiO	H_2 or methane	O_2 or air
SOFC	800-1000 (900)	yttria-stabilized or yttria/calcia-stabilized zirconia support	porous cermet of Ni or Co and yttria-zirconia/ strontia-doped lanthanum-manganite Perovskite	gasoline or methane	O_2 or air

The alkaline fuel cell (AFC) has a long history. In 1933, Sir Francis Bacon began developing a fuel cell that would operate at moderate temperatures and eventually created a hydrogen-oxygen cell with alkaline electrolytes and corrosion resistant nickel-oxide electrodes doped with lithium [5]. This fuel cell was licensed in 1959 by the Pratt and Whitney Aircraft division of the United Aircraft Corporation (currently a subsidiary of United Technologies Corporation) and eventually developed into the fuel cell system used by the command and

service modules of the U.S. Apollo space program [4, 6, 7]. This device operated at higher alkaline (KOH) concentration (~85%), higher temperature (260 °C), and lower pressure (around atmospheric) than Bacon's cell. Lower pressures were possible because of structural improvements to the porous nickel anodes and lithiated nickel oxide cathodes. Over time, the electrodes in this cell were improved by bonding noble metals (Pt/Pd anodes and Pt/Au cathodes) to Ag-plated Ni screens with PTFE, which creates a more stable electrode/electrolyte/gas interface. Lower temperature versions of the AFC are still used on NASA's Space Shuttle Orbiter missions. This pressurized hydrogen oxygen fuel cell yields a high specific power and energy density [4]. Several electrocatalysts can be used in the AFC, including non-noble metals at higher temperatures. The main disadvantage of the AFC is that it cannot be used with air or reformed fuel because carbon dioxide reacts with the alkaline electrolyte. Consequently, there is very little interest in commercializing this fuel cell.

The polymer electrolyte fuel cell (PEMFC) was the first fuel cell used in a practical application [4]. It was invented by William Grubb at General Electric (GE) in 1955 [8, 9]. This low-temperature fuel cell employed a hydrocarbon-based polymer-electrolyte membrane of polystyrene-divinylbenzene sulfonic acid cross-linked with a fluorocarbon film. These membranes had limited lifetimes within the fuel cell apparently because of the oxidative degradation of the C-H bonds in the membrane, especially the α-H sites of functional group attachment. An additional deficiency of the PEMFC was the high loadings of platinum catalyst required. GE developed PEMFC technology in spite of these drawbacks, resulting in PEMFC power plants that powered the U.S. Gemini space modules from 1962. The current polymer electrolyte standard for the PEMFC is Nafion®, a perfluorinated ionomer which maintains stability up to 100 °C (see section 1.2.2). The electrodes of the cell are formed in a thin layer on either side of this polymer electrolyte membrane (PEM) [1]. Catalyst loadings in the electrodes are ~0.1 mg/cm^2 at the anode and ~0.5 mg/cm^2 at the cathode.

A PEM must adsorb water (20-40%) in order to efficiently conduct protons [1]. Proton conduction is made possible when adsorbed water solvates the protons on the acidic groups of the polymer chains within the membrane, making water management in the membrane an important design parameter for PEMFC performance. Conducted protons carry water along with them (osmotic drag) as they diffuse through the PEM. Water is also formed at the cathode during operation, creating a water gradient across the cell. Although this water gradient causes

back-diffusion, the anode must still be humidified during cell operation at high current to prevent its dehydration. Additionally, water must be removed from the cathode to prevent flooding.

Much research is currently focused on commercialization of PEMFCs [4]. The challenges that must be surmounted to achieve this goal include reducing membrane and catalyst costs, effective management of water and heat, and reducing catalyst susceptibility to carbon monoxide and carbon dioxide poisoning from reformed fuels. The cost of a PEMFC stack can be reduced by reducing the amount of expensive construction materials in the stack (e.g. noble metal catalysts, perfluorinated membranes, bipolar plates) and improving the cell performance.

Direct methanol fuel cells (DMFCs), low-temperature fuel cells which have polymeric electrolyte membranes and operating temperatures similar to PEMFCs, oxidize liquid fuel directly at the anode, eliminating the need for reforming hydrocarbon fuel into hydrogen gas [1]. Typically, methanol or a solution of methanol and water are used as the fuel. Anticipated commercial applications of DMFCs are portable electronic devices (e.g. notebook computers, cellular phones) and refueling the devices would entail replacement of a liquid fuel-filled cartridge. DMFC anode electrodes are loaded with platinum-ruthenium catalysts (1-3 mg/cm^2) to prevent formation of a stable formic acid intermediate at the electrode. Solubility of methanol in water is a problem because the methanol can permeate the PEM and oxidize at the cathode, lowering the cathode voltage and overall efficiency of the cell. The voltage of an average DMFC is ~0.5 V at 400 mA/cm at 60 °C [1].

The phosphoric acid fuel cell (PAFC) is a high-temperature fuel cell which uses concentrated phosphoric acid contained by a SiC matrix separator as its electrolyte and operates close to 200 °C [1]. Conductivity drops at temperatures below 150 °C and the phosphoric acid becomes volatile and decomposes above 200 °C. The high PAFC operating temperature increases CO tolerance (up to 1.5% CO), promotes H_2O_2 decomposition, and allows the hot H_3PO_4 electrolyte to reject the water vapor generated at the cathode. Electrodes consist of platinum and platinum alloy catalyst on carbon black support and polymer (PTFE) binder on a 90% porous (pores from 3-50 μm to 0.0035 μm) carbon paper backing. Catalyst loadings are ~0.1 mg/cm^2 at the anode and ~1 mg/cm^2 at the cathode. The PAFC is commonly used in energy storage and its technology is only a few decades old. The Team to Advance Research on Gas Energy Transformation (TARGET) program focused on the task in the late 1960s and early 1970s, ultimately producing 40 PAFCs, but natural gas supply problems curtailed future efforts

by the program [4]. Research continued through the 1970s and 1980s into all types of fuel cell power plants with multiple successes culminating in the first commercial power plant, the 200 kW PC25^{TM} in 1992 [4].

The molten carbonate fuel cell (MCFC) is a high temperature fuel cell (~560 °C) used for energy storage [1, 4, 7]. Its high temperature eliminates the need for noble metal catalysts and allows its waste heat to be used for cogeneration. At the same time, the high temperature creates concerns with the electrodes: electrode structure distortion, dissolution of NiO catalyst, and changes in pore size distribution. Pore size distribution is the only way to balance pressure and control the electrolyte/electrode/gas reaction interface. Electrolyte creep and seal stability are also concerns with MCFCs. Current research is focused on addressing the problems of cathode dissolution, hardware corrosion, and low power density. A typical MCFC at 600 °C operates at 150 mA/cm^2 at 0.8 V.

The solid oxide fuel cell (SOFC) is a high-temperature fuel cell (900 °C), which allows for direct and quick reforming of almost any fuel in-situ, fast electrode kinetics without noble metal catalysts, impurity tolerance, and high grade waste heat useful for cogeneration [1]. The same high temperature operation also results in stringent materials requirements and consequent high fabrication costs. One of the main areas of current research into SOFCs is reducing their operating temperature [7].

Despite the array of fuel cell types, not all of them are suitable for general consumer applications. The two types identified as most promising for widespread consumer use are the PEMFC (for high power applications like automobiles and stationary power) and the DMFC (for low power applications like portable electronic devices (i.e. cell phones, laptop computers, etc.). Consequently, the remainder of this review will focus on the structures, properties, and characterization of ionomer membranes for use in these two fuel cell types, particularly the PEMFC.

1.2 Proton Exchange Membranes (PEMs) for Polymer Electrolyte Fuel Cells (PEMFCs)

1.2.1 PEM characteristics

There are several characteristics crucial to the success of a PEM, whether it is designed for use in stationary, automotive, or portable power applications. These common characteristics

include: low fuel and oxidant permeability, ability to minimize water transport caused by electro-osmosis and water diffusion, minimal conductivity of electrons, high conductivity of protons, oxidative and hydrolytic stability, good mechanical properties when wet or dry, the capacity to be fabricated into a membrane electrode assembly (MEA), and low cost [10]. Fuel permeability and water management are especially critical for PEMs in DMFCs because dilute methanol ($\leq$1 M solution) is used as the source of protons. If the membrane is permeable to the methanol fuel, the methanol will diffuse to the cathode and oxidize, lowering cell efficiency. Excessive water transport can cause flooding at the cathode, reducing catalyst and cell efficiency. Water management is important to consider because nearly all PEM materials depend upon high amounts of absorbed water hydrating their acid groups to conduct protons. Proton conductivity is proportional to the concentration of ion conducting units (often sulfonic acid) in the polymer membrane, often referred to as ion exchange capacity (IEC) with units of milliequivalents of ion conductor per mass of dry polymer (mequiv/g). Ion conductor concentration is also expressed as equivalent weight (EW) where EW = 1000/IEC with units of grams of polymer per equivalent. Increasing the IEC of a membrane increases both its proton conductivity and the amount of water absorbed by the membrane, termed its "water uptake." Water uptake is reported as a mass fraction, mass percent, or number of water molecules per acid site (λ). The water uptake of a membrane affects not only its water transport, but also its mechanical properties. Adsorbed water lowers the membrane's glass-transition temperature (T_g) and modulus and induces swelling. A membrane must have sufficient ductility in the wet and dry states to be bonded to electrodes and made into the MEA of a fuel cell; dissimilarites between the mechanical properties (e.g. swelling) of the different ionomeric polymers on either side of the membrane-electrode interface pose a challenge for MEA fabrication and operation. Finally, the lower the cost of a PEM, the easier it will be to commercialize it. Not all of the ideal values for these PEM characteristics have been quantified. A few have been specified as targets for the year 2010 by the Department of Energy's High Temperature Membrane Working Group (Table 1.2) [11].

Table 1.2. Target values for some PEM characteristics [11]

Characteristic	Target value for 2010
Proton Conductivity @ 25% RH	
at 120 °C	0.100 S/cm
at room temperature	0.070 S/cm
at -20 °C	0.010 S/cm
Oxygen Crossover	2 mA/cm^-2
Hydrogen Crossover	3 mA/cm^-2
Cost*	$5/kW

*anticipating mass manufacturing of 500,000 stacks

1.2.2 Nafion®: Current PEM standard

The current PEM standard for commercial use is Nafion®, a poly(perfluorosulfonic acid) random copolymer manufactured by the E. I. DuPont Company [10, 12]. While the specific synthetic scheme has not been reported, the copolymer is known to be generated by a free radical initiated copolymerization of tetrafluoroethylene (TFE) and unsaturated perfluoroalkyl sulfonyl fluoride, a perfluorinated vinyl ether comonomer (Figure 1.2) [13, 14].

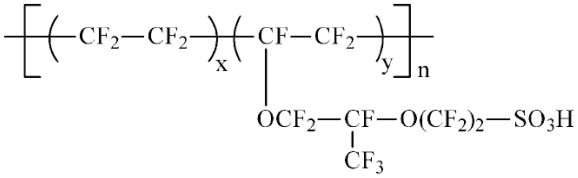

Figure 1.2. Structure of Nafion®, a poly(perfluorosulfonic acid) random copolymer. Molar fractions of comonomers are represented by x and y [10].

The crystallizable TFE backbone sequence is hydrophobic and comprises around 87 mol% of the copolymer in 1100 EW Nafion. Adjusting the ratio of the two comonomers should enable the ion concentration of the membrane (IEC) to be varied. A series of equivalent weights of Nafion were once manufactured, but the only Nafion membranes currently available appear to be 1100 EW in 2, 5, 7, 10 mil thicknesses (Nafion 112, 115, 117, and 1110, respectively). Nafion 1100 EW swells to a moderate degree in water and yields high proton conductivity. Its thicker films (e.g. Nafion 117) are used in DMFCs to reduce methanol crossover while its thinner films are utilized in hydrogen/air PEMFCs to reduce ohmic losses incurred by the resistance of the membrane [10]. The molecular weight of Nafion is not generally reported, but has been suggested to be 10^5 to 10^6 g/mol. Its precise molecular weight is difficult to determine because

Nafion forms a fine dispersion, not a true solution, when dissolved in alcohol/water mixtures [15]. These dispersions are extremely useful in creating catalyst electrodes for MEAs.

Nafion membranes are prepared in a two-stage process [12]. In the first stage, sheets of the desired membrane thickness are extruded from Nafion's thermoplastic sulfonyl fluoride precursor (having $-SO_3F$ groups). This precursor possesses crystallinity similar to but less than that of polytetrafluoroethylene (PTFE) homopolymer and after extrusion displays a small degree of anisotropy from microstructural orientation in the machine direction. In the second stage, the extruded sheets are immersed in a concentrated base and then aqueous acid solution to yield the $-SO_3H$ form of the ionomer. This final form of the ionomer possesses a clustered-ion morphology in addition to the crystalline morphology of its extruded precursor (the morphology of Nafion is discussed in greater detail in section 1.3.4). This morphology is different than that of "recast" membranes made by drying Nafion dispersions because crystallinity is lost during recasting [16].

Nafion possesses several desirable characteristics for PEM use. It displays much better oxidative stability in a PEMFC (up to 100 °C) than its polystyrene-divinylbenzene sulfonic acid membrane predecessor. The primary reason is because Nafion is essentially a fully fluorinated polymer. Its C-F bonds are much stronger than C-H bonds, resulting in greater stability [7]. Nafion's proton conductivity and mechanical strength also qualify it for use in low temperature PEMFCs.

Despite its positive attributes, Nafion is disadvantageous in several ways [10]. First, its synthesis is problematic because the perfluorinated comonomer is both costly ($600-700/m^2) and limited in availability and tetrafluoroethylene copolymerizations can pose safety concerns. Second, Nafion membranes display some undesirable properties at some conditions. For example, Nafion displays poor proton conductivity at low hydration levels and reduced conductivity above 80°C, a moderate glass-transition temperature, low modulus and mechanical strength at higher temperatures, and a high level of methanol crossover (reducing utility in DMFCs). As a consequence of the room for improvement upon Nafion PEMs, much research has gone into creating a variety of alternative polymers for PEMFC membranes besides Nafion. A detailed review of every type of alternative polymer is beyond the scope of this review, however. The interested reader is directed to recent reviews of alternative membranes in the literature [10, 17, 18].

1.2.3 Poly(arylene ether sulfone) copolymers

Wholly aromatic polymers are anticipated to be promising alternatives for high performance PEMs because of their expected stability as fuel cell membranes, ease of processing, availability, and ability to be easily be synthesized in a variety of chemical compositions [10]. A subset of this group of polymers which is especially attractive for PEM use is poly(arylene ether) copolymers, which includes poly(arylene ether sulfone), poly(ether ether ketone), and their derivatives. Many researchers have investigated the syntheses of these polymers [19] and their candidacy as alternative PEMs stems from their oxidative and hydrolytic stability in extreme conditions as well as the multitude of chemical structures (including fluorination) that can be imparted to them during synthesis (Figure 1.3) [10].

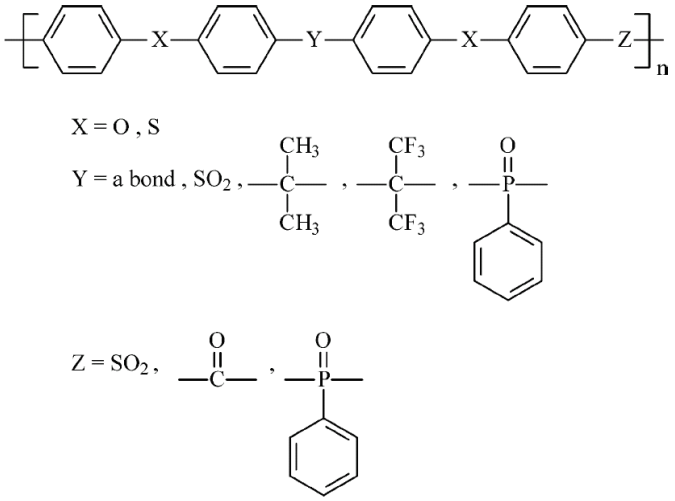

Figure 1.3. Possible chemical structures of poly(arylene ether) random copolymers. Reprinted with permission from [10]. Copyright 2004 American Chemical Society.

Active proton exchange sites must be added to poly(arylene ether)s to make them useful for PEM applications. The two ways this is done are postsulfonation of polymers and direct copolymerization of sulfonated monomers. Aromatic polymers are most frequently sulfonated via electrophilic aromatic sulfonation (postsulfonation) using one of several sulfonating agents: chlorosulfonic acid, sulfur trioxide (or its complexes), sulfuric acid, or fuming sulfuring acid. Noshay and Robeson [20] were among the first to investigate the postsulfonation of poly(arylene ether sulfone)s by attaching sulfonic acid groups to the polymers via modification reactions. Genova-Dimitrova et al. [21] demonstrated that the choice of sulfonating agent has a marked effect on the level of sulfonation during postsulfonation. They compared the postsulfonation of

bisphenol A-based poly(sulfone) using two different sulfonating agents: chlorosulfonic acid ($ClSO_3H$), a strong sulfonating agent, and its milder derivative, trimethylsilylchlorosulfonate ($(CH_3)_3SiSO_3Cl$). It was observed that the sulfonation reactions using chlorosulfonic acid were inhomogeneous and sometimes resulted in some chain cleaves of the polymer while the reactions with trimethylsilylchlorosulfonate were homogeneous and did not result in cross-linking or polymer degradation. The milder sulfonating agent was very inefficient, however, yielding sulfonation levels no higher than 0.85 even when using a 300% excess. In general, the utility of postsulfonation reactions is usually limited because the reactions commonly induce side reactions, degrade the polymer backbone by cross-linking and/or chain scission, and do not enable the ultimate location and concentration of sulfonic acid groups to be manipulated precisely.

Direct copolymerization of sulfonated monomers is more advantageous than postmodification reactions for several reasons. First, sulfonated copolymers synthesized by direct copolymerization display higher acidity and are more stable than postsulfonated polymers because of the location of their sulfonic acid groups. Sulfonation, an electrophilic substitution reaction, entails sulfonic acid groups preferentially reacting with electron-donating substituents. Consequently, this results in a sulfonic acid group randomly bonding at the ortho position of the electron-rich aromatic ether bond in post-sulfonation reactions (Figure 1.2.3). At most, only one sulfonic acid group reacted per repeat unit for bisphenol A-based systems subjected to post-sulfonation reactions. Direct copolymerization of sulfonated monomers, on the other hand, yields repeat units with two sulfonic acid groups precisely bonded at the electron-poor meta position of the deactivating sulfonyl group (Figure 1.4), thus increasing acidity and molecular stability. The second advantage of direct copolymerization is that it allows sulfonated copolymers to be synthesized in various molecular weights, so that the mechanical strength of the copolymers can be tuned.

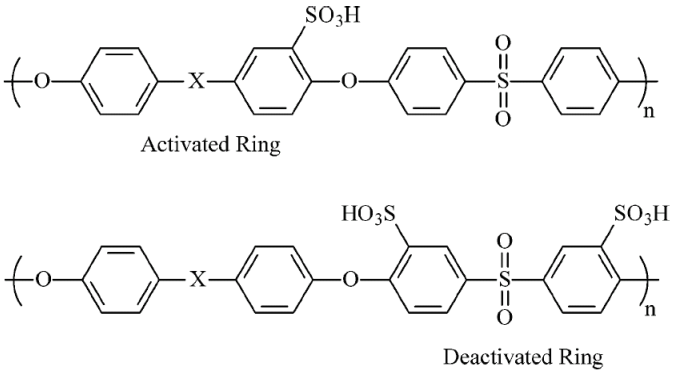

Figure 1.4. Locations of sulfonic acid groups on poly(arylene ether sulfone) repeat units attached by post-sulfonation (top) and direct copolymerization (bottom). Reprinted with permission from [10]. Copyright 2004 American Chemical Society.

The method of direct copolymerization evolved more recently than that of post-sulfonation. The metal salt of the aromatic sulfonic acid monomer utilized in direct copolymerization was first reported by Robeson and Matzner [22] as a flame retarding additive for polyarylates. Limited details of the synthesis, purification, and characterization of sulfonated 4,4'-dichlorodiphenylsulfone were reported a decade later by Ueda et al. [23]. Modifications to this synthesis procedure were made by the McGrath group (Figure 1.5) [24] and the resulting monomer was used in the direct copolymerization of poly(arylene ether sulfone) copolymers of various levels of sulfonation (Figure 1.6) [10].

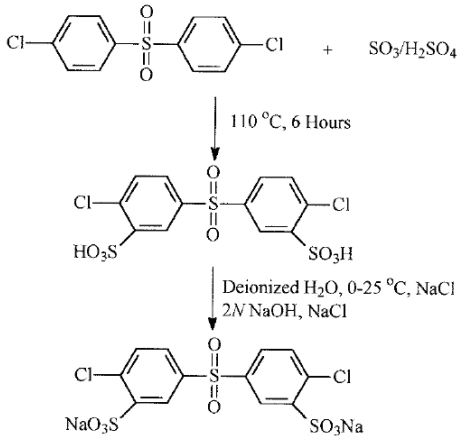

Figure 1.5. Synthetic scheme for 3,3'-disulfonated 4,4'-dichlorodiphenyl sulfone and its sodium salt [24]. Reprinted by permission of John Wiley & Sons, Inc.

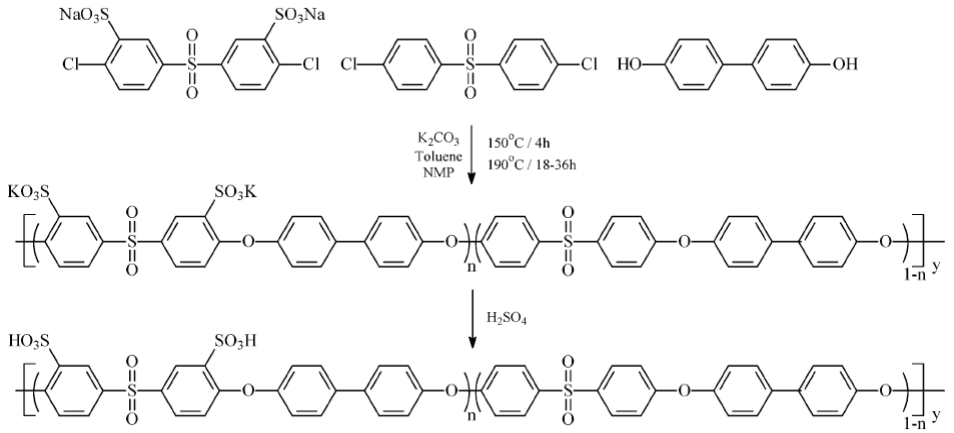

Figure 1.6. Synthetic scheme for direct copolymerization of wholly aromatic sulfonated poly(arylene ether sulfone), BPSH, where *n* equals mol% disulfonation. Reprinted with permission from [10]. Copyright 2004 American Chemical Society.

The poly(arylene ether sulfone) (BPSH) copolymers in Figure 1.2.5 are synthesized in the potassium salt form of the 3,3'-disulfonated 4,4'-dichlorodiphenyl sulfone to exploit the increased stability of the sulfonic acid salt. Solvent-cast films of these copolymers are converted to the sulfonic acid form by immersion in sulfuric acid. Two acidification methods have been evaluated for these membranes [25]. The first, method 1, entails immersion in sulfuric acid at 30 °C for 24 h followed by immersion in deionized water at 30 °C for 24 h. The second, method 2, involves immersion in sulfuric acid at 100 °C for 2 h, then immersion in deionized water at 100 °C for 2 h. Both acidification methods result in hydrophilic/hydrophobic microphase separation within the membrane of the ionic domains and nonionic domains and this phase separation (as well as proton conductivity and water uptake) increases with level of disulfonation. However, method 2 imparts to BPSH membranes greater water uptake, higher proton conductivity, and less temperature dependence on proton conductivity [25]. Kim et al. [26] observed that this is because hydrothermal treatment of a sulfonated copolymer at elevated temperatures below its fully hydrated glass transition temperature (T_g) causes an irreversible change to a more "open" morphology (greater connectivity of hydrophilic domains). Hydrothermal treatments above the hydrated T_g will cause decreased water uptake and proton conductivity because phase mixing is induced.

Variations of BPSH random copolymers can be synthesized by varying the monomers used in the synthesis, enabling specific tailoring of properties like IEC and water uptake. Harrison et al. [24] synthesized several series of sulfonated poly(arylene ether sulfone)

copolymers with controlled degrees of sulfonation by polymerizing either 3,3'-disulfonated 4,4'-dichlorodiphenyl sulfone or 3,3'-disulfonated 4,4'-difluorodiphenyl sulfone with one of four bisphenols: 4,4'-bisphenol A, hexafluoroisopropylidene bisphenol (6F bisphenol A), 4,4'-biphenol, and hydroquinone (Figure 1.7).

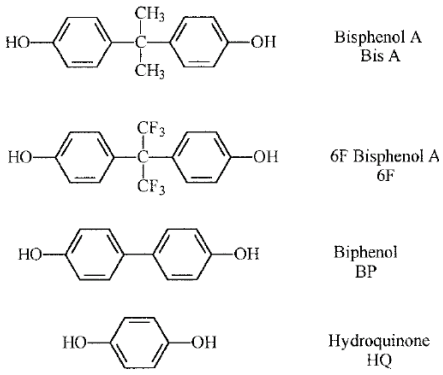

Figure 1.7. Bisphenol structures investigated by Harrison et al. [24]. Reprinted by permission of John Wiley & Sons, Inc.

IEC and water uptake were observed to change with bisphenol structure, with hydroquinone yielding the highest IEC and water uptake and 6F bisphenol A yielding the lowest of both. Both 4,4'-bisphenol A and 6F bisphenol A introduce aliphatic groups into the backbone of BPSH-xx molecules not present with the other two bisphenols. The aliphatic groups of these monomers not only lower the thermooxidative stability of the molecules, but they also impart kinks to the chain. This change in chemistry affects the stiffness (glass transition temperature, T_g) and packing behavior of the molecules, which ultimately affects their morphology. Additionally, copolymers synthesized with 6F bisphenol A are of interest because the increased surface fluorination of these copolymers may lower water uptake, reduce swelling and enhance both the adhesion and electrochemical compatibility with electrodes based on Nafion. 6F bisphenol A comonomers may help to improve the balance between high protonic conductivity and low water uptake and swelling.

In addition to tailoring membrane properties by varying BPSH copolymer structure, efforts have been made to create multiblock copolymers based on BPSH oligomers. For example, Ghassemi et al. synthesized multiblocks of hydrophobic BPSH-00 and hydrophilic sulfonated benzoyl substituted polyphenylenes [27] as well as multiblock copolymers containing hydrophobic perfluorinated poly(arylene ether) and hydrophilic disulfonated BPSH-100 oligomers [28]. Multiblock copolymers containing hydrophilic disulfonated BPSH-100 have

also been synthesized with hydrophobic poly(2,5-benzophenone) [29] and naphthalene polyimide [30]. The goal in such syntheses is to combine the positive membrane properties of BPSH with the positive characteristics of a second polymer to create a membrane whose properties are an amalgam of both (e.g. an improved balance of high proton conductivity with low water uptake and swelling). Since membrane performance properties are influenced by the supramolecular structure of the ion-containing copolymers comprising the membrane, it is important to understand the structure, morphology, and physical properties of ionomers.

1.3 Ionomers

Ionic polymers are a class of macromolecules which are considered a cross between covalent polymers and ionic salts because they have properties and structural features characteristic of both [31]. Ionic polymers possess both partially or wholly covalent (directional) bonds and ionic (non-directional) bonds [31]. Ionomers, polymers which contain a small amount of ions in a matrix of relatively low dielectric strength [32], are a subset of ionic polymers which do not contain many carboxylate groups and are structurally similar to organic polymers [31]. It is very probable that successful ionomers for PEM usage will be copolymers (polymers containing two or more different monomers), considering that ion-containing homopolymers adsorb too much water to be dimensionally and mechanically viable.

1.3.1 Copolymer architecture

Copolymer architecture can be classified into distinct categories by the way repeating units are arranged along a polymer chain. Random copolymers have their different monomers arranged in a random sequence along their chain. Many random copolymers are actually statistical copolymers because the monomers react with each other following a statistical law according to the reactivities of the monomer chemistries and the synthesis method [33]. Block copolymers are comprised of one or more continuous linear sequences of each repeat unit (blocks) and can be subdivided into diblock, triblock, multiblock, graded block, and star block copolymers, depending on the number and arrangement of blocks. Graft copolymers consist of a backbone of one repeat unit type with branches of a one or more different repeat unit types.

1.3.2 Phase separation

The short sequence lengths of repeating units in random copolymers typically inhibit them from displaying more than one morphological phase [34]. However, random copolymers will phase separate if their component phases are extremely dissimilar in nature as is the case for many proton-conducting polymers with hydrophobic hydrocarbon backbones and hydrophilic pendant ionic groups [35]. When these ionomers phase separate, their polar ionic groups tend to aggregate in assumedly spherical clusters dispersed in the continuous nonpolar matrix of the hydrocarbon substituents. To better understand the dynamic nature of cluster formation and supermolecular structure resulting from phase separation in ionomers, Mauritz and Hopfinger suggest that it may be helpful to envision ionomeric materials as block copolymers [36]. A summary of phase separation of non-ionic block copolymers is given below. While it is helpful to envision ionomeric materials as block copolymers, it is also important to realize that ion-containing copolymers do not perfectly obey phase separation theory for block copolymers. This issue will be discussed in greater detail in section 1.3.2.2.

1.3.2.1 Phase separation in non-ionic block copolymers

Diblock copolymers with chemically different A and B blocks may self-assemble into a number of different morphologies by the process of microphase separation [34, 37]. Microphase separation occurs when incompatible blocks of repeat units are covalently bonded with each other and forced to coexist. The segments obey the Gibbs free energy relationship (eq 6):

$$\Delta G = \Delta H - T\Delta S \tag{6}$$

Negative free energy (ΔG) values will induce mixing, while positive values induce separation. The entropy of mixing (ΔS) per unit volume of dissimilar polymers is very small, especially as block molecular weight increases. Consequently, a slightly positive enthalpy of demixing (ΔH) in the form of minor chemical or structural differences between A and B blocks is enough to produce a positive free energy and drive the blocks to separate from each other into distinct phases. The degree to which the A and B blocks will be compatible can be quantified by the Flory-Huggins χ parameter, χ_{AB}, which describes the non-ideal part of the mixing free energy [37]:

$$\chi_{AB} = (z/kT)[\varepsilon_{AB} - \tfrac{1}{2}(\varepsilon_{AA} + \varepsilon_{BB})] \tag{7}$$

where z = the number of nearest-neighbor monomers to a copolymer configuration cell

kT = thermal energy (Boltzmann's constant multiplied by temperature)

ε_{AB} = the interaction energy per monomer between A and B monomers

ε_{AA} = the interaction energy per monomer between A and A monomers

ε_{BB} = the interaction energy per monomer between B and B monomers

When χ_{AB} is negative, the free energy of mixing is lowered and miscibility of A and B monomers is favored. When χ_{AB} is positive, a net repulsion exists between A and B monomers. Typically, χ_{AB} is positive and less than one for dissimilar monomer pairs having no specific interactions (charges, hydrogen bonding, etc.). Miscibility between monomers increases with temperature because χ_{AB} varies inversely with temperature.

Complete macrophase separation (coexistence of separately distinct phases) does not occur in block copolymers because the entropic forces from the covalent linkages between the blocks counterbalances the thermodynamic (enthalpic) forces driving separation. As the A and B blocks repel each other, the coiled chains linking them uncoil, reducing entropy as they adopt more extended configurations. This generates an entropic restoring force which limits phase separation between A and B blocks to less than macroscopic dimensions. This "elastic" restoring force can be quantitatively expressed as [37]:

$$\Delta G_{elastic} = 3kTR^2/(2Na^2) \tag{8}$$

where *R* is the extended distance of a chain of *N* monomers and *a* is a monomer size scale similar to a statistical segment length that depends on the local structure of the polymer chain. The sum of free energies contributing to the balance of repulsive and elastic energies per copolymer chain of a lamellar phase can be written as [37]:

$$\Delta G_{lamellar}/kT = 3(\lambda/2)^2 / (2Na^2) + (\gamma_{AB}/kT)\Sigma \tag{9}$$

where γ_{AB} is the surface tension at the A-B interface and Σ is the interfacial area per chain. Classic polymer interface theory defines $\gamma_{AB} = (kT/a^2)\sqrt{(\chi_{AB}/6)}$. Invoking a volume constraint of $\Sigma\lambda/2 = Na^3$, it can be shown that $\lambda \approx 1.03a\,\chi_{AB}^{1/6}N^{2/3}$ and $\Delta G_{lamellar} \approx 1.19(\chi_{AB}N)^{1/3}$. The free energy per chain in a disordered phase in which the A and B blocks of a copolymer are homogeneously mixed can be approximated as [37]:

$$\Delta G_{disorder}/kT = \chi_{AB}f_Af_BN = (\chi_{AB}N)/4 \tag{10}$$

where f_A f_B are the mole fractions of the A and B blocks, respectively. The order-disorder phase boundary can be determined by equating $\Delta G_{lamellar}$ to $\Delta G_{disorder}$, which yields a value of $\chi_{AB}N = 10.4$ for the order-disorder transition (ODT). This agrees very closely with the more accurate mean-field estimate obtained by Ludwik Leibler [38] of 10.5. Consequently, no phase separation is predicted for symmetric diblock copolymers with low molecular weight or chemically compatible blocks ($\chi_{AB}N < 10.5$), but symmetric diblock copolymers with strongly incompatible blocks or high molecular weight ($\chi_{AB}N > 10.5$) are predicted to microphase separate into lamellae.

The most recent advance in self-consistent mean-field theory (SCMFT) applied to block copolymers was by Matsen and Schick [39-41] who calculated a phase diagram for AB diblock copolymers which compares very well to experimental observations. At values of $\chi_{AB}N > 10.5$ above the ODT, five ordered microphase structures based on varying concentrations or lengths of each block (f_A, f_B) are predicted to have regions of thermodynamic stability. A lamellar (L) phase is stable for virtually symmetric diblocks. For asymmetric diblocks, the block with the smaller volume fraction will form discrete domains within a continuous matrix comprised of the block with the larger volume fraction. Diblocks with moderate amounts of asymmetric composition (i.e. $f_A > ½$ or $f_B > ½$) form thermodynamically stable hexagonally packed cylinder (C) phases. An increase in compositional asymmetry produces a body-centered cubic spherical (S) phase (i.e. $f_A >> ½$ or $f_B >> ½$). The disordered and S phases are separated by a narrow region of close-packed spheres. A narrow, thermodynamically stable bicontinous gyroid (G) phase is also predicted between the L and C phases.

Not all final block morphology obtained experimentally matches the theoretical predictions of Matsen and Schick perfectly [37]. One reason is that their theory assumes that all monomers have statistical segments of equal length (i.e. the monomers occupy lattice cells of identical volume). This is not the case for all monomers, including the styrene and isoprene monomers in the poly(isoprene-styrene) diblock copolymer melts characterized by Khandpur et al. [42]. These copolymer melts from these unequal sized blocks have an asymmetric phase diagram as a result. A second reason for the asymmetry for the experimental diagram is that multiple χ_{IS} parameters may be required to accurately approximate the different free energies required to move an isoprene monomer from an exclusively isoprene environment to an exclusively styrene environment and move a styrene monomer from an exclusively styrene

environment to an exclusively isoprene environment. A third reason for the discrepancy between experimental and theoretical morphology is the existence of long-term psuedostable or transient morphologies that occur experimentally but do not exist in theoretical models because they are not thermodynamically stable. For example, Khandpur et al. [42] observed that a complex phase of perforated layers (PL) was next to the G phase in the phase diagram of their IS diblock phase diagram. This PL phase was later confirmed to not be thermodynamically stable. A schematic diagram of these phases is presented in Figure 1.8. A fourth reason for a difference in experimental phase diagram may be differences in chain topology. Chemically identical blocks organized in different architectures besides linear (e.g. graft, star, etc.) will elicit different phase diagrams than the one described above.

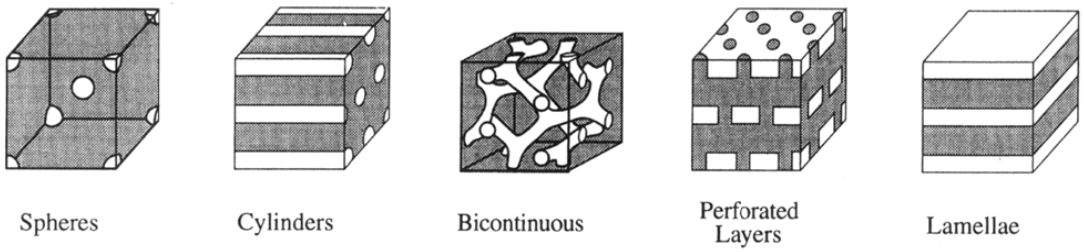

Figure 1.8. Schematic diagram of five different ordered microstructures observed for a series of polyisoprene-polystyrene diblock copolymer. Reprinted with permission from [42]. Copyright 1995 American Chemical Society.

1.3.2.2 Phase separation in block copolymers with specific interactions

The discussion above regards phase separation in block copolymers without any "specific interactions" in excess of the chemical and physical differences inherent to the blocks themselves. However, specific interactions may exist in some copolymers that may cause differences in the final phase separated morphologies [37]. These interactions include hydrogen bonding, ionic charges, and solvent affinity. Copolymers with monomers like urethanes, ureas, and amides that hydrogen bond easily or those with ionic charges will phase separate differently than those mentioned above. Chain mobility will be restricted, lowering the χ_{AB} of the copolymers, making phase separation more difficult. Polymer films cast from solution may also display different phase separation behavior than those cast from the melt. If one block has a greater affinity for the solvent than the other, the copolymer will phase separate differently than if both blocks have an equal affinity for the solvent. This is described in greater detail in section 1.3.3.

More specific details about the factors which govern phase separation in ion-containing block copolymers are extremely difficult to find as the body of literature on this subject is fairly limited. Although synthetic methods enabling the preparation of acrylic-acrylic [43] and styrenic-acrylic [44, 45] types of block ionomers have been in the literature for around two decades, systematic structure-property studies of the phase separation behaviors of these and other systems have remained limited. One thing that has been demonstrated is the how the interdomain distance between ionic domains in phase separated morphologies varies with block length [46, 47]. It would be helpful to know structure-property details about block ionomers because the type of phase separation exhibited by a block copolymer will affect its mechanical and transport properties [34]. This is of special interest for block copolymer films in proton exchange membrane fuel cell applications. The prospect of tailoring the separation of ion-conducting and non-ion-conducting phases within the membrane is a promising approach to increasing proton conductivity.

1.3.3 Morphological effects of sample preparation

In addition to chemical composition, molecular weight, and crystallinity, sample preparation parameters also influence the microphase-separated morphology of a PEM film. Much research has been performed on the phase separation of diblock (and to a smaller degree, triblock) copolymer films. The microdomain structure of a block copolymer film will vary based on the interfacial interactions determined by relative affinities of its blocks to both the substrate and the air surfaces [48-56]. When one block has an affinity for one of the surfaces, it will form domains oriented parallel to the surface [55, 57-60]. If none of the blocks has an affinity for one of the surfaces, the microdomain structure will develop perpendicular to the surfaces [55, 58, 59, 61, 62]. Other methods to achieve perpendicular microdomain structures orientation include varying substrate roughness [63], varying film thickness [60, 64], solvent casting [65], and applying external fields [66]. A gradient combination of parallel and perpendicular oriented domains has also been observed for asymmetric boundary conditions (e.g. non-neutral air and neutral substrate) [55, 59]. Choice of solvent [67-69] will affect film morphology. When block copolymers are dissolved in a solvent for casting, the block with the weakest affinity for the solvent will "precipitate first" as the solvent evaporates, becoming discrete domains within the continuous matrix formed by the second segment which is "expanded" in solution [34]. This

phenomenon is most striking when the two segments are of similar lengths and can be reversed if a solvent with a greater affinity for the first segment is chosen. Shear forces [70-72], and solvent evaporation rate [73] can also be varied to obtain different morphologies for the same polymer film. It is essential to recognize that changes in sample preparation of PEM films may impact their performance properties. For example, the proton conductivity of recast Nafion® 117 is around four orders of magnitude lower than "as received" Nafion® 117, illustrating the importance of understanding the influence of sample preparation and morphology on PEM properties [16].

1.3.4 Morphological models

In the past three decades or so, several molecular models for the microphase separation of polar and non-polar phases of ionomers have been proposed, some exclusively focused on fluorinated ionomers (e.g. Nafion). These models all attempt to predict ion-transport properties and equilibrium ionic selectivities of ionic polymers. All of the models embrace the concept of ionic group aggregation within a polymer matrix and most of them recognize this aggregation allows for swelling by polar solvents and subsequent ionic transport through the resulting ionic domains. The models diverge upon the issue of ionic domain geometry and distribution. Ultimately, however, the usefulness of these models is limited because none of them address the experimentally observed existence of crystallinity in ionomers such as perflorosulfonates (e.g. Nafion). These models, like all structural models of ionomers, fall into one of three categories [74]. The first category, which involves the most creativity, consists of qualitative models that are based on both an interpretation of the current database of structure-property experiments and widely-recognized fundamentals of polymer science. The second category of models is comprised of mathematical models. Utilizing commercially available software, these predictive models propose actual equations that describe the concepts stated in the qualitative models by applying theoretical conformation and chain-packing analyses based on molecular energetics. The third and final category of modeling consists of models which fit experimental data obtained from specific structural characterization techniques like SAXS or SANS to equations specific to the model. The following models reflect some of the most salient theories relevant to ionomers for fuel cell applications.

1.3.4.1 Eisenberg model of multiplets and clusters

In 1970, Eisenberg was the first person to propose a model of ionomer microphase morphology to complement the limited amount of structure-property data in existence for ionomers at that time [32]. This model demonstrates the energetic favorability of ionomer ions to develop a cluster morphology beginning with the aggregation of lower-order multiplets (ion pairs, triplets, quartets, octets, etc.) into clusters stabilized by electrostatic interactions. This condensation of multiplets ultimately causes a deformation in the polymer chains connected to them.

Five critical assumptions form the foundation of Eisenberg's model [32]. First, long-range electrostatic interactions, which can be strong in organic mediums with low dielectric constant, are responsible for driving the aggregation of ion pairs or multiplets. Second, the precise amount of electrostatic energy released when multiplets aggregate into larger clusters will be a function of the dielectric constant of the organic medium and the particular geometry of the ionic cluster. Third, cluster formation deforms the polymer chains, causing a change in entropy-elastic work. The polymer chain segments between ionic groups are assumed to link only nearest-neighbor ionic groups and the conformations of these interionic chains are taken to be Gaussian (statistical). Fourth, destabilization of clusters will occur at some critical temperature, T_c, at which electrostatic forces are in equilibrium with opposing elastic forces. Evidence now exists for a "cluster transition" greater than the glass transition of the polymer matrix, T_g, for several fluorocarbon and hydrocarbon-based ionomers, however, the specifics of cluster rearrangement at this transition temperature are still not completely defined. The fifth and final assumption underlying Eisenberg's model is that half of the sequential ion pairs within a cluster will give rise to "rings" by forming multiplets with each other.

Some of these assumptions fundamental to the Eisenberg model are subject to debate [74]. For example, some ionomers with small ionic comonomer mole fractions may possess a significant degree of crystallinity. Crystallinity inhibits the treatment of chains as having statistical conformations because it seriously restricts long range mobility of chain segments. Despite this fact, however, no theory subsequent to Eisenberg's has accounted for crystallinity. For ionomers with large ionic comonomer mole fractions, interionic chain distances are too short to be modeled using Gaussian statistics. Additionally, ionomer systems may also be too intricate to use the entropy-elastic equation [75] based on purely random coils to model the energy of

chain deformation. While Eisenberg's model has not proven to be the definitive theory of ionomer morphology, it laid an important foundation upon which subsequent theories were built.

1.3.4.2 Cluster model of Hopfinger et al.

Starting with Eisenberg's theory, Mauritz, Hora, and Hopfinger [76] developed a more intricate theory which further expounds upon the molecular energetics of cluster formation and addresses the incorporation of water and mobile ions into the molecular structure. This theory focuses more on molecular detail than any subsequent theory, utilizing molecular and quantum mechanics to calculate molecular parameters. Mauritz et al. [76] used molecular computer simulations to calculate configurational dipole-dipole interaction free energy (F) based on the number and strength of interacting dipoles within a cluster. Assuming the interacting dipoles to be SO_3H or $SO_3^-Na^+$, this model, like Eisenberg's, takes into account both the energy required to deform (assumed) Gaussian chains (elastic deformation energy per dipole; W) and the conformational entropy lost as charged side chains cluster ($\Delta S(n_c)$).

The Hopfinger model considers three different physiochemical states for ionomers: (1) dry, (2) in aqueous solution, and (3) in aqueous solution with mobile ions [76]. When an ionomer is in the dry state, the configurational dipole-dipole free energy is destabilized by the surface tension between the cluster and nonpolar phases (Equation 7):

$$F + 4\pi\varepsilon_0 r^2(n_c) = W + T\Delta S(n_c) \quad (7)$$

where ε_0 is the surface energy per unit area and $r^2(n_c)$ is the cluster radius. When the ionomer (e.g. Nafion) is placed in aqueous solution, water diffuses into the ionic clusters and hydrates the polar groups, forming a hydration shell and the clusters begin to swell. The resulting hydration shell size of a cluster is dependent on a free energy balance between (1) the water-water and water–polar group interactions within the hydration shell and (2) the surface tension at the aqueous-nonpolar interface and the elastic deformation energy required to move the chains aside as the hydration shell grows. Dipolar interactions cause individual hydration shells to aggregate into hydrated clusters (Figure 1.9). The free energy lost by the ejection of water molecules from overlapping hydration shells is offset by water-water interactions between hydration shells and the decrease in overall water-nonpolar interfacial area.

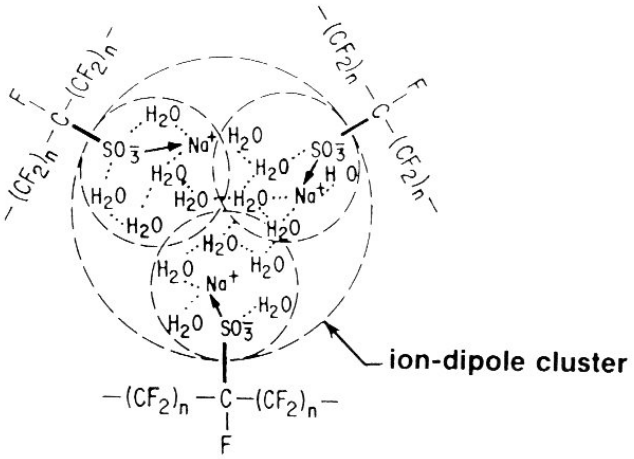

Figure 1.9. Diagram of hydrated ion-dipole cluster formation within Nafion perfluorosulfonate ionomers. Reprinted from [77] with kind permission of Springer Science and Business Media.

When the ionomer is placed in aqueous solution with mobile ions, the type and concentration of the mobile cations will affect both the effective hydration shell dipole and the size of the ion-dipole hydration shell. In this model, ionic clusters with high water content are envisioned as inverse micelles in which anions covalently bound to the nonpolar polymer chains extend into a water phase containing mobile cations [76]. This cluster model is very similar to the spherical inverted micelle model proposed by Gierke [78] (see section 1.3.4.4). To quantitatively apply this morphological model and compare theory to empirical data (e.g. water uptake, tensile modulus, equivalent weight, etc.), Mauritz et al. [76] developed a constraint of four parameters to be used to calibrate the model. These four parameters consisted of an elastic force constant and three packing factors for water molecules either in an aqueous hydration shell, in a hydration shell with a mobile cation, or within a cluster of hydration shells. Mauritz et al. [76] ultimately used the model to predict cluster size and water molecule and ion-dipole concentrations with each cluster as a function of equivalent weight.

This creative model envisioned by Mauritz et al. was unfortunately unable to draw upon the abundance of experimental data from structural studies reported shortly after the model was published. For example, Lowry and Mauritz [79] developed a correction to the cluster theory model of Mauritz et al. based on a four-state ion-counterion hydration model (Figure 1.10). The correction states that ion-hydrate complexes can interchange between four states: (1) ion pairs that are fully dissociated, (2) ion pairs with undisturbed, contacting primary hydration shells, (3)

ion pairs whose outer spheres have complexed, and (4) ion pairs whose inner spheres have complexed.

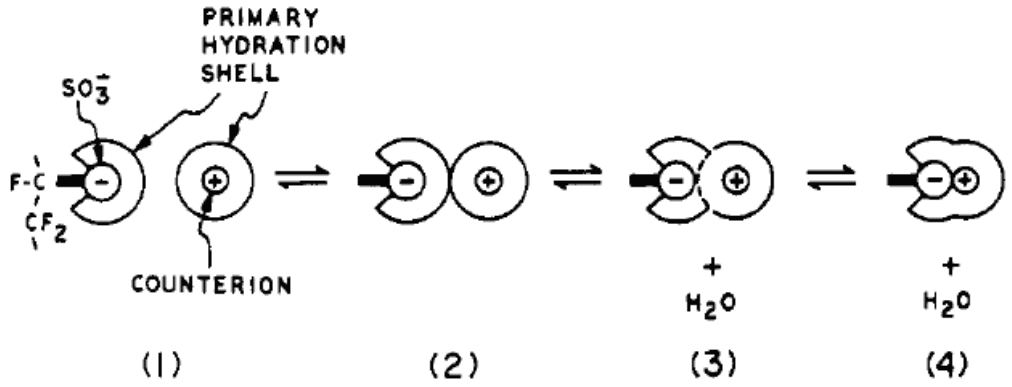

Figure 1.10. Four-state model of the hydration-mediated dissociation equilibrium of Mauritz et al[79]. Each ion-hydrate complex (pair) changes between states at a characteristic rate. Reprinted with permission from [79]. Copyright 1980 American Chemical Society.

Subsequent studies have also drawn into question the assumption of Gaussian coil approximation for the polymer chains between ionic groups with the discovery that Nafion ionomers possess a substantial amount of chain order in their perfluorocarbon phase because closely-packed long side chains are anchored in clusters [80, 81].

1.3.4.3 Forsman's theory of site aggregation

Forsman [82] proposed a lattice-based statistical mechanical model of aggregation in dry ionomers in the melt or in solutions at concentrations greater than the critical overlap concentration. This model assumes four approximations: (1) equal spacing along the chain backbone of interacting repeat units, (2) both the entire molecules and subchains between interacting groups obey Gaussian statistics, (3) there are the same number of repeat units in each cluster, and (4) the *m* repeat units that form each cluster would be nearest neighbors if cluster formation did not occur (Figure 1.11).

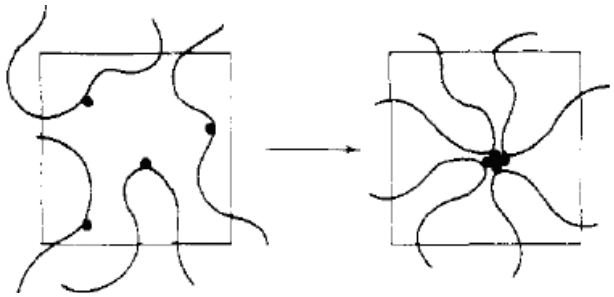

Figure 1.11. Forsman's model of cluster formation of a central repeat unit and its nearest neighbors. Reprinted with permission from [82]. Copyright 1982 American Chemical Society.

The extension of the chains beyond their statistical conformation in the absence of cluster formation is predicted. Rubber elasticity theory is used to calculate the entropy loss incurred by extension of the molecules (ΔS_r) as well as the loss of entropy resulting from confining repeat units to aggregates (ΔS_a). The free energy of cluster formation is also calculated. Calculations from this model reveal that ΔS_a is two to four times larger than ΔS_r.

The approximations upon which this model is based prevent it from being universally applicable to ionomer systems [74]. It cannot be accurately applied to crystalline and hydrated systems because the model does not address these conditions. In addition, this model is not appropriate for modeling perfluorinated ionomers because its Gaussian coil approximation limits its applicability to polymers with low mole fractions of ionic copolymer.

1.3.4.4 Hsu and Gierke's elastic theory of cluster swelling in perfluorinated ionomers

Gierke and coworkers [78, 83] proposed a semiphenomenological elastic theory of cluster swelling in perfluorinated ionomers that assumed the existence of clusters *a priori* and sought to model the equilibrium diameter of hydrated clusters by considering the energetics associated with their growth. In this model the hydrated cluster structure is envisioned as a spherical inverted micelle in which ion exchange sites are found at the interface of a spherical water domain. Multiple inverted micelles are connected by ~10 Å diameter "pores" or tiny channels that enable ion transport (Figure 1.12).

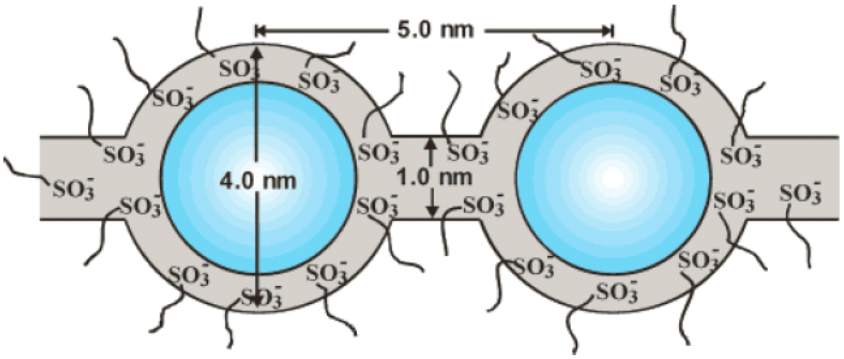

Figure 1.12. Cluster- network model proposed by Gierke for sulfonated Nafion ionomers: hydrated clusters form inverted micelles connected by pores. Adapted from [84] with permission from Elsevier and reprinted with permission from [12, 82]. Copyright 2004 American Chemical Society.

For mathematical simplicity, Hsu and Gierke assume in this model that a dry cluster introduced into an group of fully-hydrated clusters will swell provided that the number of ions within the cluster remains constant [83]. The equilibrium diameter of the cluster in the Gierke model [83] is dependent upon its free energy. This free energy of the hydrated cluster is estimated by assuming a balance between the energy produced by hydrophilic interactions in the cluster interior and surface and the elastic energy required to create volume for the hydrated cluster by deforming the surrounding polymer matrix. Minimizing this free energy yields an expression for the cluster diameter which has been shown to accurately describe cluster diameter in Nafion as cation type, equivalent weight, and water content are varied. For a given equivalent weight, the Gierke model indicates that the exchange sites per cluster, the number of water molecules per exchange site, and the cluster diameter increased linearly with water content [78]. This model was the first one to assign the SAXS maximum for Nafion to regions between clusters and to suggest that solvent swelling may cause minor morphological reorganizations, two ideas that have not been disproven. Although it was not meant to be the quintessential model for Nafion's actual morphology, this cluster-network (or cluster-channel) model has been referenced more often than another other model in the study of perfluorosulfonate ionomers.

Nevertheless, a few limitations are inherent in this theory. First, Hsu and Gierke assume that a dry cluster introduced into a group of fully-hydrated clusters will swell provided that the number of ions within the cluster remains constant. While this assumption simplifies the mathematics of the model, is not consistent with experimental findings. Gierke et al. [78] had already estimated the number of ion exchange groups per cluster based on (a) SAXS data for

Nafion at various water contents and (b) valid assumptions of Nafion's cluster morphology and discovered a linear relationship between the number ion exchange sites per cluster and water content as well as cluster diameter and water content. Additionally, the existence and nature of the interconnecting channels in this model forms the basis of Gierke's model for selective ion transport, but their existence has yet to be substantiated by direct experimental evidence. While Hsu and Gierke offer a thermodynamic explanation for the stability of these channels, they also concede that their approach of applying macroscopic concepts to confirm such tiny channels is questionable.

1.3.4.5 Water sorption isotherm model for clustered ionomers of Mauritz and Rogers

Mauritz and Rogers [85] conceived a model for equilibrium hydration states of ionomers with clustered morphologies, building upon the previous models of Mauritz, Hora, and Hopfinger [76] and Hsu and Gierke [83]. The Mauritz and Rogers model presumes *a priori* that ion clusters exist, that they are identical in chemistry and size, and that all fixed ions and water molecules are contained in these cluster domains. Unlike its predecessors, this model allows the average number of fixed ions per cluster to vary with water content. Similar to previous models [76, 83], it reasons that when a previously dry strong acid ion-exchange polymer membrane is in equilibrium with water vapor or water, the driving force for membrane swelling will be the diffusion of water into the clusters. This diffusion creates an osmotic pressure derived from a molecular theory of water activity, which is affected by the number of water molecules tightly bound to the ion exchange groups and counterions, the ratio of free and bound water within the cluster, and the counterion dissociation equilibrium (Figure 1.3.2). The osmotic pressure will be increasingly tempered by the pressure created by the retractive forces of the surrounding polymer matrix as it resists deforming as the clusters swell. The local, microscopic Young's modulus of the polymer matrix and the extension ratio of the cluster determine the magnitude of the resisting force of the polymer. Equilibrium is reached when the osmotic pressure within the cluster equals the polymer matrix contraction force. This model predicts three quantities: the average number of sorbed water molecules per ionized sidechain, the cluster radius extension ratio, and the ionic cluster phase's volume fraction when the ionomer is equilibrated in either pure water or water vapor of a specified humidity. Although the Young's modulus used in this model's calculations is on the molecular scale (within 100 Å of the cluster) and varies with water content, calculations

made with macroscopic Young's modulus values yield a reasonable water sorption isotherm expression and water uptake values for Nafion ionomers.

1.3.4.6 Three-phase model

Yeager and Steck [86] proposed a three-phase morphological model for perfluorinated ionomers to explain ion-diffusion coefficients for cations and anions and ion exchange selectivity. This empirical model divided perfluorinated ionomer systems into three different regions: (1) a region containing the amorphous and crystalline fluorocarbon phase, (2) a region at the interface between the fluorocarbon and the hydrated clusters, and (3) the ionic clusters. The bulk of the sorbed water was presumed to be in the ionic clusters in region 3, while the interfacial region (region 2) was believed to consist of fluoroether side chains, a small amount of sorbed water, and ionic groups not incorporated into the clusters. Smaller ions and those with a high charge density reside in the ionic clusters (region 3), while larger ions and those with a lower charge density are expected to be found in region 2. This model is different from the model of Gierke et al. [78, 83, 84] because there is a transition region between the clusters and the polymer matrix, there are no geometric restrictions placed on the clusters, and the geometric distribution of clusters is less ordered (no lattice).

1.3.4.7 Spherical core-shell model of MacKnight et al.

MacKnight et al. [87] proposed a spherical core-shell model comprised of an ion-rich spherical core surrounded by a shell of associated ions. An inter-shell-core region separating the core from the shell possessed an electron density different than either the shell or the core. For an undeformed cesium salt of a 6.1 mol% ethylene-methacrylic acid (E-MAA) copolymer with a core radius of 5 Å, an inner shell radius of 41 Å, an outer shell radius of 46 Å, and a ratio of shell to core electron densities of 0.007, this model fit experimental data with only 7% error [88]. However, the model failed to closely approximate experimental data when the same E-MAA was subjected to deformation, suggesting that a more complex local structure model was required to accurately depict ionomer morphology [88].

1.3.4.8 Modified (depleted-zone) core-shell model of Fujimura et al.

Fujimura et al. [80, 89] proposed a intraparticle core-shell model to explain the morphological origins of two scattering maxima obtained in SAXS and WAXD experiments and data from uniaxial deformation. The maxima, located at $s \approx 0.07$ and 0.3 nm^{-1}, were assigned to morphological features in the crystalline and ionic domains, respectively. For 1100 EW Nafion, changes in the scattering maximum at $s \approx 0.3$ nm^{-1} indicated ionic clusters were observed in the dry state for its cesium sulfonate form [80], cluster dimensions increased with water content and the degree of microscopic swelling was shown to greatly exceed the degree of macroscopic swelling [89]. Nafion also exhibited more uniaxial deformation on the microscopic scale than the macroscopic scale [89]. These results prompted Fujimura et al. [89] to conclude that the best way to represent the morphology of Nafion is by an intraparticle core-shell model in which an ion-rich core is surrounded by an ion-poor shell (i.e. a depleted zone) primarily comprised of fluorocarbon chains. The ionic scattering maximum is proposed to come from the short-range order distance within the core-shell particles which are dispersed throughout a matrix of fluorocarbon chains with ions that exist as nonclustered or in multiplets.

The intraparticle core-shell model model is based on two key assumptions which have led to its eventual disregard as a useful model for Nafion morphology. This model assumes that swelling does not cause ionic groups to redistribute and that the clusters are uniformly distributed in space. These assumptions are not valid because the cluster-network of Gierke et al. [78] allows for cluster reorganization during swelling and Roche et al. [90] observed a small angle upturn in scattering intensity for Nafion which suggested a heterogeneous distribution of clusters.

1.3.4.9 Local-order model of Dreyfus et al.

The spatial distribution of clusters in water-swollen Nafion was the focus of research by Dreyfus and coworkers [91]. They fit a local-order model to scattering intensities obtained from SANS experiments performed on Nafion samples with hydration levels ranging from 6 to 26% by volume. The model assumes spherical, hydrated clusters and defines their local distribution consisting of four nearest neighbors at a well-defined distance arranged in a tetrahedral structure embedded in a matrix of completely disordered (gaslike) clusters. Using a form factor for homogeneous spheres and a radial distribution function for the tetrahedral structure, Dreyfus et

al. derived an expression for the intensity function, I(q), in which the radius of the scattering particle (R), and the distance between locally ordered particles (D) were the only two variables required to obtain reasonable fits over the q-range 0.2 to 2.6 nm^{-1}. The authors concluded based on the close fit between the model and experimental data that both the small angle upturn and the ionomer peak could be attributed to the presence and spatial distribution of ionic clusters. Although this local-order model yielded excellent fits, it yielded an improbably large number of charge sites per cluster calculated from the R values.

1.3.4.10 Lamellar model of Litt

Whereas previous models for Nafion [78, 89, 91] had assumed clusters to be spherical, Litt [92] proposed a reevaluation of this cluster geometry based on morphological and dimensional changes observed by SAXS during swelling and deswelling experiments. Litt noticed that instead of the observed Bragg dimensions of the ionomer peak displaying a 1/3-power dependence on water content as would be expected for isotropic swelling of spherical clusters, the Bragg dimensions scaled nearly linearly with water content. Litt showed that the SAXS data from Gierke et al. [78] indicated a proportional increase in d spacing with water content [92]. Consequently, Litt proposed a lamellar model for Nafion morphology consisting of hydrophilic micelle layers comprised of ionic domains separated by thin, lamellar PTFE-like crystals. This model would allow the hydrophilic micelles to swell with water content, increasing the d spacing between ionic domains linearly with the volume fraction of water in the polymer and permitting reversible behavior.

While this model explains swelling behavior in Nafion well, it is an oversimplification. This model ignores the small-angle maximum observed in SAXS and SANS associated with the important morphological feature of crystalline, interlamellar long spacing. Gebel and Moore [93] observed that the SAXS and SANS peaks of perfluorosulfonate ionomers with short pendant chains did not shift proportionally with an increase in water content; the intercluster spacings shifted in a significantly different way than the interlamellar spacings. These peaks would shift in a parallel manner if the lamellar model were accurate.

1.3.4.11 Sandwich-like model of Haubold et al.

Haubold et al [94] proposed a variation of the lamellar model based on acid form Nafion 117 synchrotron SAXS studies. Samples were dry or equilibrated with methanol, water, or a range of mixtures of water/methanol using an in situ flow cell. A layered model was fitted to the scattering cross section data in which each scattering particle was envisioned as a sandwich consisting of a liquid "core" of water/methanol molecules flanked by a "shell" of side chains, including sulfonic acid groups. Each sandwich had a rectangular parallelepiped structure with lateral dimensions of 1.5 and 4.5 nm and a total thickness of 6.0 nm. These sandwiches were suggested to be oriented in a continuous sequence allowing the liquid core regions to adjoin with each other, thereby forming channels to enable proton transport. According to the model, the core shrinks with increased water content while the shell expands. This model is primarily concerned with local structure as it does not address the organization of main chains (which may form crystallites) or provide a comprehensive three-dimensional configuration of hydrophilic/hydrophobic organization.

1.3.4.12 Gebel model of swelling and dissolution

While the sandwich-like model of Haubold et al. [94] addressed the swelling behavior of Nafion, Gebel [95] went further and developed a model addressing the evolution of perfluorosulfonate ionomer morphology from the dry state through the water swollen state to solution. Their goal was to model morphological changes associated with the dissolving and solution casting processes in Nafion. Small-angle scattering measurements were performed on swollen membranes whose water volume fraction ranged from 0.3 to 0.93 and homogeneous aqueous solutions with polymer volume fractions up to 0.12. Based on the results of these experiments coupled with energetic considerations, Gebel proposed a qualitative model for swelling and dissolution of Nafion (Figure 1.13). The ionomer in the dry state begins as isolated, spherical ionic clusters in a perfluorinated polymer matrix. The clusters have diameters of ~1.5 nm and their centers are ~2.7 nm apart). With an increase in water content, interfacial energy is kept at a minimum as these clusters swell to hold the droplets of water surrounded by the ionic groups. Percolation begins to occur between water volume fractions of 0.3 and 0.5, as the ionic domains reorganize and connecting cylinders of water form between the swollen spheres to maintain constant surface area. A structural inversion begins to occur as water volume fraction

increases above 0.5 and the polymer matrix evolves into a network of connected rods. These rods appear to disconnect and separate into a colloidal dispersion of rods as the membrane eventually "dissolves" into solution. While this model provides a reasonable transition from ion clusters in relatively dry membranes to rod-like structures in solution, there is no thermodynamic justification or experimental scattering data to support the proposed phase inversion around a water volume fraction of 0.5.

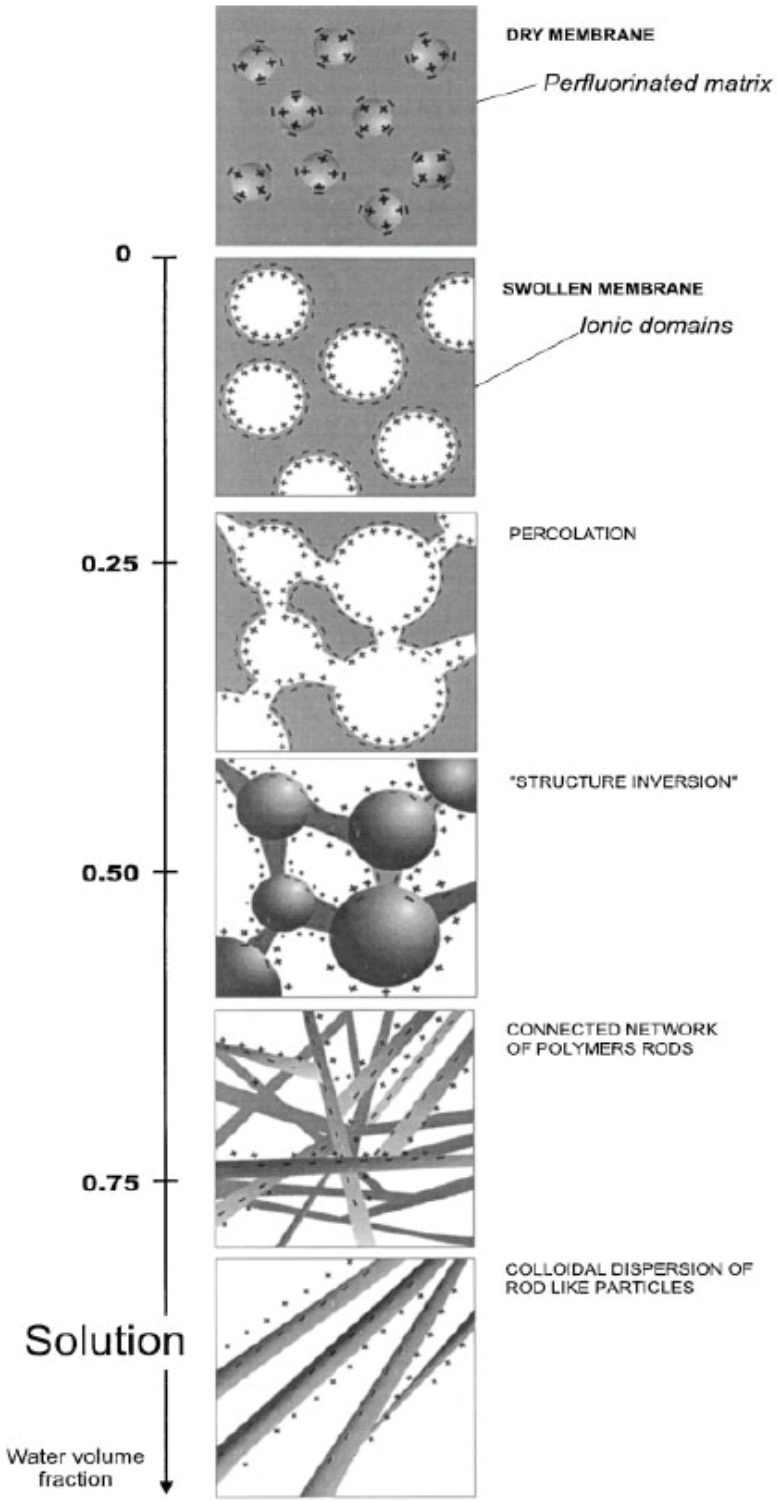

Figure 1.13. Conceptual model of Gebel for swelling and dissolution of Nafion with increasing water content. Reprinted from [84, 95] with permission from Elsevier.

1.3.4.13 Rod-like model of Rubatat

Rubatat and coworkers [96] provided additional experimental scattering data to complement and refine Gebel's model [95] of morphological evolution with water content. Using a combination of USAXS, SAXS, and SANS, the authors probed the morphology of hydrated Nafion from 1 to 1000 nm. The scattering curves assembled from these experiments contained the extended small-angle upturn from long-range electron density heterogeneities below 10^{-3} $Å^{-1}$, the low angle maximum (matrix knee) due to supralamellar distances within the crystalline domains, and the ionomer peak associated with local ordering between ionic clusters. The data at low angles followed a q^{-1} power law and yielded domain dimensions indicating a rod length and diameter of ≥1000 Å nm and ~60 Å, respectively. The authors reasoned that rod-like aggregates in the system could more accurately be considered as ribbon-like, with cross-sectional thickness and width around 20 and 80 Å, respectively. Therefore at low water contents, the ribbons pack face to face and at higher water contents where the aggregates are spaced more than 80 Å apart, the aggregates become like cylinders as the distribution around their long axis becomes isotropic. This model reconciles the rod-like morphology with observed differences in swelling behavior observed above and below a water volume fraction of 0.6, while remaining consistent with previous observations [97] that swelling does not involve a strong structural reorganization of cluster morphology as suggested by Gebel [95], but a dilution of entities which induce scattering. Rubatat et al. [96] propose that information about these ribbon-like aggregates (size, shape, and distribution) is found in the small angle scattering region (intermediate *q*-range), while the extended small-angle upturn region (very small *q*-range) contains information about large bundles of these aggregates, whose long-range distribution is heterogeneous. Information about the small concentration of crystalline regions of Nafion lies between these two regions in *q* space. There has been very little information obtained from this region as a result of Nafion's low degree of crystallinity (~8-12 wt% [80]). More research is required to determine the location of these crystalline domains within perfluorosulfonated ionomers and better understand their effect on the ionomer's physical properties.

1.3.5 Effect of morphology on PEM characteristics

The morphology of a polymer membrane has a dramatic influence on its usefulness as a PEM [35]. Specifically, it is the ability of a polymer to phase separate into both hydrophilic and

hydrophobic domains and the degree to which this occurs that determines many PEM characteristics including ion conductivity, gas permeation, water transport (diffusion, electro-osmotic drag), water uptake, interfacial adhesion and mechanical strength. There are three different scale lengths at which polymer microstructure influences membrane properties. On the smallest scale, the dissociation distance between the counter ion of the polymer and the charge-carrying ion must be considered. At the next level, aggregation of ions and the effect of side chains become relevant. The separation of dissimilar components of the polymer occurs at the highest level, from the nano- to microscale.

The degree to which morphology affects PEM proton conductivity appears to be a function of the ion content of the membrane [35]. At low IEC values, morphologies that create enhanced ionic domain conductivity (e.g. ion channels) through phase separation yield significantly higher proton conductivities and appear to use absorbed water more efficiently. This phenomenon has been observed in several polymer systems. Sulfonated polysulfone-*b*-poly(vinylidenefluoride) multiblocks displayed proton conductivities up to four times higher than their related sulfonated polysulfone homopolymers when both were at low IEC values (0.78-1.30 mmol/g vs. 0.83-1.25 mmol/g) and similar values of water uptake (14-25 % vs 15-25 %) and λ (number of water molecules per acid group; 9.9-10.6 vs. 10.0-11.1) [98]. Conductivities increased with IEC, but the difference between block and homopolymer conductivities decreased. Ultimately, the conductivities of the two were identical at IEC values above 1.4 mmol/g. Sequenced sulfonated naphthalenic polyamide multiblocks were shown to have higher proton conductivities than randomly sulfonated naphthalenic polyimides, but this difference decreased with an increase in IEC [99, 100]. Interestingly, the conductivity of a naphthalenic sulfonated polyimide block copolymer synthesized by Cornet et al. [101] was shown to vary nonlinearly as ionic block length increased from 1 to 9 repeat units, reaching a maximum of 0.018 S/cm at 3 units and decreasing thereafter [101]. Sulfonated crosslinked poly(styrene-*b*-butadiene-*b*-styrene) (SBS) triblocks displayed proton conductivities higher than their corresponding statististical copolymers by three orders of magnitude at a given degree of sulfonation, attributed to the formation of ionic channels in the triblock copolymers [102]. Analysis of the SBS copolymers by small angle x-ray scattering (SAXS) and transmission electron microscopy (TEM) confirmed the presence of a cylindrical morphology in samples up to 23.5 mol% sulfonation, but this morphology was not present at higher sulfonation levels.

Polystyrene-*g*-polystyrenesulfonic acid (PS-*g*-PSSA) graft block copolymers have also displayed IEC-dependent conductivities [103, 104]. A PS-*g*-PSSA graft copolymer with 16.1 mol% sulfonic acid content possessed proton conductivity an order of magnitude larger than that of a PS-*r*-PSSA random copolymer of similar sulfuric acid content (16.8 mol%) even though the water content of the graft copolymer was 60% lower [104]. The effect of phase separation upon proton conductivity it not as pronounced in membranes with high IEC values as it is with those with low IEC values [35]. A possible reason for this observation may be that the high ion and water contents of high IEC membranes enables them to achieve a percolation limit for ionic regions independently of microphase separation. While the effects of the number of ionic regions on the properties of a PEM have been well-characterized, the role that ionic domain size plays in proton conductivity and other PEM properties is still not fully understood.

Morphology may or may not have an effect on the swelling of a PEM. Morphology does not appear to play a role in swelling of membranes of poly(styrene-*b*-butadiene-*b*-styrene) (SBS) block copolymers compared to poly(styrene-*r*-butadiene) (SBR) statistical copolymers. Even when each was crosslinked by ultraviolet (UV) radiation to preserve its microstructure, the degree of swelling of each membrane was dependent only on its IEC value and not its morphology [102].

The morphology of a PEM influences its methanol permeability. Since methanol and water have similar properties (e.g. dipole moment), they both diffuse through the hydrophilic ionic domains of a PEM. However, since methanol molecules are larger than protons, methanol permeability can be reduced without sacrificing proton conductivity by restricting the cross-sectional area of ionic channels through a PEM. Won et al. [102] successfully fixed the structure of poly(styrene-*b*-butadiene-*b*-styrene) by UV-crosslinking the triblock copolymer in the presence of a photoinitiator before sulfonating it. The resulting polymer membrane yielded a methanol permeability of 8.1×10^{-8} cm^2/s, and more than thirty times lower than Nafion®.

1.3.6 Viscoelastic properties of ionomers

A considerable amount of study has been performed on the viscoelastic properties of ionomers [105-127]. The following discussion is restricted to the linear viscoelastic domain in which the Boltzmann superposition principle is obeyed (i.e. when an applied stress is increased or decreased within a given time scale, the observed strain will change by the same percentage as

the applied stress). Ionomers may either possess some crystallinity or be completely amorphous. Perfluorosulfonate ionomers (e.g. Nafion) are not entirely amorphous because their Teflon-like backbones may form crystallites. Amorphous ionomers (e.g. sulfonated polystyrene, sulfonated polyarylene ethers) possess no discernable crystallinity and their properties fall into three categories: the glassy state, the glass transition region, and the rubbery region. Only the first two categories will be discussed here since ionomers used in PEM applications are mainly used in the glassy state below their glass transition temperatures.

1.3.6.1 The glassy state

In the glassy state at temperatures well below the glass transition temperature (T_g) of an ionomer, its ionic groups generally have a negligible effect on its viscoelastic behavior [128]. The reason is because motion within a polymer in the glassy state is localized to chain segments and it occurs over long time scales. Ionic groups along the length of a molecule, however, typically influence viscoelastic and mechanical properties by restricting long-range molecular motion over short time scales (typical of temperatures above T_g).

Despite this, several researchers using dynamic mechanical analysis (DMA) have observed sub-T_g relaxations affected by ionic associations which restrict localized main-chain motions in both amorphous and semicrystalline ionomers [105-108]. Drzewinki and MacKnight [105] observed a β relaxation associated with the addition of ionic sulfonated groups to amorphous polysulfone. This relaxation is a function of counterion, water content, and thermal history. It increases in magnitude with increased ion association and decreases in temperature with increased hydration and decreased ion association. Since water facilitates the relaxation, the β relaxation in sulfonated polysulfone is attributed to hindered rotations of the pendant sulfonate groups rather than ionic interations. Drzewinki and MacKnight also concluded that the sulfonated groups do not cluster, but instead form multiplets of ion pairs and quartets. Characterizing sub-T_g relaxations in perfluorosulfonated ionomers has not been as straightforward. Yeo and Eisenberg [106] studied the effect of water and counterion on the dynamic mechanical properties of Nafion over a temperature range of -190 to ~150 °C identified α, β, and γ relaxations (α > β > γ) for the acid form of Nafion, with the β relaxation magnitude and temperature responding similarly to counterion, water, and temperature as the one reported for sulfonated polysulfone [105]. The α relaxation was attributed to the glass transition

temperature of the matrix, the β transition to the ionic domains, and the γ relaxation to the short range motion of the $–CF_2–$ backbone. Eisenberg and coworkers [124] reversed the assignment of the α and β relaxations as the result of a later study. More recently, Moore and coworkers [127] have compared DMA, variable temperature SAXS, and variable temperature solid-state ^{19}F NMR data for Nafion and decisively concluded that the β relaxation actually corresponds to the true glass transition temperature (T_g) of Nafion.

In addition to its dynamic mechanical properties, fracture and fatigue behavior is another important mechanical property of an ionomer in the glassy state. Extensive fracture and fatigue experiments have been conducted by Hara, Sauer, and coworkers to determine the effect of ionic associations on glassy polymers [109-112]. Hara et al. [110] showed that ionic associations do affect fatigue behavior of polystyrene, measured in the number of cycles to damage initiation, N_i, and the number of cycles to fracture, N_f, as a function of ion content measured by neutralization of sulfonic acid groups with sodium. Both N_i and N_f decrease with an increase in ion content up to 5 mol%. Between 5 and 6 mol% ion content there is a jump in N_i and N_f, which remain higher above 6 mol% than the for original polystyrene, demonstrating ion-induced fatigue resistance above 6 mol%. This transition at 5-6 mol% ion content, corresponds to the point where the multiplet-to-cluster transition has been observed for sulfonated polystyrene [109] and the boundary above which time-temperature superposition no longer holds [113]. These data suggest that below 5 mol% the ions exist predominantly in multiplets which act as physical crosslinks to decrease fatigue resistance, but that above 6 mol% the ions transition into filler particle-like clusters which reinforce the polymer. Hara et al. also determined that fatigue resistance of ionomers in the glassy state is affected by neutralizing ion type (divalent calcium salts reinforce polystyrene three times better than monovalent cesium and potassium salts) [112] and excess neutralizing agent (a 100% excess of NaOH improved resistance while a 300% excess decreased it) [111]. These fracture and fatigue behavior data, along with the dynamic mechanical behavior data for ionomers in the glassy state, are dwarfed by the data obtained to investigate the glass transitions of ionomers.

1.3.6.2 The glass transition region

The viscoelastic and mechanical properties of ionomers in their glass transition region can be greatly affected by ionic groups and much work has been performed on ionomers in this

region [113-119]. Much of the focus of this work has been placed on identifying the thermal transitions (e.g. glass transition temperature) and dynamic mechanical relaxations of perfluorosulfonate ionomers (e.g. Nafion), especially considering the potential temperature limitations that may be encountered during operating fuel cells at elevated temperatures. Moore and Martin [121], working with a series of Dow perfluorosulfonate ionomer membranes whose side chains are shorter than those of Nafion, observed two or three endotherms in DSC thermograms for the ionomers. They assigned the lower endotherm (150-180 °C) to the matrix glass transition ($T_{g,m}$), which decreased with an increase of side chain length. The middle endotherm (270-300 °C) was assigned to the cluster glass transition ($T_{g,c}$). Similar endotherms (ca. 150 and 260 °C) were observed by Moore and Martin [122] for Na^+-form Nafion and similar thermal relaxations (ca. 140 and 240 °C) were previously observed by Kyu et al. [124] by DMA for Na^+-form Nafion and assigned as the $T_{g,m}$ and $T_{g,c}$, respectively. The highest endotherm (ca. 335 °C) observed by Moore and Martin for the Dow ionomers was observed for those with high equivalent weight and assigned to the melting of Teflon-like crystallites (T_m) [121]. This paradigm of a dual Tg explanation for two DMA relaxations where the T_g of the matrix is reflected in the α relaxation and the T_g of regions of restricted mobility (e.g. ionic clusters) is reflected in the β relaxation was widely accepted for many years. Only recently, Moore and coworkers [127] have demonstrated that although this model is acceptable for polystyrene- and polyethylene-based ionomers, it does not describe the behavior of Nafion accurately. By comparing DMA, variable temperature SAXS, and variable temperature solid-state ^{19}F NMR data for Nafion, Moore and coworkers [127] arrived at more conclusive assignments for the endotherms and dynamic mechanical transitions observed for Nafion. The low temperature endotherm was attributed not to the $T_{g,m}$ as previously thought, but to the melting of small imperfect crystals, similar to that observed in other crystallizable copolymers. The middle endotherm, corresponding to the β relaxation and previously considered the $T_{g,c}$, was determined to be the genuine glass transition of Nafion. It is the T_g of the entire ionomer—the onset of thermally activated segmental main-chain motions enabled by side chain mobility within a *static* physical (electrostatic) network. The highest temperature endotherm (α transition), previously associated with crystallite melting, was assigned to the onset of long-range main and side chain mobility enabled by destabilization of the electrostatic network of the ionomer. Around these temperatures, activation of a *dynamic* network happens as electrostatic interactions within

aggregates weaken and "ion-hopping" occurs as ionic pairs "hop" from one aggregate to another to relieve local stress. It is important to remember that this thermal and dynamic mechanical behavior of Nafion does not apply to non-perfluorosulfonated ionomers. For example, Drzewinki and MacKnight [105] associated the α relaxation observed for sulfonated polysulfone ionomers in DMA with the matrix glass transition because it was the only transition measurable by DSC. Consequently, the remainder of this section will discuss the glass transition of ionomers in terms of $T_{g,m}$ and $T_{g,c}$.

The amorphous regions of an ionomer are thought to give rise to its matrix glass transition ($T_{g,m}$). This transition is thought to be the threshold temperature above which the polymer chain segments can translate and rotate [129]. Since the glass transition is a function of cooperative backbone motion, it can be significantly increased by ionic associations that restrict such motion. The magnitude of this increase is determined by several factors: the location of the ionic sites within the molecule, the concentration of ionic groups in the molecule (i.e. equivalent weight), the type and size of the counterions, and the degree of hydration of ionic groups. The location of the ionic sites within the molecule may vary widely (random vs. telechelic, within the backbone, in a pendant group, at the end of a long chain, multiplets, clusters, etc.). The more randomly distributed the ionic groups, the more restrictions are placed on chain mobility. Gauthier et al. [126] report that ionic groups in polymers raise the $T_{g,m}$ more efficiently when they exist as multiplets instead of clusters because they are more available to act as ionic crosslinks. Eisenberg and coworkers [115, 117] reported that the amount of restricted mobility can be quantified by the product of q/a and c, where q is the neutralizing ion charge, a is the distance between charges, and c is the concentration of the ionic species. Intermolecular forces from ionic groups can raise the $T_{g,m}$ considerably with only a small increase in the concentration of ionic groups (2 to 10 °C/mol% ions) and the effect will scale with the magnitude of the ionic forces [123]. For example, the incorporation of ions into Nafion substantially increases its $T_{g,m}$ from 10 °C for its nonionic sulfonyl fluoride precursor form [107] to 150 °C for its sodium form [124, 125]. Similarly, Moore and Martin [121] observed an increase in the $T_{g,m}$ of Dow perfluorosulfonate ionomers with a decrease in equivalent weight, a phenomenon observed in many ionomers and attributed to the formation of ionic crosslinks [106]. Risen and coworkers examined the influence of the cation type used for neutralization and sulfonation level on the T_g of sulfonated polystyrene [118, 119]. Contrary to behavior exhibited by other ionomers, the T_g

was affected neither by the type nor size of the neutralizing cation, but only sulfonation level [119]. Drzewinki and MacKnight [105] and Noshay and Robeson [20] found that sulfonation of polysulfone polymers increased the T_gs [20, 105], as well as the moduli [105] of the ionomers. Finally, the hydration level of ionic groups also has a considerable effect on their influence on the glass transition. Stress relaxation tests of submerged Nafion have shown its $T_{g,m}$ to decrease considerably in water, likely because the hydration of the ionic domains results in a plasticizing effect which enhances segmental mobility of the polymer backbone [125]. Drzewinki and MacKnight [105] observed that the effect of hydration upon the α relaxation of sulfonated polysulfone ionomers varied with counterion. While DSC data showed that water lowered the glass transition for sodium and cesium ionomers, DMA data showed that the α-relaxation temperature lowered in the presence of water for the sodium ionomers, but sometimes increased for the cesium ionomers. The authors reasoned that these results may be a function of both the ability of cesium to form contact ion pairs as well as the amount of water present in the two salts at T_g. This was confirmed by a brief increase followed by a decrease observed in the α-relaxation temperature as the cesium salt was gradually exposed to water. This suggested that small amounts of water disrupt ionic aggregates, which forms free ions and increases the α-relaxation temperature until additional water hydrates the free ions and lowers the T_g.

In addition to ionic associations, the T_g of an ionomer can also be influenced by its nonionic characteristics such as backbone flexibility, intermolecular forces, and pendant group size. Jérôme et al. [120] proposed that an ionomer's observed glass transition temperature was a function not only of the strength of ionic associations at the test temperature, but also a function of observation time (e.g. scan rate) and of the relative flexibility of the polymer backbone. Consequently, strongly associated ionic groups may profoundly increase the T_g of a low T_g material with a flexible backbone by restricting its mobility, but the same ionic groups may have a very small influence on the T_g of a high T_g material with a stiff backbone. Hydrogen bonding and other intermolecular forces limit polymer chain mobility, thus influencing $T_{g,m}$ [130]. Also, the $T_{g,m}$ will increase with increasing size of rigid pendant groups, but it will decrease with the plasticizing effect of an increase in size of flexible pendant groups [131].

The cluster glass transition, $T_{g,c}$, is the temperature corresponding to the onset of mobility within the ionic clusters of an ionomer. Mobility is typically restricted within clusters due to ionic associations. Both the strength of electrostatic aggregates and the nature of the polymer

chains affect the balance of electrostatic and elastic forces that stabilize ionic clusters, so they both influence $T_{g,c}$, the temperature at which the clusters can thermally relax. Multiple DMA studies have been performed to characterize the $T_{g,c}$ transition in Nafion [124-126]. Nafion's ionic cluster glass transition, $T_{g,c}$, appears as a peak around 240 °C when Nafion is hydrolyzed from its sulphonyl fluoride precursor form to its sodium form. This transition is strongly affected by neutralization, cation type, and hydration and shown to increase with degree of neutralization, counterion size, and strength of intracluster ionic interactions. Water, known for its plasticization effect, causes a dramatic decrease in the $T_{g,c}$. Moore and coworkers [127] showed that this transition corresponds to a disruption in Nafion's electrostatic structure as it transitions from a static electrostatic network to a dynamic electrostatic network.

1.4 Characterization Methods

Multiple characterization techniques exist to characterize the morphologies and the structure-property relationships of ionic polymers. This review will focus on four of them: atomic force microscopy, transmission electron microscopy, uniaxial (tensile) testing, and scanning electron microscopy.

1.4.1 Atomic force microscopy (AFM)

Atomic force microscopy (AFM) is a form of scanning probe microscopy (SPM) in which a probe tip is scanned over a surface to obtain a topographical image of the surface. The objective in AFM is to scan the tip over a sample surface at a constant height above the surface or at a constant force by using feedback mechanisms [132]. This process begins as the tip of a micro-machined cantilever mounted on a piezoelectric actuator is scanned over the surface of a sample (Figure 1.14). A laser beam within the system is reflected off of the back of the cantilever tip and detected by a position-sensitive photodiode. As the tip moves up and down during scanning, the laser beam is deflected between the upper and lower sections of the photodiode. The light intensity differences between the upper and lower photodetectors of the photodiode are transmitted through a computer-controlled feedback loop to a second piezoelectric actuator connected to either the cantilever or the sample. This feedback allows the piezoelectric actuator to continuously adjust during scanning to maintain the cantilever tip either at a constant height above the sample surface or at a constant force.

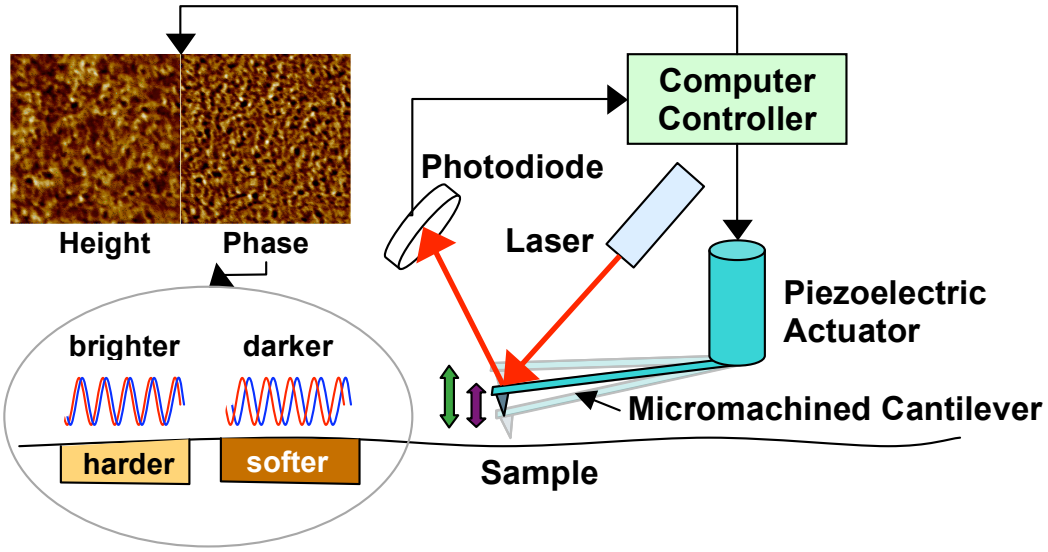

Figure 1.14. Schematic diagram of Atomic Force Microscope (AFM)

An AFM system images the topography of a system by measuring the attractive and repulsive forces between the probe tip and the sample surface [132]. These forces change as the distance between the tip and the surface changes (Figure 1.15). As the probe tip approaches the surface from a distance, it begins to detect the long-range attractive van der Waals forces between the nuclei of its own atoms and the atomic nuclei in the sample. These attractive forces increase as the tip continues moving towards the surface. At the same time, the electron clouds of the tip atoms and the sample atoms gradually approach each other and a resulting repulsive force begins to grow. This repulsive force begins to slowly cancel out the attractive forces as the tip moves even closer to the sample until the electron clouds come in contact with each other and completely cancel any attractive forces. The repulsive forces continue to grow and dominate from this point until the tip contacts the sample. Consequently, the AFM can be operated in three major modes (Figure 1.16) which correspond to the three main regions of the force-distance curve: non-contact mode (dominated by attractive forces), contact mode (dominated by repulsive forces), and tapping mode (consisting of intermittent contact through both attractive and repulsive force regions). Other scanning modes that may be performed with an AFM include friction force microscopy, chemical force microscopy, electrostatic force microscopy, and magnetic force microscopy [133], but these modes are outside of the scope of this review and will not be discussed in further detail.

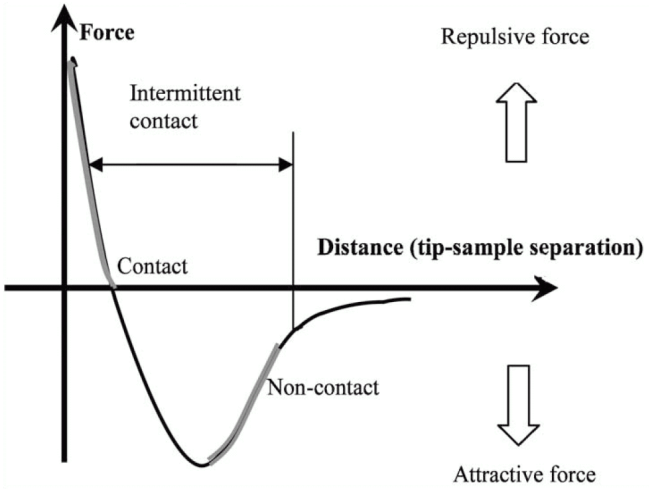

Figure 1.15. Interatomic force variation versus distance between AFM tip and sample. Reprinted from [84, 95] with permission from Elsevier.

In contact mode (Figure 1.16, left), the probe tip contacts the surface to be imaged [132]. This mode yields a very high resolution because the area of the surface contacted by the tip is very small. In this mode, the tip is sensing only the repulsive forces (< 10 nN) between it and the surface. Contact mode may be performed in two different ways: constant height mode and constant force mode. In constant height mode, the z-axis of the probe is fixed during scanning and surface forces are measured. (Figure 1.17a) The disadvantage of this mode is that steep features may damage the probe tip because it may collide with them as it moves at a constant height. In constant force mode, the force between the tip and the sample is kept constant by feedback and the distance between the probe and the surface varies. (Figure 1.17b) The disadvantage to this mode is that shear forces from the tip can damage soft samples.

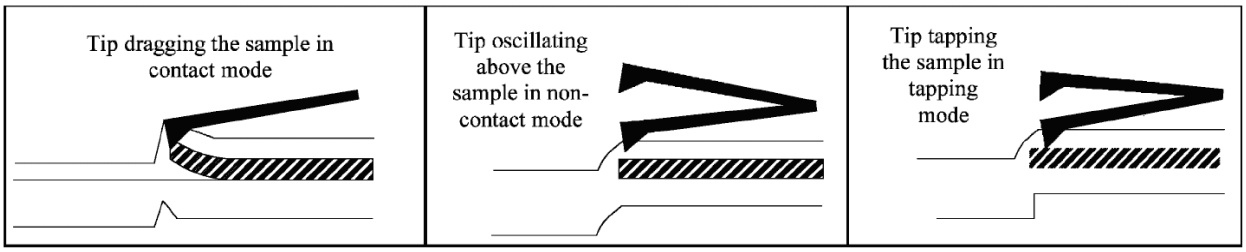

Figure 1.16. Three major modes of AFM operation: contact (left), non-contact (middle), and tapping (right). Reprinted from [84, 95] with permission from Elsevier.

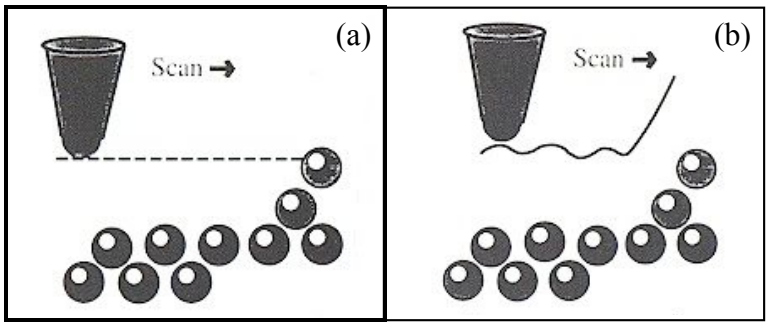

Figure 1.17. Two contact modes (a) constant height and (b) constant force. Reprinted from [77] with kind permission of Springer Science and Business Media.

In non-contact mode (Figure 1.16, middle), the AFM probe tip oscillates at 50-150Å above the sample surface without contacting the sample [132]. In this range, the tip is sensing only the long range attractive van der Waals forces between it and the surface. Unfortunately, when samples are imaged in this mode in ambient conditions, contaminants in the air (especially moisture) adsorb to the sample surface forming a fluid contaminant layer. This fluid contaminant layer may degrade the resolution images obtained in non-contact mode because it can obscure the attractive forces sensed by the tip.

Tapping mode (Figure 1.16, right) combines the positive attributes of both contact and non-contact modes [132]. In tapping mode, a piezoelectric actuator oscillates the cantilever at a resonance frequency and the cantilever is slowly lowered until it taps the sample surface. The amplitude of the cantilever's oscillation will change with the topography of the surface, allowing the topography to be easily mapped. The tapping motion of the tip prevents tip damage characteristic of contact mode because the tip does not collide with elevated surface features as in constant height mode and sample damage caused by shear forces from the tip are also prevented. Soft samples can be imaged with high resolution in tapping mode, especially because the oscillation of the tip moves it in and out of any fluid contaminant layer present, minimizing the influence of the layer on the resolution.

The initial amplitude at which the cantilever is oscillated in tapping mode is called its free air amplitude. When the amplitude of the cantilever's oscillation begins to decrease as the cantilever is lowered to the sample surface, feedback mechanisms in the AFM computer controller are used to keep the cantilever's oscillation at the surface at a specified setpoint. The ratio of this setpoint amplitude and the cantilever's free air amplitude is known as the amplitude ratio. This ratio, usually between 0.5 and 1.0, may vary by sample and is a measure of how hard

the tip is tapping on the surface. If the amplitude ratio is too high, the tip may not tap hard enough to image features on the sample surface. If it is too low, the tip may flatten surface features as it is tapping. The lower the amplitude ratio, the deeper below the surface the tip can probe.

Two image types that can simultaneously be obtained via tapping mode and are commonly reported in the literature are height image and phase image (Figure 1.14). The amplitude of the oscillating cantilever decreases as topographical features increase in height and it increases as topographical feature height decreases. The brightness of an imaged feature increases with its height. For phase imaging, the AFM system detects the phase lag between the initial oscillation imparted to the cantilever by its piezoelectric actuator and the one sensed by the photodiode during imaging (Figure 1.14). The difference in phase between the two oscillations will be very small for hard, hydrophobic features as the tip rebounds quickly after tapping the surface. It will become larger as features become softer, more hydrophilic, or more adhesive because the tip will sink into or briefly adhere to the surface upon tapping, delaying the oscillation. The computer controller inverts these phase lag signals, resulting in features with smaller phase lag appearing brighter and features with larger phase lags appearing darker.

The type of tip used for AFM imaging is a very important consideration [77]. The resolution of an AFM image is based on the size, shape, and stiffness of the tip (Figure 1.18). Slender, needlelike tips will image the edges of features much more accurately than large, wide tips will (Figure 1.18a). Carbon nanotubes work very well for obtaining high resolution (on the atomic scale) but they frequently break because they cannot withstand the shear forces often encountered during imaging. Artifacts in AFM images can often be caused by the imaging tip. For example, if the tip is too broad so that the tip is larger than the feature to be imaged, the microscope will ultimately image the tip itself instead of the feature. If the tip becomes chipped during imaging (Figure 1.18b), features may be imaged twice, resulting in pairs of features in the image. Additionally, streaks may appear in an AFM image if debris becomes stuck to the tip during imaging (Figure 1.18c).

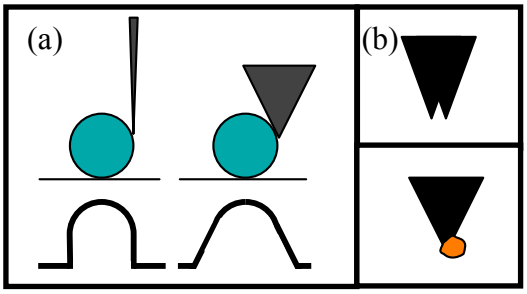

Figure 1.18. Tip resolution and artifact issues (a) tip size vs feature size, (b) chipped tip, (c) contaminated tip; (a) adapted from [77] with kind permission of Springer Science and Business Media.

AFM is advantageous for several reasons [77]. With AFM it is possible to obtain high resolution images (down to atomic resolution) of non-conductive samples. AFM can image samples in ambient, fluid, or high vacuum environments. AFM is also less expensive than scanning electron microscopy (SEM). The few disadvantages to AFM include that the tip may be easily damaged or contaminated during use, causing artifacts. Also, samples may not be scanned at extreme high and low temperatures because this may ruin the tip alignment.

1.4.2 Transmission electron microscopy (TEM)

While AFM images the surface of a sample with a micromachined probe, transmission electron microscopy (TEM) images the bulk of a sample by using an electron beam. TEM is an optical microscopy technique, meaning that radiation passes through the sample to create an image [77]. An electron beam with a short wavelength serves as the radiation source emitted from the top of the microscope column and aimed at the specimen mounted within the column (Figure 1.19). Magnetic lenses focus the beam before and after it passes through the specimen before it ultimately forms an image on a screen or film at the base of the column.

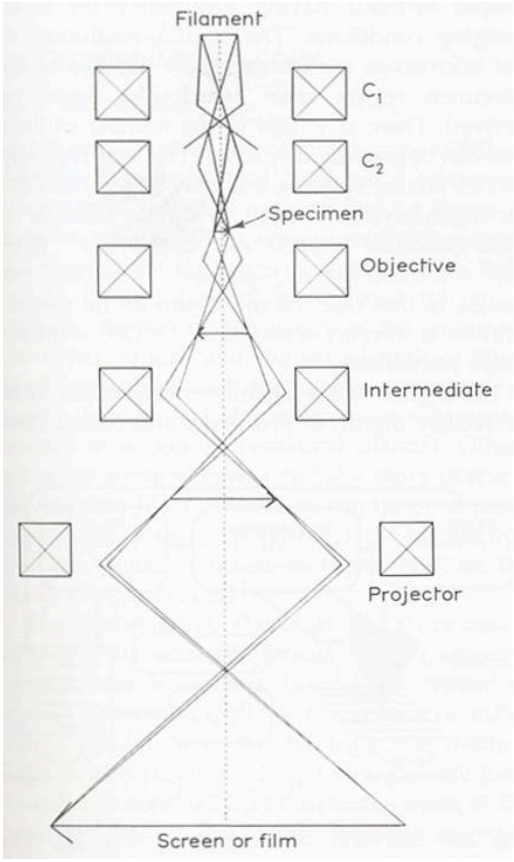

Figure 1.19. Schematic drawing of a transmission electron microscope (TEM). Reprinted from [77] with kind permission of Springer Science and Business Media.

The contrast of a TEM image is a function of electron scattering by the sample [77]. In bright field imaging mode, where the electron beam is allowed to directly reach the image plane unscattered, the brightness of a region increases with electron scattering, but electrons that are scattered to large angles are ignored. Image brightness depends on local mass thickness (thickness × density) in amorphous materials (*mass thickness contrast*) and crystal orientation in semi-crystalline materials (*diffraction contrast*). Maximum contrast is achieved by keeping objective aperture diameter small and accelerating voltage low. In dark field imaging mode, an image is formed only by radiation scattered by the specimen. Compared to bright field images, dark field images have higher contrast and lower intensity (brightness). Dark field TEM can be used to measure crystallite dimensions and orientation in semi-crystalline polymers, but amorphous polymer samples are seldom imaged in this mode. This is because the intensities of these samples are very low as only some of the electrons scattered in every direction can be

collected by the objective aperture. The necessity of long exposure times coupled with image instability make dark field imaging of polymers quite challenging [77].

Preparation of samples for TEM usually requires much time and skill. Specimens must be extremely thin (30-100nm). These small thicknesses can be achieved by different methods depending on the form of the polymer to be imaged (e.g. particles and solutions vs. thick/bulk polymers) [77]. Polymer samples in particulate or solution form may be prepared for TEM by one of three methods: dispersion, disintegration, and thin film casting. Specimens may be created by dispersion from solutions or suspensions of polymers by spraying or wetting TEM specimen grids with the solution and allowing the excess solvent to evaporate. This can be done for high molecular weight polymers in dilute solution. Disintegration is used to creating samples from fibers by breaking them apart into fine fibrillar structures in a cool ultrasonic bath (typically water, ethanol, or water/ethanol) often for 30 minutes or more. Thin film casting, as its name implies, involves casting thin films of a sample on glass, freshly cleaved or fractured inorganic surfaces (e.g. mica or NaCl), or liquid (e.g. mercury, glycerol, orthophosphoric acid). Films are lifted off and picked up on TEM grids. Specimens of thick or bulk polymers must be prepared by a different way called ultramicrotomy, a process that yields thin sections of the sample. Large specimens may be cut with saws and razor blades to fit directly into the chuck of an ultramicrotome, but smaller or softer samples (e.g. fibers, films) must be embedded in a resin for orientation and support. A range of resins (e.g. epoxy resin, polyester resin, methacrylates) can be used for embedding specimens in a sample mold. For most dry polymer samples, room temperature curing epoxies are sufficient. A range of mold shapes exist to accommodate a variety of sample shapes and orientations. Once the sample is embedded in a resin, it is removed from the mold and placed in a vise and either cut with a jeweler's saw, or with a razor blade under a stereo microscope to allow for fine trimming. The goal is to produce a flat top with sloping sides to form trapezoid, trimming a maximum of epoxy away in the process. This trimmed block is then secured in the ultramicrotome chuck and sectioned into very thin slices with a glass or diamond knife. The sections float across a water surface directly behind the knife and are subsequently lifted onto TEM grids. If the polymer sample has a glass transition temperature near or below room temperature, regular ultramicrotoming will not section it successfully and it will have to be cyromicrotomed at cryogenic temperatures. In general,

ultramicrotoming is very time-consuming and tedious and requires a lot of practice to adequately prepare samples.

Contrast of polymer samples for TEM can be enhanced by staining [77]. Typically TEM images of polymer samples have very poor contrast because the polymers are comprised of atoms with low atomic numbers, like hydrogen and carbon, which do not scatter electrons well. Staining polymer samples involves incorporating electron dense atoms into them. This can be done physically, by adsorbing the atoms into the microstructure of the polymer, or chemically by reacting the electron dense species with the polymer. The latter way is preferable because atoms that are not chemically bonded to the specimen risk being extracted in the vacuum of the TEM chamber. Staining allows both dispersed phases in multiphase polymers (e.g. high impact polystyrene stained with osmium tetroxide) and detailed fine structures of polymers (e.g. lamellar structure of polyethylene stained with chlorosulfonic acid) to be observed via TEM. Ionomer membranes have been stained by introducing electron dense counterions into the membranes to convert them to the lead (Pb^{2+}) [134], cesium (Cs^{+})[89], silver (Ag^{+}) [98], or tin and silver (Sn^{2+} and Ag^{+}) [78] ion form. A variety of stains exist for use with polymer specimens, but there is no single reference that catalogues every stain matched with its reactive polymer group. A partial listing is given in Table 1.3. Most stains used with polymers are positive stains, meaning that the region of the polymer with which they react appears darker in the micrograph. In contrast, negative stains darken the area around the features of interest, often used to image latex or emulsion materials. Specimens can be stained either before or after sectioning by either immersion in the stain solution or exposure to vapor. Samples stained prior to sectioning may be cut into small blocks (~1-3 mm across) or embedded and trimmed before staining. Trimming before staining is especially helpful when the stain diffuses into the specimen slowly because the stain will be most concentrated in the outer surface of the specimen to be sectioned. In addition to immersion and vapor exposure, sectioned specimens may be stained by placing them on a droplet of stain solution.

Table 1.3. TEM stains for specific functional groups and polymer examples [77].

Functional group	*Examples*	*Stains*
−CH−CH−	Saturated hydrocarbons (PE, PP) (HDPE)	Chlorosulfonic acid Phosphotungstic acid Ruthenium tetroxide
−C=C−	Unsaturated hydrocarbons (polybutadiene, rubber)	Osmium tetroxide Ebonite Ruthenium tetroxide
−OH, −COH	Alcohols, aldehydes (polyvinyl alcohol)	Osmium tetroxide Ruthenium tetroxide Silver sulfide
−O−	Ethers	Osmium tetroxide Ruthenium tetroxide
−NH2−	Amines	Osmium tetroxide Ruthenium tetroxide
−COOH	Acids	Hydrazine, then Osmium tetroxide
−COOR	Esters (butyl acrylate) (polyesters) (ethylene-vinyl acetate)	Hydrazine, then Osmium tetroxide Phosphotungstic acid Silver sulfide Methanolic NaOH
−CONH2 −CONH−	Amides (nylon)	Phosphotungstic acid Tin chloride
Aromatics	Aromatics Aromatic polyamides Polyphenylene oxide	Ruthenium tetroxide Silver sulfide Mercury trifluoroacetate
Bisphenol A based epoxies	Epoxy resin	Ruthenium tetroxide

Like any technique, TEM has its advantages and disadvantages. This powerful bulk imaging technique can image samples with a resolution down to the atomic level (~1 nm). It can determine molecular orientation, identify ordered regions, and determine the size and orientation of features and morphologies at this scale. Unfortunately, transmission electron microscopes are expensive and sample preparation is time-consuming and tedious because specimens must be very thin (~50 nm) and additional steps usually must be performed to increase polymer contrast. There is always the risk of forming artifacts during sample preparation. Much training is required to both obtain and interpret TEM images. Additionally, polymer samples can be easily damaged by the electron beam during imaging (e.g. mass loss, cross-linking, chain scission, dimensional changes, disruption of crystallinity). This radiation damage may limit the resolution

obtainable with TEM, but it may be mitigated by cooling the specimen and increasing the accelerating voltage. Despite the challenges of this microscopy method, TEM is still a powerful technique to image the bulk of polymers.

1.4.3 Tensile (stress-strain) testing

Tensile or stress-strain testing is one of several mechanical tests that can be performed to characterize the stiffness and strength of a polymer and predict when it may fail in a given application [135]. During a stress-strain test, a polymer sample is deformed at a constant elongation rate and the stresses that result from the deformation are simultaneously recorded. Sample geometry can either be in the shape of a rectangular strip or dogbone with a rectangular or circular cross-section. The dogbone geometry (Figure 1.20) is preferable because stresses concentrate in the narrower midsection, improving the accuracy of the stresses measured and increasing the probability of a tensile break in the narrower section of the sample.

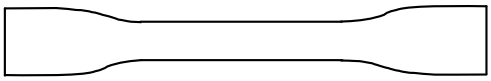

Figure 1.20. Dogbone sample geometry

The specimen is clamped at both ends and one end is pulled at a constant rate of elongation. A load cell at one end measures the load or stress as the sample elongates. Typical data obtained from stress-strain experiments are engineering (nominal) stress (σ) vs. engineering (nominal) strain (ε). Engineering stress is defined as the ratio of the applied load (F) to the original specimen cross-sectional area (A_0):

$$\sigma = F/A_0 \tag{8}$$

Engineering strain is defined as the ratio of the change in gauge length (distance between clamps) (ΔL) over the original gauge length (L_0):

$$\varepsilon = \Delta L/L_0 = (L - L_0) / L_0 \tag{9}$$

Engineering strain can be expressed as percent elongation by multiplying by 100%. A mechanical, electronic, or optical extensometer (strain gauge) may be used to measure instantaneous strain during testing. If this is done, data can be reported in terms of true strain, the sum of all instantaneous length changes divided by the instantaneous length.

The behavior of a polymer subjected to tensile testing depends on the strain applied and the polymer material itself [135]. At low strains, most polymers respond elastically; the

deformation is reversible when the strain is removed and the magnitudes of stress and strain are linearly proportional. This proportionality, known as Hooke's law, results in the ratio of stress over strain yielding a constant known as the elastic, or Young's, modulus. This modulus is the initial slope of the curve obtained by plotting stress versus strain (Figure 1.21). As the strain increases, polymers may display strain-induced softening as their chains uncoil and straighten. The slope of the graph will decrease, but the deformation is still reversible. At some point as the strain applied to the material increases, the deformation will exceed the reversible limit and the polymer will either break if brittle or yield if ductile. If the material yields, the stress-strain curve reaches a maximum, called the yield point. The strain at the yield point is the elongation at yield and the stress is known as the yield stress (σ_y), or upper yield stress. The specimen becomes permanently deformed as its chains slide past each other and it undergoes "necking," observed as a decrease in cross-sectional area usually somewhere in its midsection, and the stress decreases to the drawing stress, or lower yield stress. Local stress increases at the necking region because of the decrease in load-bearing cross-sectional area. Amorphous polymer chains in the necking region change conformation and orient in the direction of the tensile stress. These extended chains resist further deformation, a phenomenon called strain-hardening. If the resistance from strain hardening is larger or equal to the increased stress in the necking region, continued deformation of the sample will occur only by the necking region spreading along the sample, a process called cold drawing. If the local stress in the necking region exceeds the hardening resistance, the necking region will continue to narrow and result in a failure at that location. The stress at which a material breaks (fractures) is called the tensile strength (σ_B) or ultimate strength and the strain is called the elongation at break.

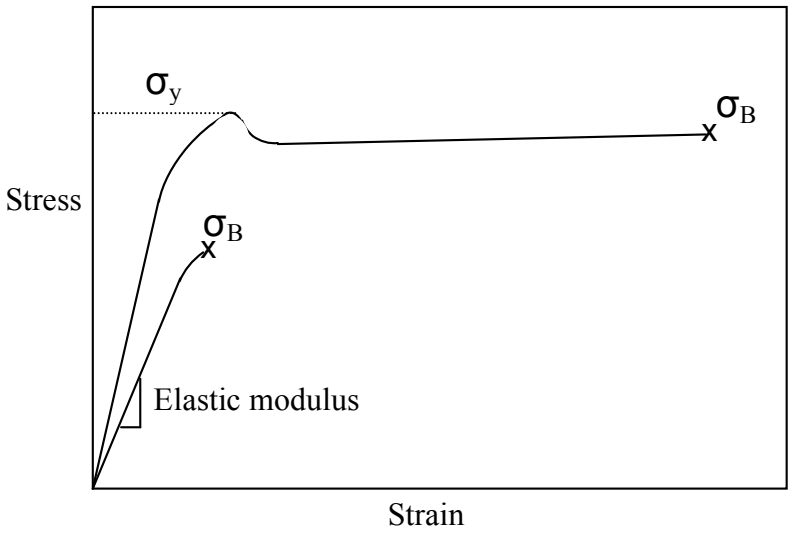

Figure 1.21. Stress-strain curves for both ductile (top curve) and brittle (bottom curve) materials

There are five main nonlinear viscoelastic properties of a material that can be evaluated from its stress-strain curve obtained by tensile testing [136]. *Stiffness* is the ability to bear stress without changing dimension, measured by the magnitude of the elastic modulus in the linear viscoelastic portion of the curve. The steeper the linear part of the curve, the stiffer the material. *Elasticity* is the ability to deform reversibly (bear stress without permanently deforming), determined by the yield point or elastic limit. The length of the horizontal portion of a material after this point is an indicator of its degree of ductility. *Resilience* is the ability to absorb stress without permanently deforming. The area under the elastic portion of the curve is reported as the resilient energy. *Strength* indicates the ability to bear dead load, represented by the stress at which the material breaks (tensile strength, σ_B). *Toughness* is a measure of the ability to absorb energy per unit volume and undergo a large amount of permanent deformation without breaking. It is measured as the area under the stress-strain curve.

1.4.4 Field emission-scanning electron microscopy (FE-SEM)

Field emission-scanning electron microscopy (FE-SEM) operates similarly to traditional scanning electron microscopy (SEM). The primary difference between FE-SEM and SEM is how each microscope generates electrons to produce its electron beam [137]. Traditional SEMs produce electrons by heating a filament of tungsten or LaB_6 until the electrons boil off the filament and shower down upon a specimen. FE-SEM, however, employs a field emission electron source that applies a high voltage directly to a sharp point, extracting electrons directly

from that point. This increases the useful magnification of an SEM by an order of magnitude because of the small diameter of the point and the coherence of the electron beam.

Apart from its electron source, FE-SEM operates similarly to traditional SEM (Figure 1.22) [77]. After an electron beam is emitted from the filament at the top of the microscope, it is focused as it passes down through a series of magnetic lenses and coils. A final aperture narrows the beam diameter right before the beam contacts the specimen in the vacuum which is large enough to accommodate samples several inches in diameter.

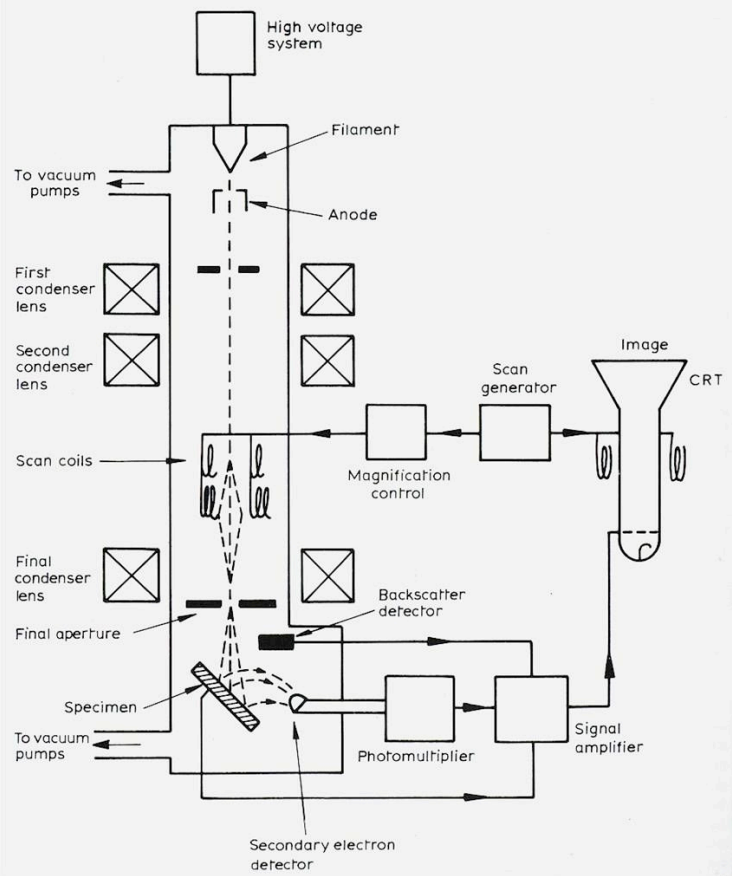

Figure 1.22. Schematic drawing of a scanning electron microscope (SEM). Reprinted from [77] with kind permission of Springer Science and Business Media.

As the beam scans across the surface of the specimen, it interacts with the top layer of the specimen, creating three different types of radiation: secondary electrons, backscattered electrons, and x-rays (Figure 1.23). The primary electrons from the beam excite the atoms in the top few nanometers (5 to 50 nm) of the specimen, causing them to emit low energy electrons (<50 eV) called secondary electrons. At the same time that secondary electrons are emitted, some of the beam electrons are scattered by specimen nuclei at depths of 1 μm or more (*R(B)* in

Figure 1.4.10) and escape as backscattered electrons. X-rays are simultaneously emitted from even greater depths in a specimen (~5 μm; *R(x)* in Figure 1.23) during scanning.

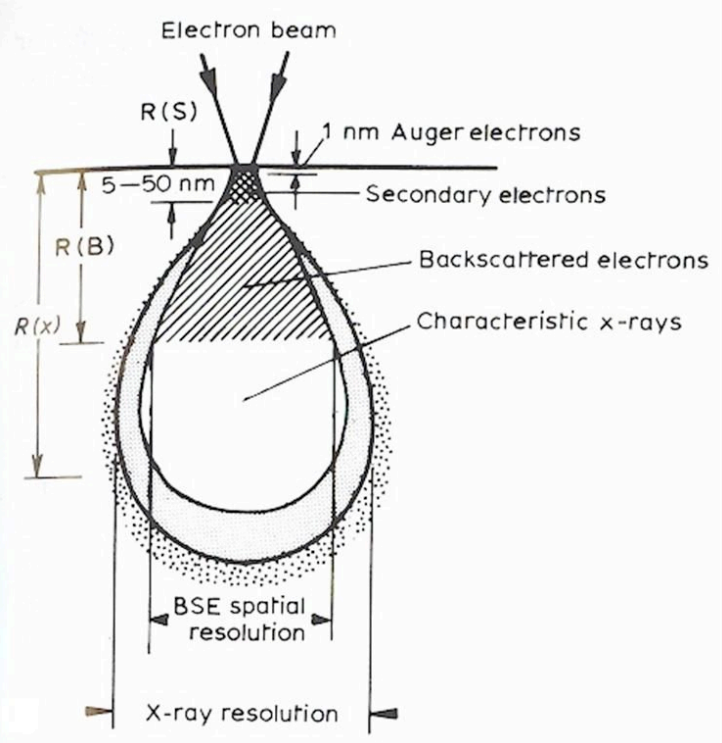

Figure 1.23. Types and origin of radiation emitted when an incident SEM electron beam interacts with a solid sample. Reprinted from [77] with kind permission of Springer Science and Business Media.

Two kinds of x-rays are emitted when a high energy electron beam interacts with a sample: characteristic x-rays and continuum x-rays [77]. Characteristic x-rays are produced after an inner shell electron of an atom has been ejected by the electron beam when the excited atom returns to its ground state. These x-rays, which form sharp peaks in the x-ray spectrum, contain analytical information about the atoms from which they are generated in the form of well defined energies characteristic of the atoms. Continuum x-rays cannot be used to analyze atoms within a specimen because they are formed when the high energy beam electrons are scattered near the atomic nucleus. These x-rays form the background of the x-ray energy spectrum because they have a wide range of energies.

The size of region from which a signal originates will limit the spatial resolution (i.e. the minimum distance between two object features at which they can still be observed as two features) of the image derived from that signal. As the size of the region increases, the spatial resolution of the generated image will decrease. This region is part of the entire region in which

the incident beam interacts with the specimen, called the interaction volume. The interaction volume will vary with beam intensity and sample chemistry. It is expected to increase as sample atomic number decreases and also as accelerating voltage increases [138-140].

The radiation emitted as the electron beam interacts with the sample can be used to form images of the specimen [77]. Separate detectors are mounted within the SEM to collect each of the signals emitted by the specimen during scanning. A secondary electron detector collects secondary electrons to yield surface topography information. These electrons provide the highest resolution images obtainable from the microscope (~5 nm) because they originate from an area the size of the electron beam. The images appear as if they are viewed from the location of the scanning electron beam, but appear as if they are illuminated from the location of the electron detector. A backscattered electron detector collects backscattered electrons and can be used to create topographic contrast images, but these images have a decreased resolution of only 1 μm because the electrons escape from a larger area than the secondary electrons. Two backscattered electron detectors placed close to the sample are usually required to generate a good image without excessively stark contrast. Backscattered electrons can also provide atomic number contrast image because the fraction of these electrons that escape will vary by atom (e.g. 0.06 for carbon to 0.5 for gold [138]). In addition, x-rays can be used to identify the chemical composition of the specimen through either of two detectors: an energy dispersive x-ray spectrometer (EDS) or a wavelength dispersive x-ray spectrometer (WDS). In an EDS, a solid state, lithium drifted silicon detector is used to sense the x-rays, which produce current pulses in proportion to their energy. These pulses are displayed as an energy spectrum after being amplified and sorted by size with a multichannel analyzer. The spectrum contains peaks from all elements larger than sodium (atomic number 11) and may suffer from elemental overlap. Elemental overlap is minimized in a WDS because it separates x-rays of different wavelengths using a bent crystal, resulting in a high signal to noise ratio. Only wavelengths that obey Bragg's law are reflected by the crystal, allowing specific wavelengths from one element at a time to be detected individually as the crystal is rotated. Several crystals are necessary to detect a range of elements.

The operating parameters of the SEM that affect resolution include beam current, beam voltage, final aperture size, and working distance (the distance between the detector and the specimen) [77]. Maximum resolution can be obtained by using a high accelerating voltage, a

small probe size (which requires a small final aperture size and working distance and low beam current), and a slow scan rate (it is necessary to keep noise low because the beam current is low) [77]. Sample placement for maximum resolution in a FE-SEM is inside the lens, which different to sample placement for SEM.

Sample preparation for SEM is relatively simple compared to other microscopy methods, provided that samples can withstand drying and high vacuum [77]. The main goal of sample preparation for SEM is to make samples conductive to prevent them from charging as they are bombarded by electrons during imaging. This is typically achieved by sputter coating samples under vacuum with a nanoscale coating of conductive metal (e.g. palladium or gold). Samples that cannot be sputter coated may be scanned with low accelerating voltages ($\leq$ 5 keV) to slow the rate of charging.

FE-SEM is advantageous for several reasons [77]. In addition to ease of sample preparation, an FE-SEM can be easily operated and attractive images obtained with a brief amount of training. This is only advantageous, however, provided that one realizes the ability to interpret the images is important because even attractive images may contain artifacts or fail to reveal data of interest. The advantages of FE-SEM images include their three-dimensional appearance and large depth of field (i.e. the depth or thickness of a specimen that is simultaneously in focus; e.g. 20 µm at 5000x). Additionally, FE-SEM yields better resolution than SEM (<1 nm vs. 10nm) and it is less expensive than transmission electron microscopy (TEM).

There are a few disadvantages to using FE-SEM/SEM [77]. The sample may be modified by either the vacuum within the microscope chamber or by the electron beam. This microscopy method can only be used with specimens that can withstand the vacuum within the system. Samples containing fluid or gas, including some biological specimens, cannot be imaged under vacuum with SEM. If a non-conductive sample or one that is not properly grounded is imaged with SEM, the electrons from the scanning electron beam will collect on the sample surface and gradually "charge" the sample by increasing the charge on its surface. This can create artifacts because as charging of a sample increases, the secondary electron detector senses more electrons and the image brightness increases. Charging may also cause the sample image to appear to move or undulate even though the sample remains stationary. Another disadvantage of SEM imaging is possible damage to the sample by the electron beam. Caution

must be taken with polymer samples that are sensitive to beam damage because they may crack and degrade at high accelerating voltages. Low accelerating voltages (≤5 keV) must be used with these sample types to minimize beam damage. Finally, SEM is limited because it can only provide detail of the exterior of the sample imaged. Although SEM cannot probe into the interior or bulk of a specimen during imaging, this information can be obtained via TEM.

1.5 References

1. Winter, M. and R.J. Brodd, *What are batteries, fuel cells, and supercapacitors?* Chemical Reviews, 2004. **104**(10): 4245-4269.

2. Kreuer, K.D., S.J. Paddison, E. Spohr, and M. Schuster, *Transport in proton conductors for fuel-cell applications: Simulations, elementary reactions, and phenomenology.* Chemical Reviews, 2004. **104**(10): 4637-4678.

3. Liebhafsky, H.A. and E.J. Cairns, *Fuel cells and fuel batteries: A guide to their research and development*. 1968, New York: John Wiley & Sons.

4. Fuller, T.F., *Is a fuel cell in your future?* The Electrochemical Society Interface, 1997: 26-32.

5. Bacon, F.T., *Fuel cells, past, present and future.* Electrochimica Acta, 1969. **14**(7): 569-585.

6. Appleby, A.J., *From Sir William Grove to today - fuel-cells and the future.* Journal of Power Sources, 1990. **29**(1-2): 3-11.

7. Perry, M.L. and T.F. Fuller, *A historical perspective of fuel cell technology in the 20th century.* Journal of the Electrochemical Society, 2002. **149**(7): S59-S67.

8. Grubb, W.T., *Fuel cell*. 1959, General Electric Company: USA.

9. Grubb, W.T. and L.W. Niedrach, *Batteries with solid ion-exchange membrane electrolytes II. Low-temperature hydrogen-oxygen fuel cells.* Journal of the Electrochemical Society, 1960. **107**(2): 131-135.

10. Hickner, M.A., H. Ghassemi, Y.S. Kim, B.R. Einsla, and J.E. McGrath, *Alternative polymer systems for proton exchange membranes (PEMs).* Chemical Reviews, 2004. **104**(10): 4587-4611.

11. *R&D plan for the high temperature membrane working group*. 2003, Department of Energy Office of Efficiency and Renewable Energy's Hydrogen, Fuel Cells & Infrastructure Technologies Program

12. Mauritz, K.A. and R.B. Moore, *State of understanding of Nafion.* Chemical Reviews, 2004. **104**(10): 4535-4585.

13. Beckerbauer, R., *Unsaturated α-hydroperfluoroalkylsulfonyl fluorides*. 1973, E. I. du Pont de Nemours and Company, Wilmington, DE: U.S.

14. Grot, W.G., *CF_2=$CFCF_2CF_2SO_2F$ and derivatives and polymers thereof*. 1973, E. I. du Pont de Nemours and Company, Wilmington, DE: U.S.

15. Grot, W.G., *Process for making liquid composition of perfluorinated ion exchange polymer, and product thereof*. 1984, E. I. du Pont de Nemours and Company, Wilmington, DE: U.S.

16. Zaluski, C. and G. Xu, *Blends of Nafion and Dow perfluorosulfonated ionomer membranes.* Macromolecules, 1994. **27**(23): 6750-6754.

17. Miyatake, K. and M. Watanabe, *Recent progress in proton conducting membranes for PEFCs.* Electrochemistry, 2005. **73**(1): 12-19.

18. Meier-Haack, J., A. Taeger, C. Vogel, K. Schlenstedt, W. Lenk, and D. Lehmann, *Membranes from sulfonated block copolymers for use in fuel cells.* Separation and Purification Technology, 2005. **41**(3): 207-220.

19. Wang, S. and J.E. McGrath, *Synthesis of poly(arlene ethers)s*, in *Synthetic methods in step-growth polymers*, M.E. Rogers and T.E. Long, Editors. 2003, Wiley: Hoboken, NJ. p. 327.

20. Noshay, A. and L.M. Robeson, *Sulfonated polysulfone.* Journal of Applied Polymer Science, 1976. **20**(7): 1885-1903.

21. Genova-Dimitrova, P., B. Baradie, D. Foscallo, C. Poinsignon, and J.Y. Sanchez, *Ionomeric membranes for proton exchange membrane fuel cell (PEMFC): Sulfonated polysulfone associated with phosphatoantimonic acid.* Journal of Membrane Science, 2001. **185**(1): 59-71.

22. Robeson, L.M. and M. Matzner, *Flame retardant polyarylate compositions*. Patent No. 4,380,598. 1983, Union Carbide Corporation: USA.

23. Ueda, M., H. Toyota, T. Ouchi, J.I. Sugiyama, K. Yonetake, T. Masuko, and T. Teramoto, *Synthesis and characterization of aromatic poly(ether sulfone)s containing pendant sodium-sulfonate groups.* Journal of Polymer Science Part a-Polymer Chemistry, 1993. **31**(4): 853-858.

24. Harrison, W.L., F. Wang, J.B. Mecham, V.A. Bhanu, M. Hill, Y.S. Kim, and J.E. McGrath, *Influence of the bisphenol structure on the direct synthesis of sulfonated poly(arylene ether) copolymers. I.* Journal of Polymer Science Part a-Polymer Chemistry, 2003. **41**(14): 2264-2276.

25. Kim, Y.S., F. Wang, M. Hickner, S. McCartney, Y.T. Hong, W. Harrison, T.A. Zawodzinski, and J.E. McGrath, *Effect of acidification treatment and morphological stability of sulfonated poly(arylene ether sulfone) copolymer proton-exchange membranes for fuel-cell use above 100 degrees C.* Journal of Polymer Science Part B-Polymer Physics, 2003. **41**(22): 2816-2828.

26. Kim, Y.S., L. Dong, M.A. Hickner, B.S. Pivovar, and J.E. McGrath, *Processing induced morphological development in hydrated sulfonated poly(arylene ether sulfone) copolymer membranes.* Polymer, 2003. **44**(19): 5729-5736.

27. Ghassemi, H., G. Ndip, and J.E. McGrath, *New multiblock copolymers of sulfonated poly(4 '-phenyl-2,5-benzophenone) and poly(arylene ether sulfone) for proton exchange membranes. II.* Polymer, 2004. **45**(17): 5855-5862.

28. Ghassemi, H., J.E. McGrath, and T.A. Zawodzinski, *Multiblock sulfonated-fluorinated poly(arylene ether)s for a proton exchange membrane fuel cell.* Polymer, 2006. **47**(11): 4132-4139.

29. Wang, H., A.S. Badami, A. Roy, and J.E. McGrath, *Multiblock copolymers of poly (2,5-benzophenone) and disulfonated poly (arylene ether sulfone) for proton exchange membranes. I. Synthesis and characterization.* Journal of Polymer Science Part A: Polymer Chemistry, 2006. **45**(2): 284-294.

30. Lee, H.-S., A. Roy, A.S. Badami, and J.E. McGrath, Prepr. Pap. - Am. Chem. Soc., Div. PMSE, 2006. **95**: 210-211.

31. Wilson, A.D. and H.J. Prosser, *Ionic polymers: History, definition, and classification*, in *Developments in ionic polymers-1*, A.D. Wilson and H.J. Prosser, Editors. 1983, Applied Science Publishers: New York. p. 1-34.

32. Eisenberg, A., *Clustering of ions in organic polymers. A theoretical approach.* Macromolecules, 1970. **18**: 284-92.

33. Chanda, M., *Advanced polymer chemistry: A problem solving guide*. 2000, New York: Marcel Dekker. p. 7.

34. Noshay, A. and J.E. McGrath, *Block copolymers: Overview and critical survey*. 1977, New York: Academic Press. 516.

35. Yang, Y. and S. Holdcroft, *Synthetic strategies for controlling the morphology of proton conducting polymer membranes.* Fuel Cells, 2005. **5**(2): 171-186.

36. Mauritz, K.A. and A.J. Hopfinger, *Structural properties of membrane ionomers*, in *Modern aspects of electrochemistry*, J.O.M. Bockris, B.E. Conway, and R.E. White, Editors. 1982, Plenum Press: New York. p. 425-508.

37. Bates, F.S. and G.H. Fredrickson, *Block copolymers - designer soft materials.* Physics Today, 1999. **52**(2): 32-38.

38. Leibler, L., *Theory of microphase separation in block copolymers.* Macromolecules, 1980. **13**(6): 1602-1617.

39. Matsen, M.W. and M. Schick, *Stable and unstable phases of a diblock copolymer melt.* Physical Review Letters, 1994. **72**(16): 2660-2663.

40. Matsen, M.W. and M. Schick, *Stable and unstable phases of a linear multiblock copolymer melt.* Macromolecules, 1994. **27**(24): 7157-7163.

41. Matsen, M.W. and M. Schick, *Microphase separation in starblock copolymer melts.* Macromolecules, 1994. **27**(23): 6761-6767.

42. Khandpur, A.K., S. Forster, F.S. Bates, I.W. Hamley, A.J. Ryan, W. Bras, K. Almdal, and K. Mortensen, *Polyisoprene-polystyrene diblock copolymer phase diagram near the order-disorder transition.* Macromolecules, 1995. **28**(26): 8796-8806.

43. Bugner, D.E., *Ab block copolymers containing methacrylic acid and/or metal methacrylate blocks*, in *Chemical reactions on polymers*, J.L. Benham and J.F. Kinstle, Editors. 1988, American Chemical Society: Washington, D.C. p. 276-290.

44. Allen, R., I. Yilgor, and J.E. McGrath, *Studies on the synthesis of novel block ionomers*, in *Coulombic interactions in macromolecular systems*, A. Eisenberg and F.E. Bailey, Editors. 1986, American Chemical Society: Washington, D. C. p. 79-92.

45. Long, T.E., R.D. Allen, and J.E. McGrath, *Synthesis and characterization of block copolymers containing acid and ionomeric functionalities*, in *Chemical reactions on polymers*, J.L. Benham and J.F. Kinstle, Editors. 1988, American Chemical Society: Washington, D. C. p. 258-275.

46. Venkateshwaran, L.N., G.A. York, C.D. DePorter, J.E. McGrath, and G.L. Wilkes, *Morphological characterization of well defined methacrylic based di- and triblock ionomers.* Polymer, 1992. **33**(11): 2277-2286.

47. Gouin, J.P., C.E. Williams, and A. Eisenberg, *Microphase structure of block ionomers .1. Study of molded styrene 4-vinylpyridinium aba blocks by SAXS and SANS.* Macromolecules, 1989. **22**(12): 4573-4578.

48. Krausch, G., *Surface-induced self-assembly in thin polymer-films.* Materials Science & Engineering R-Reports, 1995. **14**(1-2): 1-94.

49. Lambooy, P., T.P. Russell, G.J. Kellogg, A.M. Mayes, P.D. Gallagher, and S.K. Satija, *Observed frustration in confined block-copolymers.* Physical Review Letters, 1994. **72**(18): 2899-2902.

50. Huinink, H.P., M.A. van Dijk, J.C.M. Brokken-Zijp, and G.J.A. Sevink, *Surface-induced transitions in thin films of asymmetric diblock copolymers.* Macromolecules, 2001. **34**(15): 5325-5330.

51. Fasolka, M.J. and A.M. Mayes, *Block copolymer thin films: Physics and applications.* Annual Review of Materials Research, 2001. **31**: 323-355.

52. Segalman, R.A., K.E. Schaefer, G.H. Fredrickson, E.J. Kramer, and S. Magonov, *Topographic templating of islands and holes in highly asymmetric block copolymer films.* Macromolecules, 2003. **36**(12): 4498-4506.

53. Segalman, R.A., A. Hexemer, and E.J. Kramer, *Effects of lateral confinement on order in spherical domain block copolymer thin films.* Macromolecules, 2003. **36**(18): 6831-6839.

54. Knoll, A., A. Horvat, K.S. Lyakhova, G. Krausch, G.J.A. Sevink, A.V. Zvelindovsky, and R. Magerle, *Phase behavior in thin films of cylinder-forming block copolymers.* Physical Review Letters, 2002. **89**(3).

55. Wang, Q., Q.L. Yan, P.F. Nealey, and J.J. de Pablo, *Monte Carlo simulations of diblock copolymer thin films confined between two homogeneous surfaces.* Journal of Chemical Physics, 2000. **112**(1): 450-464.

56. Wang, Q., P.F. Nealey, and J.J. de Pablo, *Monte Carlo simulations of asymmetric diblock copolymer thin films confined between two homogeneous surfaces.* Macromolecules, 2001. **34**(10): 3458-3470.

57. Koneripalli, N., N. Singh, R. Levicky, F.S. Bates, P.D. Gallagher, and S.K. Satija, *Confined block-copolymer thin-films.* Macromolecules, 1995. **28**(8): 2897-2904.

58. Kellogg, G.J., D.G. Walton, A.M. Mayes, P. Lambooy, T.P. Russell, P.D. Gallagher, and S.K. Satija, *Observed surface energy effects in confined diblock copolymers.* Physical Review Letters, 1996. **76**(14): 2503-2506.

59. Mansky, P., T.P. Russell, C.J. Hawker, M. Pitsikalis, and J. Mays, *Ordered diblock copolymer films on random copolymer brushes.* Macromolecules, 1997. **30**(22): 6810-6813.

60. Fasolka, M.J., P. Banerjee, A.M. Mayes, G. Pickett, and A.C. Balazs, *Morphology of ultrathin supported diblock copolymer films: Theory and experiment.* Macromolecules, 2000. **33**(15): 5702-5712.

61. Pickett, G.T. and A.C. Balazs, *Equilibrium behavior of confined triblock copolymer films.* Macromolecular Theory and Simulations, 1998. **7**(2): 249-255.

62. Sommer, J.U., A. Hoffmann, and A. Blumen, *Block copolymer films between neutral walls: A Monte Carlo study.* Journal of Chemical Physics, 1999. **111**(8): 3728-3732.

63. Sivaniah, E., Y. Hayashi, M. Iino, T. Hashimoto, and K. Fukunaga, *Observation of perpendicular orientation in symmetric diblock copolymer thin films on rough substrates.* Macromolecules, 2003. **36**(16): 5894-5896.

64. Walton, D.G., G.J. Kellogg, A.M. Mayes, P. Lambooy, and T.P. Russell, *A free-energy model for confined diblock copolymers.* Macromolecules, 1994. **27**(21): 6225-6228.

65. Mansky, P., P. Chaikin, and E.L. Thomas, *Monolayer films of diblock copolymer microdomains for nanolithographic applications.* Journal of Materials Science, 1995. **30**(8): 1987-1992.

66. Mansky, P., J. DeRouchey, T.P. Russell, J. Mays, M. Pitsikalis, T. Morkved, and H. Jaeger, *Large-area domain alignment in block copolymer thin films using electric fields.* Macromolecules, 1998. **31**(13): 4399-4401.

67. Brinkmann, S., R. Stadler, and E.L. Thomas, *New structural motif in hexagonally ordered cylindrical ternary (abc) block copolymer microdomains.* Macromolecules, 1998. **31**(19): 6566-6572.

68. Kim, J., B. Kim, B. Jung, Y.S. Kang, H.Y. Ha, I.H. Oh, and K.J. Ihn, *Effect of casting solvent on morphology and physical properties of partially sulfonated polystyrene-block-poly(ethylene-ran-butylene)-block-polystyrene copolymers.* Macromolecular Rapid Communications, 2002. **23**(13): 753-756.

69. Funaki, Y., K. Kumano, T. Nakao, H. Jinnai, H. Yoshida, K. Kimishima, K. Tsutsumi, Y. Hirokawa, and T. Hashimoto, *Influence of casting solvents on microphase-separated structures of poly(2-vinylpyridine)-block-polyisoprene.* Polymer, 1999. **40**(25): 7147-7156.

70. Morrison, F.A. and H.H. Winter, *Effect of unidirectional shear on the structure of triblock copolymers .1. Polystyrene polybutadiene polystyrene.* Macromolecules, 1989. **22**(9): 3533-3540.

71. Kotaka, T., M. Okamoto, A. Kojima, Y.K. Kwon, and S. Nojima, *Elongational flow-induced morphology change of block copolymers. 2. A polystyrene-block-poly(ethylene butylene)-block-polystyrene triblock copolymer with cylindrical microdomains.* Polymer, 2001. **42**(7): 3223-3231.

72. Kotaka, T., M. Okamoto, A. Kojima, Y.K. Kwon, and S. Nojima, *Elongational flow-induced morphology change of block copolymers - part 1. A polystyrene-block-poly(ethylene butylene)-block-polystyrene-block-poly(ethylene butylene) tetrablock copolymer with polystyrene spherical microdomains.* Polymer, 2001. **42**(3): 1207-1217.

73. Kim, G. and M. Libera, *Morphological development in solvent-cast polystyrene-polybutadiene-polystyrene (sbs) triblock copolymer thin films.* Macromolecules, 1998. **31**(8): 2569-2577.

74. Mauritz, K.A., *Morphological theories*, in *Ionomers: Synthesis, structure, properties and applications*, M.R. Tant, K.A. Mauritz, and G.L. Wilkes, Editors. 1997, Chapman & Hall: New York. p. 95-157.

75. Volkenstein, M.B., *Configurational statistics of polymer chains*. 1963, New York: Wiley. 501.

76. Mauritz, K.A., C.J. Hora, and A.J. Hopfinger, *Theoretical model for the structure of ionomers: Application to Nafion materials*, in *Ions in polymers, adv. Chem. Ser.*, A. Eisenberg, Editor. 1980, American Chemical Society: Washington, DC. p. 123-44.

77. Sawyer, L. and D. Grubb, *Polymer microscopy*. 1996, New York: Chapman & Hall.

78. Gierke, T.D., G.E. Munn, and F.C. Wilson, *The morphology in Nafion perfluorinated membrane products, as determined by wide-angle and small-angle X-ray studies.* Journal of Polymer Science Part B-Polymer Physics, 1981. **19**(11): 1687-1704.

79. Lowry, S.R. and K.A. Mauritz, *An investigation of ionic hydration effects in perfluorosulfonate ionomers by fourier-transform infrared-spectroscopy.* Journal of the American Chemical Society, 1980. **102**(14): 4665-4667.

80. Fujimura, M., T. Hashimoto, and H. Kawai, *Small-angle x-ray-scattering study of perfluorinated ionomer membranes .1. Origin of 2 scattering maxima.* Macromolecules, 1981. **14**(5): 1309-1315.

81. Starkweather, H.W., *Crystallinity in perfluorosulfonic acid ionomers and related polymers.* Macromolecules, 1982. **15**(2): 320-323.

82. Forsman, W.C., *Effect of segment - segment association on chain dimensions.* Macromolecules, 1982. **15**(4): 1032-1040.

83. Hsu, W.Y. and T.D. Gierke, *Elastic theory for ionic clustering in perfluorinated ionomers.* Macromolecules, 1982. **15**(1): 101-105.

84. Hsu, W.Y. and T.D. Gierke, *Ion-transport and clustering in Nafion perfluorinated membranes.* Journal of Membrane Science, 1983. **13**(3): 307-326.

85. Mauritz, K.A. and C.E. Rogers, *A water sorption isotherm model for ionomer membranes with cluster morphologies.* Macromolecules, 1985. **18**(3): 483-491.

86. Yeager, H.L. and A. Steck, *Cation and water diffusion in Nafion ion-exchange membranes - influence of polymer structure.* Journal of the Electrochemical Society, 1981. **128**(9): 1880-1884.

87. MacKnight, W.J., W.P. Taggart, and R.S. Stein, Journal of Polymer Science Polymer Symposium, 1974. **45**: 113.

88. Roche, E.J., R.S. Stein, T.P. Russell, and W.J. Macknight, *Small-angle x-ray-scattering study of ionomer deformation.* Journal of Polymer Science Part B-Polymer Physics, 1980. **18**(7): 1497-1512.

89. Fujimura, M., T. Hashimoto, and H. Kawai, *Small-angle x-ray-scattering study of perfluorinated ionomer membranes .2. Models for ionic scattering maximum.* Macromolecules, 1982. **15**(1): 136-144.

90. Roche, E.J., M. Pineri, and R. Duplessix, *Phase-separation in perfluorosulfonate ionomer membranes.* Journal of Polymer Science Part B-Polymer Physics, 1982. **20**(1): 107-116.

91. Dreyfus, B., G. Gebel, P. Aldebert, M. Pineri, M. Escoubes, and M. Thomas, *Distribution of the micelles in hydrated perfluorinated ionomer membranes from SANS experiments.* Journal De Physique, 1990. **51**(12): 1341-1354.

92. Litt, M., *A reevaluation of Nafion(r) morphology.* Abstracts of Papers of the American Chemical Society, 1997. **213**: 33-POLY.

93. Gebel, G. and R.B. Moore, *Small-angle scattering study of short pendant chain perfuorosulfonated ionomer membranes.* Macromolecules, 2000. **33**(13): 4850-4855.

94. Haubold, H.G., T. Vad, H. Jungbluth, and P. Hiller, *Nano structure of Nafion: A SAXS study.* Electrochimica Acta, 2001. **46**(10-11): 1559-1563.

95. Gebel, G., *Structural evolution of water swollen perfluorosulfonated ionomers from dry membrane to solution.* Polymer, 2000. **41**(15): 5829-5838.

96. Rubatat, L., A.L. Rollet, G. Gebel, and O. Diat, *Evidence of elongated polymeric aggregates in Nafion.* Macromolecules, 2002. **35**(10): 4050-4055.

97. Rollet, A.L., G. Gebel, J.P. Simonin, and P. Turq, *A SANS determination of the influence of external conditions on the nanostructure of Nafion membrane.* Journal of Polymer Science Part B-Polymer Physics, 2001. **39**(5): 548-558.

98. Yang, Y.S., Z.Q. Shi, and S. Holdcroft, *Synthesis of sulfonated polysulfone-block-pvdf copolymers: Enhancement of proton conductivity in low ion exchange capacity membranes.* Macromolecules, 2004. **37**(5): 1678-1681.

99. Genies, C., R. Mercier, B. Sillion, N. Cornet, G. Gebel, and M. Pineri, *Soluble sulfonated naphthalenic polyimides as materials for proton exchange membranes.* Polymer, 2001. **42**(2): 359-373.

100. Guo, X.X., J.H. Fang, T. Watari, K. Tanaka, H. Kita, and K.I. Okamoto, *Novel sulfonated polyimides as polyelectrolytes for fuel cell application. 2. Synthesis and proton conductivity, of polyimides from 9,9-bis(4-aminophenyl)fluorene-2,7-disulfonic acid.* Macromolecules, 2002. **35**(17): 6707-6713.

101. Cornet, N., O. Diat, G. Gebel, F. Jousse, D. Marsacq, R. Mercier, and M. Pineri, *Sulfonated polyimide membranes: A new type of ion-conducting membrane for electrochemical applications.* Journal of New Materials for Electrochemical Systems, 2000. **3**(1): 33-42.

102. Won, J., H.H. Park, Y.J. Kim, S.W. Choi, H.Y. Ha, I.H. Oh, H.S. Kim, Y.S. Kang, and K.J. Ihn, *Fixation of nanosized proton transport channels in membranes.* Macromolecules, 2003. **36**(9): 3228-3234.

103. Ding, J.F., C. Chuy, and S. Holdcroft, *Solid polymer electrolytes based on ionic graft polymers: Effect of graft chain length on nano-structured, ionic networks.* Advanced Functional Materials, 2002. **12**(5): 389-394.

104. Ding, J.F., C. Chuy, and S. Holdcroft, *A self-organized network of nanochannels enhances ion conductivity through polymer films.* Chemistry of Materials, 2001. **13**(7): 2231-2233.

105. Drzewinski, M. and W.J. MacKnight, *Structure and properties of sulfonated polysulfone ionomers.* Journal of Applied Polymer Science, 1985. **30**(12): 4753-4770.

106. Yeo, S.C. and A. Eisenberg, *Physical-properties and supermolecular structure of perfluorinated ion-containing (Nafion) polymers.* Journal of Applied Polymer Science, 1977. **21**(4): 875-898.

107. Hodge, I.M. and A. Eisenberg, *Dielectric and mechanical relaxations in a Nafion precursor.* Macromolecules, 1978. **11**(2): 289-293.

108. Nakano, Y. and W.J. MacKnight, *Dynamic mechanical properties of perfluorocarboxylate ionomers.* Macromolecules, 1984. **17**(8): 1585-1591.

109. Hara, M. and P. Jar, *Effect of ionic aggregates on the fatigue properties of ionomers.* Polymer Communications, 1987. **28**(2): 52-54.

110. Hara, M., P.Y. Jar, and J.A. Sauer, *Fatigue behavior of ionomers .1. Ion content effect on sulfonated polystyrene ionomers.* Macromolecules, 1988. **21**(11): 3183-3186.

111. Hara, M., P. Jar, and J.A. Sauer, *Fatigue behavior of ionomers .3. Effect of excess neutralizing agent on sulfonated polystyrene ionomers.* Macromolecules, 1990. **23**(23): 4964-4969.

112. Hara, M., P. Jar, and J.A. Sauer, *Fatigue behavior of ionomers .2. Effect of counterion on sulfonated polystyrene ionomers.* Macromolecules, 1990. **23**(20): 4465-4469.

113. Eisenberg, A. and M. Navratil, *Ion clustering and viscoelastic relaxation in styrene-based ionomers. II. Effect of ion concentration.* Macromolecules, 1973. **6**: 604-612.

114. Ward, T.C. and A.V. Tobolsky, *Viscoelastic study of ionomers.* Journal of Applied Polymer Science, 1967. **11**: 2403-2415.

115. Eisenberg, A., H. Matsuura, and T. Tsutsui, *Glass transition in ionic polymers: The acrylates.* Journal of Polymer Science Part A-Polymer Chemistry, 1971. **9**: 2131-2135.

116. Eisenberg, A. and M. Navratil, *Ion clustering and viscoelastic relaxation in styrene-based ionomers. IV. X-ray and dynamic mechanical studies.* Macromolecules, 1974. **7**: 90-94.

117. Matsuura, H. and A. Eisenberg, *Glass transitions of ethyl acrylate-based ionomers.* Journal of Polymer Science Part B-Polymer Physics, 1976. **14**(7): 1201-1209.

118. Mattera, V.D. and W.M. Risen, *Composition dependence of glass-transition temperature of sulfonated-polystrene ionomers.* Journal of Polymer Science Part B-Polymer Physics, 1986. **24**(4): 753-760.

119. Yang, S., K. Sun, and W.M. Risen, *Preparation and thermal characterization of the glass-transition temperatures of sulfonated polystyrene metal ionomers.* Journal of Polymer Science Part B-Polymer Physics, 1990. **28**(10): 1685-1697.

120. Jérôme, R., J. Horrion, R. Fayt, and P. Teyssié, *Halato-telechelic polymers .10. Effect of the ionic end groups on the glass-transition temperature.* Macromolecules, 1984. **17**(11): 2447-2450.

121. Moore, R.B. and C.R. Martin, *Morphology and chemical properties of the Dow perfluorosulfonate ionomers.* Macromolecules, 1989. **22**(9): 3594-3599.

122. Moore, R.B. and C.R. Martin, *Chemical and morphological properties of solution-cast perfluorosulfonate ionomers.* Macromolecules, 1988. **21**(5): 1334-1339.

123. Bazuin, C.G. and A. Eisenberg, *Modification of polymer properties through ion incorporation.* Industrial & Engineering Chemistry Product Research and Development, 1981. **20**(2): 271-286.

124. Kyu, T., M. Hashiyama, and A. Eisenberg, *Dynamic mechanical studies of partially ionized and neutralized Nafion polymers.* Canadian Journal of Chemistry-Revue Canadienne De Chimie, 1983. **61**(4): 680-687.

125. Kyu, T. and A. Eisenberg, *Mechanical relaxations in perfluorosulfonate-ionomer membranes.* ACS Symposium Series, 1982. **180**: 79-110.

126. Gauthier, S., D. Duchesne, and A. Eisenberg, *Vinylpyridinium ionomers .1. Influence of the structure of the ion on the state of aggregation in random styrene-based systems.* Macromolecules, 1987. **20**(4): 753-759.

127. Page, K.A., K.M. Cable, and R.B. Moore, *Molecular origins of the thermal transitions and dynamic mechanical relaxations in perfluorosulfonate ionomers.* Macromolecules, 2005. **38**(15): 6472-6484.

128. Tant, M.R. and G.L. Wilkes, *Structure and properties of hydrocarbon-based ionomers*, in *Ionomers: Synthesis, structure, properties and applications*, M.R. Tant, K.A. Mauritz, and G.L. Wilkes, Editors. 1997, Chapman & Hall: New York. p. 261-289.

129. Moore, R.B., *Chemical and morphological investigations of perfluorosulfonate ionomers.* 1988, Texas A&M University.

130. Robertson, M.A.F. and H.L. Yeager, *Structure and properties of perfluorinated ionomers*, in *Ionomers: Synthesis, structure, properties and applications*, M.R. Tant, K.A. Mauritz, and G.L. Wilkes, Editors. 1997, Chapman & Hall: New York. p. 290-330.

131. Eisenberg, A., in *Physical properties of polymers*, J.E. Mark, A. Eisenberg, W.W. Graessley, L. Mandelkern, and J.L. Koeing, Editors. 1984, American Chemical Society: Washington, D.C. p. 55-96.

132. Jalili, N. and K. Laxminarayana, *A review of atomic force microscopy imaging systems: Application to molecular metrology and biological sciences.* Mechatronics, 2004. **14**(8): 907-945.

133. Overney, R.M. and V.V. Tsukruk, *Scanning probe microscopy in polymers: Introductory notes*, in *Scanning probe microscopy of polymers*, B.D. Ratner and V.V. Tsukruk, Editors. 1998, American Chemical Society: Washington, D.C. p. 2-30.

134. Ceynowa, J., *Electron-microscopy investigation of ion-exchange membranes.* Polymer, 1978. **19**(1): 73-76.

135. Ebewele, R.O., *Polymer science and technology*. 2000, New York: CRC Press. 343-387.

136. Williams, D.J., *Polymer science and engineering*. 1971, Englewood Cliffs, NJ: Prentice-Hall. 401.

137. Available from: http://www.emu0.emu.uct.ac.za/EMforBiologists/lecture2/Lecture-2.htm.

138. Goldstein, J.I., D.E. Newbury, P. Echlin, D.C. Joy, A.D. Romig Jr., C.E. Lyman, C. Fiori, and E. Lifshin, *Scanning electron microscopy and x-ray microanalysis: A text for biologists, materials scientists, and geologists*. 2nd ed. 1992, New York: Plenum. 820.

139. Reimer, L., *Scanning electron microscopy: Physics of image formation and microanalysis*. 2nd ed. Optical sciences, ed. A.L. Schawlow, A.E. Siegman, and T. Tamir. Vol. 45. 1998, New York: Springer. 527.

140. Newbury, D.E., D.C. Joy, P. Echlin, C. Fiori, and J.I. Goldstein, *Advanced scanning electron microscopy and X-ray microanalysis*. 1986, New York: Plenum.

Chapter 2. Molecular Weight Effects upon Poly(arylene ether sulfone)-Based Random and Multiblock Copolymers for Fuel Cells

Anand S. Badami,[1] Hae-Seung Lee,[1] Yanxiang Li,[1,2] Abhishek Roy,[1] Hang Wang,[1,3] and James E. McGrath[1]

[1]*Department of Chemistry, Macromolecular Science and Engineering Program, Macromolecules and Interfaces Institute, Virginia Polytechnic Institute and State University, Blacksburg, VA 24061, USA*

[2]*Present Address: The Dow Chemical Company, 1710 Building, Midland, MI 48674*

[3]*Present Address: Celanese Corporation, 8040 Dixie Highway, Florence, KY 41042*

Abstract

The realization of proton exchange membrane (PEM) fuel cells as commercially available energy conversion sources depends largely upon the development of PEMs whose properties are enhanced over current perfluorinated sulfonic acid PEMs. Essential to this effort is the understanding of how a membrane's molecular weight and morphology affect its relevant performance properties like proton conductivity and hydrolytic stability. The present study evaluates the effect of molecular weight and block length upon both the morphologies and membrane properties of two random copolymer series and two multiblock copolymer series, respectively, all based on disulfonated poly(arylene ether sulfone) copolymers. Changes in molecular weight appear to have little effect on the phase separated morphologies, water uptake, and proton conductivities of random copolymers. Changes in block length do, however, have a pronounced effect on multiblock copolymers, affecting surface and bulk morphologies as well as water uptake, proton conductivity, and hydrolytic stability. The multiblock membrane properties affected by block length appear to improve as the degree of nanophase separation increases, suggesting that PEM properties may be optimized by changes in morphology.

2.1 Introduction

The need to reduce our nation's dependence upon foreign oil is well-recognized. A long-term solution to this problem may be proton exchange membrane (PEM) fuel cells. These can be

quite efficient (60-70% or more) electrochemical energy conversion devices which do not need recharging like batteries because their fuel and oxidant are continuously supplied from an external source [1, 2]. Applications for PEM fuel cells range from automobiles, stationary power for homes and other buildings, and portable electronic devices. At the heart of every PEM fuel cell is a proton exchange membrane flanked by two electrodes, whose main function is to conduct protons from the anode to the cathode and provide a barrier between the fuel and oxidant gases. In addition to high protonic conductivity and low fuel and oxidant permeability, there are several other characteristics a PEM must possess to be viable including good mechanical properties, hydrolytic stability, and cost effectiveness [3].

The current state-of-the-art PEM material is Nafion®, a poly(perfluorosulfonic acid) manufactured by the E. I. duPont Company [4]. Despite its good proton conductivity, chemical stability, and mechanical stability, Nafion®'s limitations, which include cost and fuel permeability, have prompted research into alternative PEM materials [3, 5]. A promising alternative to Nafion® may be the disulfonated poly(arylene ether sulfone) (or biphenol sulfone in the acid (H) form; BPSH) copolymers, which display good chemical/mechanical stability and proton conductivity, as well as reduced fuel permeability [3, 6, 7]. It is anticipated that sulfonated poly(arylene ether sulfone) copolymers synthesized with fluorinated comonomer (4,4'-hexafluoroisopropylidene diphenol or 6F-bisphenol; 6FSH) possess the positive membrane characteristics of BPSH copolymers and also bond well to Nafion® electrodes.

Copolymerizing highly hydrophilic BPSH with hydrophobic oligomers into multiblock copolymers may be an additional way to optimize membrane properties. Multiblock copolymers based on BPSH-type copolymers have been shown to display higher proton conductivity at low relative humidity than random BPSH copolymers [8-13]. It is expected that changes in multiblock copolymer synthesis can be used to control nanophase-separated morphology and membrane properties like water uptake and mechanical strength.

While it is well accepted that molecular weight will directly influence PEM mechanical properties, the influence of molecular weight or block length upon morphology and other membrane properties, such as proton conductivity and water uptake, has not been well-characterized. The present study has investigated the effect of molecular weight upon the morphologies and membrane properties of two random copolymer series (BPSH and 6FSH; Figure 2.1) and the effect of block length upon the morphologies and membrane properties of

two multiblock copolymer series containing BPSH (Figure 2.2). The first series is comprised of BPSH and naphthalene-based polyimide oligomers at three different block lengths. The second series is comprised of BPSH and poly(2,5-benzophenone) oligomers at two different block lengths.

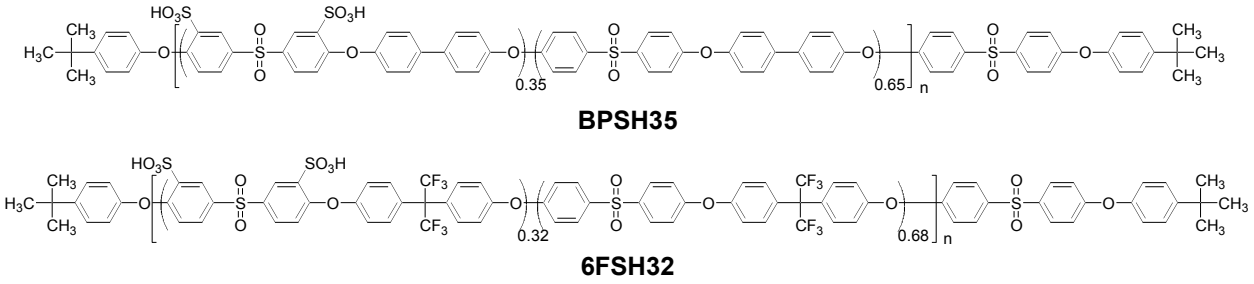

Figure 2.1. Chemical structure of BPSH35 (top) and 6FSH32 (bottom) copolymers.

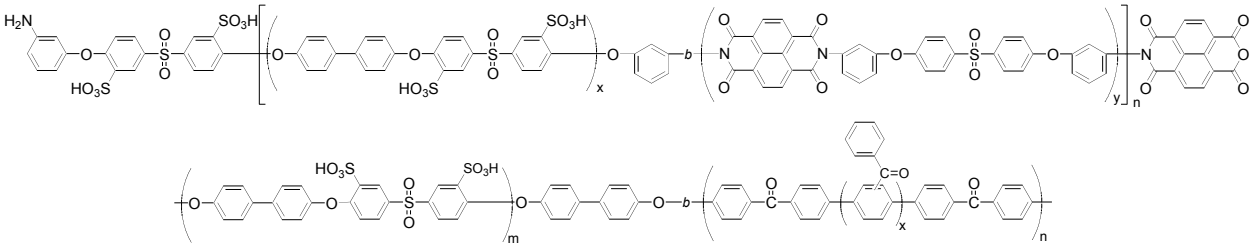

Figure 2.2. Chemical structure of $BPSH100_x$-PI_y (top) and $BPSH100_x$-PBP_y (bottom) multiblock copolymers.

To achieve the goals of this study, number average molecular weights for random copolymers and block lengths for the oligomers which were coupled into multiblock copolymers were determined by ^{1}H-NMR or ^{13}C-NMR. Molecular weight values were compared against intrinsic viscosity values to ensure accuracy. Measurements were made of both the proton conductivity in liquid water and the water uptake of the membranes. The values of these membrane properties were evaluated alongside of surface morphology images obtained by atomic force microscopy. In the case of the multiblock copolymers, they were also evaluated with bulk morphology images obtained by transmission electron microscopy. Dynamic mechanical analysis was employed to gain insight about the effect of molecular weight and block length upon the viscoelastic behavior of the membranes.

2.2 Experimental

2.2.1 Materials

Non- and partially-fluorinated disulfonated poly(arylene ether sulfone) random copolymers with 35 and 32 mol% disulfonation (BPS35 and 6FS32, respectively) at varying target molecular weights (20, 30, 40, 50, and 70 or 80 kg/mol) were synthesized as previously reported [14, 15]. Multiblock copolymers comprised of oligomers of 100 mol% disulfonated poly(arylene ether sulfone) and naphthalene polyimide at three different target block lengths ($BPSH100_x$-PI_y, where x and y = 5, 10, or 15 kg/mol) were synthesized as described elsewhere [16]. Multiblock copolymers comprised of oligomers of 100 mol% disulfonated poly(arylene ether sulfone) and poly(2,5-benzophenone) at two different target block lengths ($BPSH100_x$-PBP_y, where x = 6 and 10 kg/mol) were synthesized as previously reported [17]. 1-Methyl-2-Pyrrolidinone (NMP; EMD Chemicals) and N,N-Dimethyl-acetamide (DMAc; EMD Chemicals) were used as received.

2.2.2 Film casting and membrane acidification

BPS35 and 6FS32 films were first prepared by dissolving the copolymers in their potassium sulfonate salt form in DMAc (7.5% (w/v) for microscopy, 10% (w/v) for all other characterizations). Solutions were syringe filtered through 0.45 μm Teflon® filters and cast onto clean glass substrates. The transparent solutions were dried under a 120V, 250W infrared lamp for 24 h and the resultant films were dried under vacuum at 100 °C for 24 h. Films were lifted from their substrates by immersion in deionized water. All films were converted to their acid form (BPSH35, 6FSH32) by boiling in 0.5 M sulfuric acid for 2 h, rinsing in deionized (DI) water, and then boiling in DI water for 2 h, termed “Method 2” [6]. Samples were dried under vacuum at 60 °C for 12 h.

$BPSH100_x$-PI_y films were prepared identically to the random copolymer films with a few exceptions. Copolymers in their potassium sulfonate salt form were dissolved in NMP at 10% (w/v). The cast solutions were dried under the infrared lamp for 48 h and the resultant films were dried under vacuum at 120 °C for 24 h. Acidified films were equilibrated in DI water for 24 h twice.

$BPSH100_x$-PBP_y films were prepared identically to the $BPSH100_x$-PI_y films except the copolymers in their potassium sulfonate salt form were dissolved in DMAc at 5% (w/v) and the equilibrated membranes were dried under vacuum at 60 °C for 3 h.

2.2.3 Molecular weight characterization

Number average molecular weights were determined using ^{1}H-NMR [14-17], except for poly(2,5-benzophenone) oligomers for which ^{13}C-NMR was used [17].

2.2.4 Intrinsic viscosity

Intrinsic viscosity measurements were determined in NMP at 25 ºC with 0.05M LiBr using an Ubbelohde viscometer [18].

2.2.5 Proton conductivity

Conductivity measurements of acidified membranes were performed at 30 °C in water using a Solartron 1252A + 1287 impedance/gain-phase analyzer over a frequency range of 10 Hz-1 MHz. The cell geometry was chosen to ensure that the membrane resistance dominated the response of the system. The resistance of the film was taken at the frequency that produced the minimum imaginary response.

2.2.6 Water uptake

To obtain water uptake values, membranes were dried for 24 h at 100 °C, weighed, and immersed in deionized water at room temperature for 24 h. The wet membranes were blotted dry and immediately weighed again. Water uptake was calculated as the ratio of the difference between wet and dry membrane weight divided by dry membrane weight and expressed as a weight percent.

2.2.7 Atomic force microscopy (AFM)

AFM images of membrane surface morphology were obtained using a Veeco Digital Instruments MultiMode scanning probe microscope with a NanoScope IVa controller in tapping mode (TM-AFM). A silicon probe (Veeco) with an end radius of <10 nm and a force constant of 5 N/m was used to image samples at ambient conditions. Samples were equilibrated at 30%

relative humidity (RH) for at least 12 h before being imaged immediately at room temperature and approximately 15-20% RH. Imaging samples in fully hydrated conditions was done with a silicon probe with an end radius of <10 nm and a force constant of 0.9 N/m. Membranes were mounted to mica sheets with Tempfix adhesive and then equilibrated for ≥40 h in DI water prior to imaging in a fluid cell filled with DI water at room temperature.

2.2.8 Dynamic mechanical analysis (DMA)

DMA was performed using a TA Instruments 2980 Dynamic Mechanical Analyzer. Measurements were taken at 1 Hz at a constant heating rate of 5 °C/min in air from 100 to 350 °C for the random copolymers and from 100 to 400 °C for the multiblock copolymers. Random copolymers were tested in the acid form. Multiblock copolymer samples were converted to the potassium sulfonate salt form prior to testing by immersion in an excess solution (~91 wt%) of K_2SO_4 in DI water. Samples to be measured by DMA were dried under vacuum at 100 °C for 12 h and then kept sealed in a vacuum desiccator before analysis.

2.2.9 Transmission electron microscopy (TEM)

Electron density contrast within the membrane samples was enhanced by quantitatively titrating the membranes with CsOH solution to exchange the acidic protons with cesium. Membranes were embedded in epoxy and ultramicrotomed into 50-70 nm thin sections with a diamond knife. Transmission electron micrographs were obtained using a Philips EM 420 transmission electron microscope (TEM) operating at an accelerating voltage of 100 kV.

2.3 Results and Discussion

Two series of acidified films of non- and partially-fluorinated poly(arylene ether sulfone) random copolymers with varying molecular weights (BPSH35 and 6FSH32) were successfully imaged by TM-AFM (Figures 2.3 and 2.4).

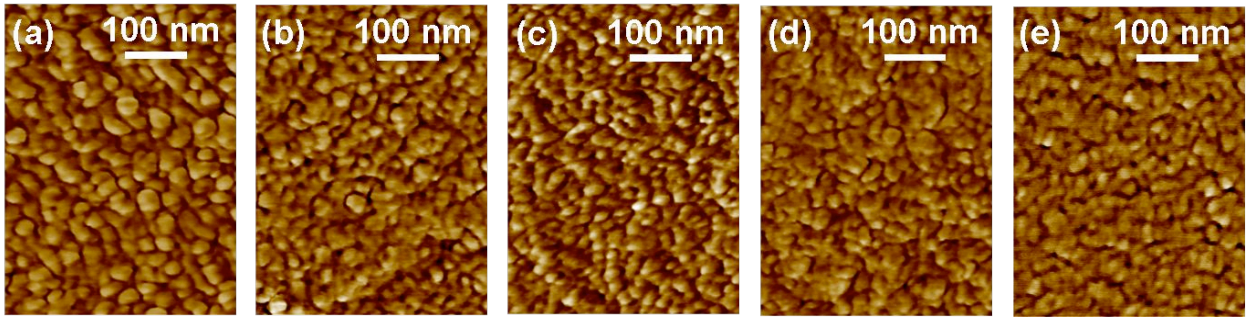

Figure 2.3. AFM phase images of BPSH35 random copolymer series: (a) 19.9 kg/mol, (b) 28.8 kg/mol, (c) 38.1 kg/mol, (d) 48.0 kg/mol, and (e) 83.1 kg/mol (extrapolated value). Setpoint ratios = 0.98, 0.98, 0.98, 0.98, 0.94.

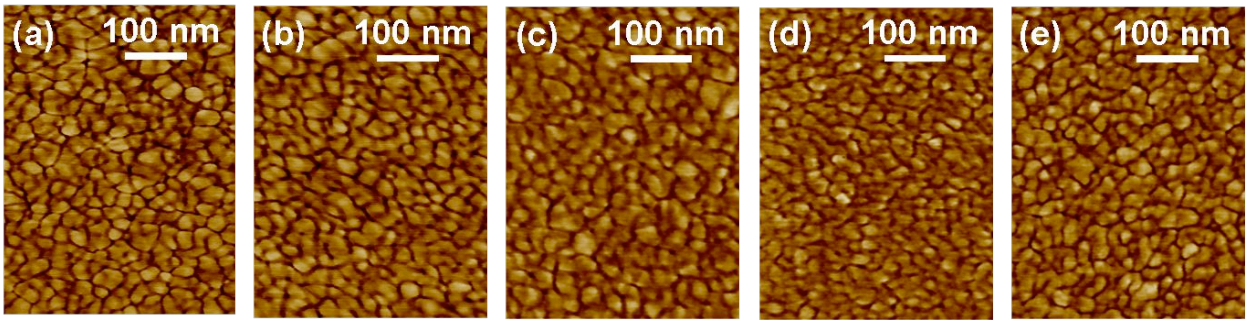

Figure 2.4. AFM phase images of 6FSH32 molecular weight series: (a) 19 kg/mol, (b) 27.5 kg/mol, (c) 37.8 kg/mol, (d) 49.5 kg/mol, and (e) ~70 kg/mol (estimated). Setpoint ratios = 0.98 (all).

It has been shown previously that adsorbed water on ion-rich regions of Nafion dampen the oscillation of an AFM cantilever, causing an observable phase shift.[19] Since the ionic domains of the membranes in this study have adsorbed water, the darker regions in the AFM images correspond to the aggregated ionic groups and the lighter regions to the hydrophobic backbones. It can be observed from the images that the differences in the phase separated morphologies of the BPSH35 films with an increase in molecular weight are small to non-existent. Also, the morphologies of the 6FSH32 films appear virtually identical as molecular weight increases. Brighter hydrophobic domain sizes appear roughly the same and the interconnectivity between darker hydrophilic domains remains consistent throughout both series. This is understandable because the ionic and non-ionic units of the random copolymers are distributed randomly throughout the films. While an increase in molecular weight would be expected to increase the number of randomly distributed ionic and non-ionic units of a random copolymer chain, it would not affect the total number of randomly distributed units in the film. Consequently, an increase in molecular weight would not influence the size of the phase separated domains formed by those units, either. Intrinsic viscosity measurements for the films (Tables 2.1 and 2.2) confirm

that molecular weight is increasing across each series. The consistency in the phase separated morphologies of the copolymers in each series is reflected in the similar values for IEC, water uptake, and proton conductivities of the copolymers (Tables 2.1 and 2.2).

Table 2.1. Membrane Properties of BPSH35 Random Copolymers[e]

M_n (kg/mol)	I.V.[b] (dL/g)	IEC[c] (meq./g)	Water Uptake (%)	Proton Conductivity (S/cm)[d]
19.9	0.43	1.49	40	0.070
28.8	0.48	1.50	43	0.080
38.1	0.63	1.52	42	0.081
48.0	0.74	1.52	38	0.080
83.1[a]	1.04	1.50	36	0.077

[a]Extrapolated M_n
[b]Determined in NMP at 25 ºC with 0.05 M LiBr
[c]Ion Exchange Capacity determined by titration
[d]Measured at 30 ºC in DI water
[e]Data taken from reference [14].

Table 2.2. Membrane Properties of 6FSH32 Random Copolymers[e]

M_n (kg/mol)	I.V.[b] (dL/g)	IEC[c] (meq./g)	Water Uptake (%)	Proton Conductivity (S/cm)[d]
19.0	0.23	1.02	27.6	NA (brittle)
27.5	0.30	1.06	26.4	0.060
37.8	0.44	1.07	27.3	0.050
49.5	0.53	1.06	27.6	0.055
70[a]	0.60	1.05	23.4	0.050

[a]Estimated M_n
[b]Determined in NMP at 25 ºC with 0.05 M LiBr
[c]Ion Exchange Capacity determined by titration
[d]Measured at 30 ºC in DI water
[e]Data taken from reference [15].

A look at the three-dimensional height images for these membranes (Figures 2.5 and 2.6) reveals that molecular weight does not appear to influence the topography of the membranes. While the topography fluctuates slightly in height from sample to sample, there is no discernable trend with molecular weight for either series indicating that random copolymer topography is independent of molecular weight.

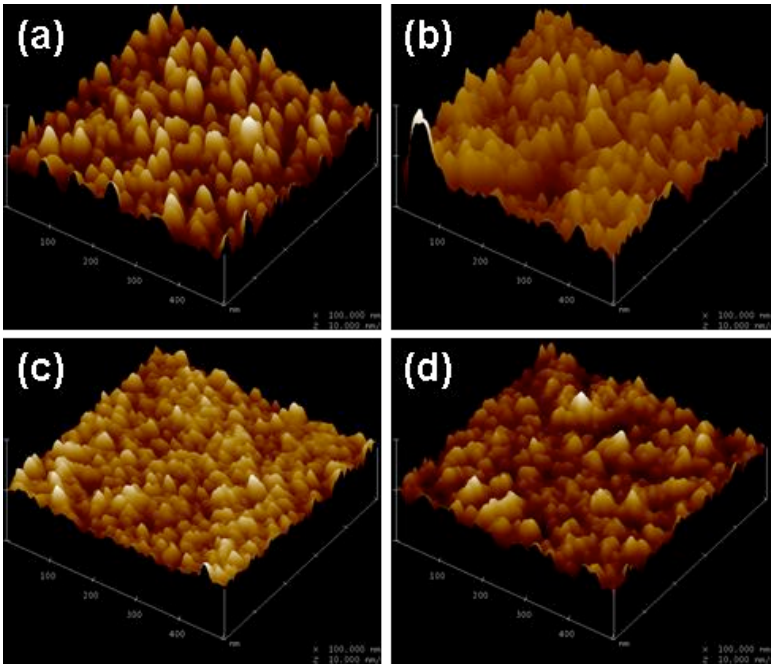

Figure 2.5. Three-dimensional tapping mode AFM height images for the BPSH35 random copolymers: (a) 19.9 kg/mol, (b) 28.8 kg/mol, (c) 38.1 kg/mol, (d) 48.0 kg/mol; Setpoint Ratios: 0.98; z range = 10 nm.

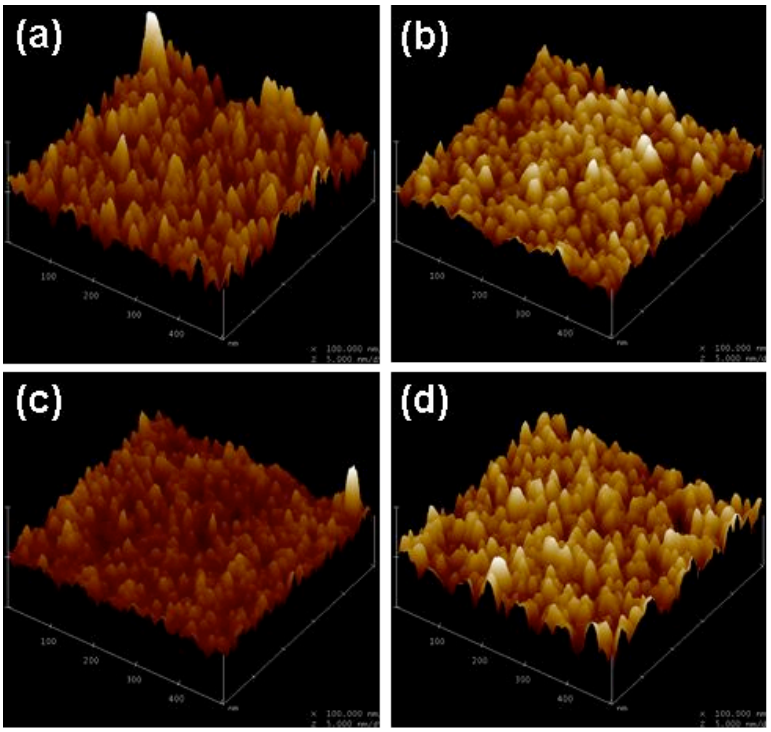

Figure 2.6. Three-dimensional tapping mode AFM height images for the 6FSH32 random copolymers: (a) 27.5 kg/mol, (b) 37.8 kg/mol, (c) 49.5 kg/mol, (d) ~70 kg/mol; Setpoint Ratios: 0.98; z range = 10 nm.

In addition to morphology and topography, the glass transition temperatures of the random copolymers do not change much with molecular weight either. The glass transition temperatures (227, 226, 229, and 233 °C) obtained from the inflection of the storage modulus curves obtained for the 6FSH32 series (Figure 2.7) indicate that for the molecular weights tested, T_g appears to be fairly independent of molecular weight. Since T_g is a function of chain mobility, which is related to free volume, it is proportional to the number of chain ends of a polymer, which decreases with molecular weight ($\overline{M}_n$). This relationship is expressed in equation 2.1 where $T_{g\infty}$ is the T_g at infinite molecular weight and K is a constant.

$$T_g \approx T_{g\infty} - \frac{K}{\overline{M}_n} \tag{2.1}$$

Each polymer has it own molecular weight above which increases in molecular weight no longer substantially affect its glass transition temperature. It is likely that the molecular weights tested for 6FSH32 are greater than this threshold molecular weight, preventing an increase in molecular weight from noticeably influencing the glass transition. It is important to note that only one glass transition was observed for each copolymer. While it has been shown previously for random ionomers that two glass transitions may be observed—a lower one for the matrix regions with isolated multiplets and a higher one for the aggregated ionic cluster regions [20-23], two glass transitions have been difficult to observe in aromatic poly(arylene ether sulfone) copolymers [7, 24, 25]. Drzewinski and MacKnight [26] reported only one glass transition temperature by DMA for sulfonated poly(arylether)sulfones, supporting the results for the 6FSH32 copolymers. The absence of a second glass transition temperature for the 6FSH32 random copolymers is probably a result of its short sequence lengths preventing a high degree of phase separation.

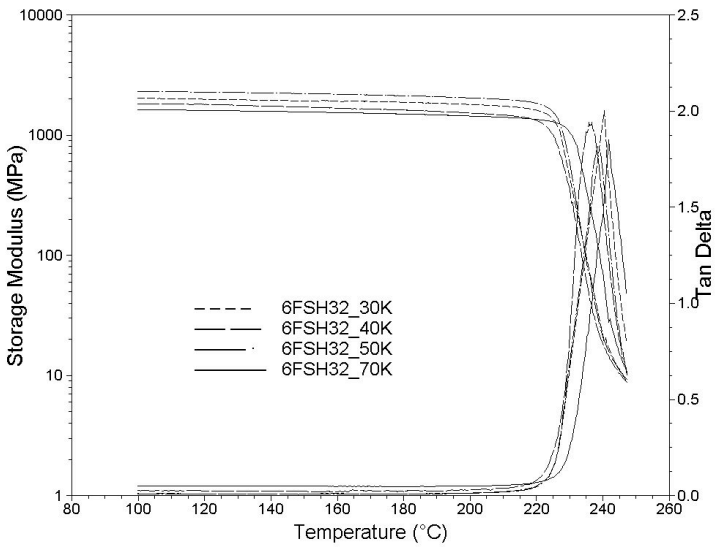

Figure 2.7. Storage modulus and tan delta curves for 6FSH32 random copolymer series.

Two multiblock copolymer series were characterized similarly to the random copolymers to evaluate the effect of block length upon the morphologies and properties of the membranes. The structures of these two series of 100 mol% disulfonated poly(arylene ether sulfone)-based multiblock copolymers with varying block lengths, $BPSH100_x$-PI_y and $BPSH100_x$-PBP_y, were presented in Figure 2.2. The morphologies of these multiblock copolymer series are decidedly different from those of the random copolymer series. Phase separation in the $BPSH100_x$-PI_y series (Figure 2.8) is very distinct compared to the random copolymer series.

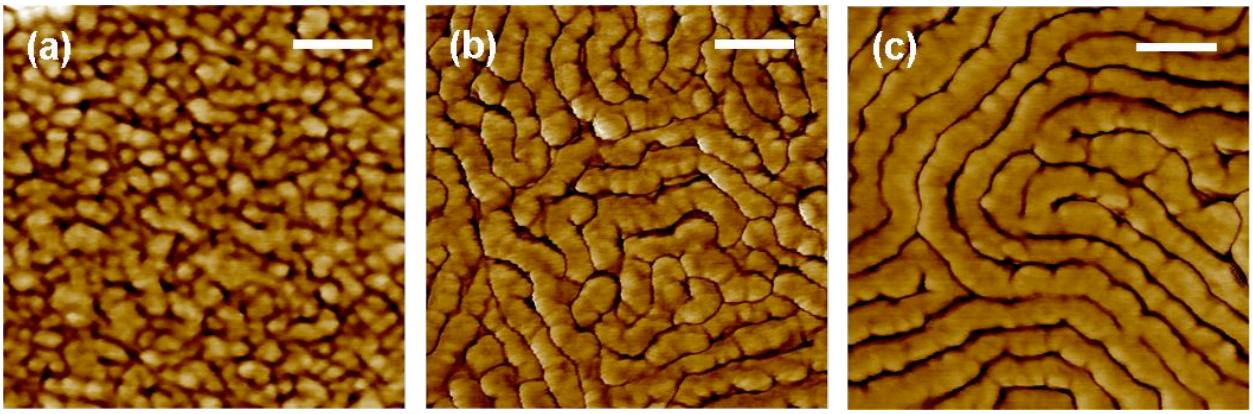

Figure 2.8. AFM phase images of BPSH100x-PIy multiblock copolymer series. (a) x = 5.5 kg/mol, y = 5.9 kg/mol, (b) x = 9.8 kg/mol, y = 10.5 kg/mol, (c) x = 14.5 kg/mol, y = 19.2 kg/mol. Setpoint ratios = 0.98, 0.90, 0.98. Scale bars = 100 nm. Images reprinted from [16]. Reprinted by permission from John Wiley & Sons, Inc.

Brighter hydrophobic domains appear to increase in connectivity as block length increases. Hydrophilic connectivity also increases across the series and is reflected in increased water uptake and proton conductivity (Table 2.3).

Table 2.3. Water Uptake and Proton Conductivities of BPSH100$_x$-PI$_y$ Multiblock Copolymers

Sample	Block Length (kg/mol)		Overall I.V. (dL/g)[a]	IEC (meq./g)[b]	Water Uptake (%)	Proton Conductivity (S/cm)[c]
	x	y				
5k-5k	5.5	5.9	0.50	1.65	59	0.080
10k-10k	9.8	10.5	0.63	1.57	67	0.085
15k-15k	14.5	19.2	0.68	1.55	85	0.100

[a]Determined in NMP at 25 ºC with 0.05 M LiBr
[b]Ion Exchange Capacity determined by titration
[c]Measured at 30 ºC in DI water

Block length also has a pronounced effect on the morphologies and membrane properties of the BPSH100$_x$-PBP$_y$ multiblock series (Figure 2.9). Phase separation is very distinct in this multiblock series compared to the random copolymer series. Brighter hydrophobic domains appear to increase in connectivity from spherical to cylindrical as block length increases.

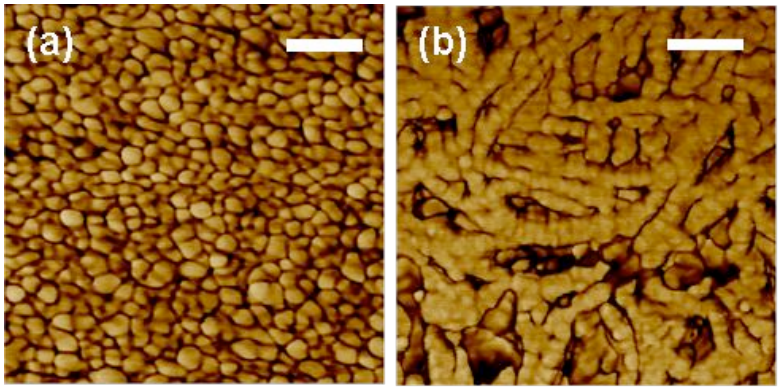

Figure 2.9. AFM phase images of BPSH100x-PBPy multiblock copolymer series; (a) x = 5.9 kg/mol, y = 5.5 kg/mol, (b) x = 9.5 kg/mol, y = 9.4 kg/mol; Setpoint ratios = 0.89 (both); Scale bars = 100 nm. Images reprinted from [17]. Reprinted by permission from John Wiley & Sons, Inc.

Intrinsic viscosity values confirm that oligomer molecular weights are increasing (Table 2.4). Although the increases in IEC and water uptake with block length may be considered to be negligibly small, there is a 50% increase in proton conductivity with increasing block length. This confirms the results for the BPSH100$_x$-PI$_y$ series that changes in multiblock copolymer block length have a considerable effect on proton conductivity through changes in phase separation.

Table 2.4. Water Uptake and Proton Conductivities of BPSH100$_x$-PBP$_y$ Multiblock Copolymers[d]

Sample	Block Length (kg/mol)		Block I.V. (dL/g)[a]		IEC (meq./g)[b]	Water Uptake (%)	Proton Conductivity (S/cm)[c]
	x	y	x	y			
6k-6k	5.9	5.5	0.24	0.32	1.65	59	0.080
10k-10k	9.5	9.4	0.35	0.48	1.57	67	0.085

[a]Determined in NMP at 25 ºC with 0.05 M LiBr
[b]Ion Exchange Capacity determined by titration
[c]Measured at 30 ºC in DI water
[d]Data taken from reference [17].

A look at the three-dimensional height images acquired simultaneously with the AFM phase images for each series of multiblock membranes (Figure 2.10) reveals that block length appears to influence membrane topography. While the topographies of the BPSH100$_x$-PI$_y$ membranes fluctuate slightly in height, the difference between the highest and lowest features of each membrane appears to increase somewhat with block length (Figure 2.10a-c). The same trend is observed with the BPSH100$_x$-PBP$_y$ multiblock series (Figure 2.10d-e). Smaller block lengths result in more uniform topographies while larger block lengths result in a more heterogeneous topography. This result may have implications for membrane electrode assembly (MEA) fabrication. Differences in topography might be expected to result in different contact between a proton exchange membrane and the electrode dispersion or decal applied to the membrane, ultimately affecting the performance of the fuel cell.

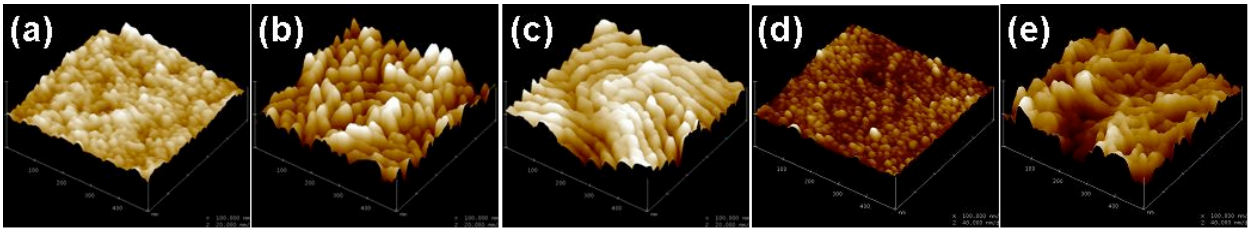

Figure 2.10. Three-dimensional tapping mode AFM height images for the BPSH100x-PIy multiblock copolymers: (a) x = 5.5 kg/mol, y = 5.9 kg/mol, (b) x = 9.8 kg/mol, y = 10.5 kg/mol, (c) x = 14.5 kg/mol, y = 19.2 kg/mol. Setpoint ratios = 0.98, 0.90, 0.98; z range = 20 nm; and the BPSH100$_x$-PBP$_y$ multiblock copolymers: (d) x = 5.9 kg/mol, y = 5.5 kg/mol, (e) x = 9.9 kg/mol, y = 9.4 kg/mol. Setpoint ratios = 0.89 (both); z range = 40 nm.

Although the surface morphology of these multiblock copolymer membranes appears to change with block length, the more important question with respect to PEM performance is what effect block length has on the bulk of these membranes and their resulting ability to conduct protons. To determine this, the membranes were imaged by TEM (Figure 2.11). Generally speaking, the bulk morphologies of these membranes appear to correlate with their surface

morphologies. In the BPSH100$_x$-PI$_y$ series (Figure 2.11a-c), phase separated domains of increasing size appear in the TEM images, however they appear to be smaller than the domains observed on the surface (Figure 2.8). The domains in the BPSH100-PBP micrograph (Figure 2.11d) also look smaller than those in the corresponding AFM micrograph (Figure 2.9a). This difference is attributed in part to the differences in moisture content during AFM and TEM imaging. The high vacuum in the TEM column is likely responsible for drawing moisture from the thin sample sections, thereby shrinking the domain sizes within the membrane. Another reason for the difference in domain sizes between the surface and the bulk of the membranes is that the TEM sections are cut perpendicular to the plane of the membrane surface. Anisotropic domains would consequently look different in each direction.

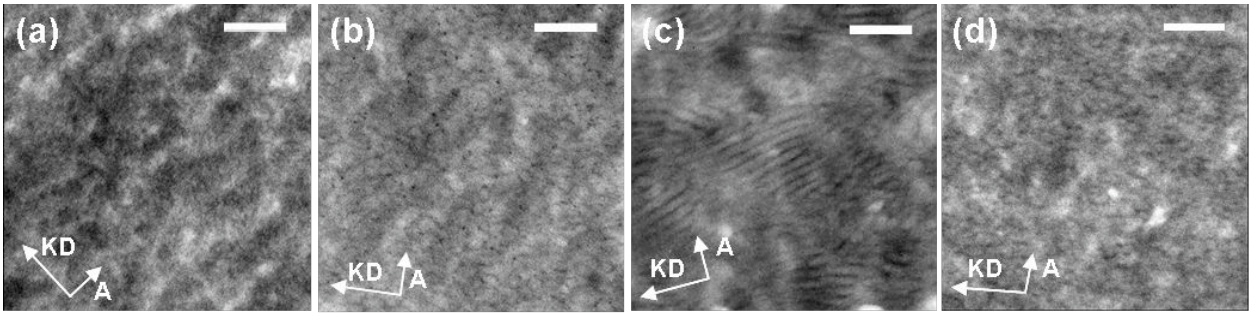

Figure 2.11. TEM micrographs of multiblock copolymers: (a) BPSH100-PI 5k-5k, (b)BPSH100-PI 10k-10k, (c) BPSH100-PI 15k-15k, and (d) BPSH100-PBP 6k-6k. "A" denotes direction of air side. "KD" denotes the knife direction during microtoming. Scale bars = 100 nm.

The BPSH100$_x$-PI$_y$ series was subjected to a DMA single frequency temperature sweep in an attempt to ascertain the effect of block length upon glass transition temperature. The BPSH100$_x$-PBP$_y$ membranes were not tested because they were too brittle. The BPSH100$_x$-PI$_y$ membranes were first converted from the acid form (BPSH) into their potassium salt form (BPS) prior to testing. This was done because the sulfonic acid groups of highly sulfonated BPSH have been shown to degrade at temperatures as low as 230 °C [27], which is well below the expected glass transition temperature of the polyimide blocks of around 320 °C (based on unpublished DSC data). The samples were then tested without recasting so that their original acid form morphology would be retained as much as possible. An unfortunate side effect of the neutralization by K_2SO_4 was embrittlement of the membranes, which may reflect partial base-catalyzed cleavage of the imide ring. As a result, the membrane with the lowest block length, the "5k-5k" sample, was too brittle to withstand the oscillations of the instrument. The membrane with the next longest block length, the "10k-10k" sample, fractured before the full temperature

sweep was completed. Only the sample with the largest block length, the "15k-15k" sample, was robust enough to withstand the full temperature sweep to 400 °C (Figure 2.12). While no quantitative measurements of strength were made, these differences in brittleness between the $BPS100_x$-PI_y samples implicitly suggest that mechanical strength increases with block length.

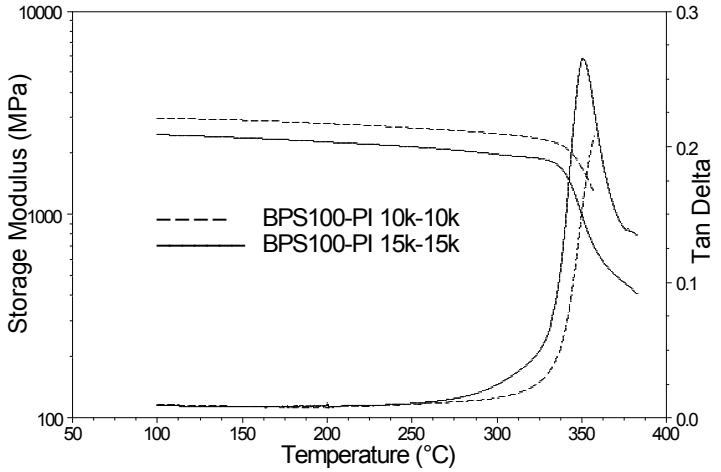

Figure 2.12. Storage modulus and tan delta curves for BPSH100x-PIy multiblock copolymer series

Glass transition temperatures of 352 and 346 °C were obtained from the inflections of the storage modulus curves in Figure 2.12 for the 10k-10k and 15k-15k samples, respectively. Although it is difficult to deduce a conclusive trend from two points, these data suggest that the T_g of these multiblock copolymers does not increase with block length in this range. This behavior is similar to that of the 6FSH32 random copolymer series. It is likely that the overall molecular weights of the multiblock copolymer chains, like the molecular weights of the 6FSH32 series, exceed the molecular weight above which increases in molecular weight no longer substantially affect T_g. This conclusion is tenable considering that the intrinsic viscosities of the two multiblock copolymers in Figure 12 exceed those of the copolymers in the 6FSH32 series.

Although non-ionic block copolymers often exhibit a separate glass transition for each of their component blocks [28], only one glass transition appears in the tan delta curve of the 15k-15k sample. This transition is attributed to the polyimide blocks, whose glass transition temperature is expected to be around 320 °C. No glass transition corresponding to the BPS100 block can be observed in the storage modulus or tan delta curves. If it were present, the T_g of BPS100 would be expected to be higher than 283 °C, the T_g reported for BPS60 [7], because T_g rises with ionic content [20]. Two glass transitions have been observed via DSC for the

BPSH100-PBP 6k-6k multiblock copolymer [17]. Given that the block lengths of the BPSH100-PI 15k-15k multiblock copolymer are over twice as large as those of the BPSH100-PBP 6k-6k multiblock copolymer, and that DMA is more sensitive to transitions than DSC, it does not make sense why only one transition is observed for the BPSH100-PI. Further research is required to understand the seeming absence of the second glass transition.

Given that hydrolytic stability is an important characteristic of a successful proton exchange membrane [3], TM-AFM was performed in liquid water to gauge the influence of block length on the morphological stability of fully hydrated membranes. The 6FSH32 membrane with a molecular weight of approximately 70 kg/mol was chosen as the first sample because its random structure is effectively equal to a negligibly small block length close to zero. In addition, it has a partially fluorinated structure and the highest molecular weight of its series, making it the one random copolymer with any chance (albeit small) of being more hydrolytically stable than the others in this study. The $BPSH100_x$-PI_y multiblock copolymers were also tested. The resulting micrographs (Figure 2.13) indicate that block length increases hydrolytic stability.

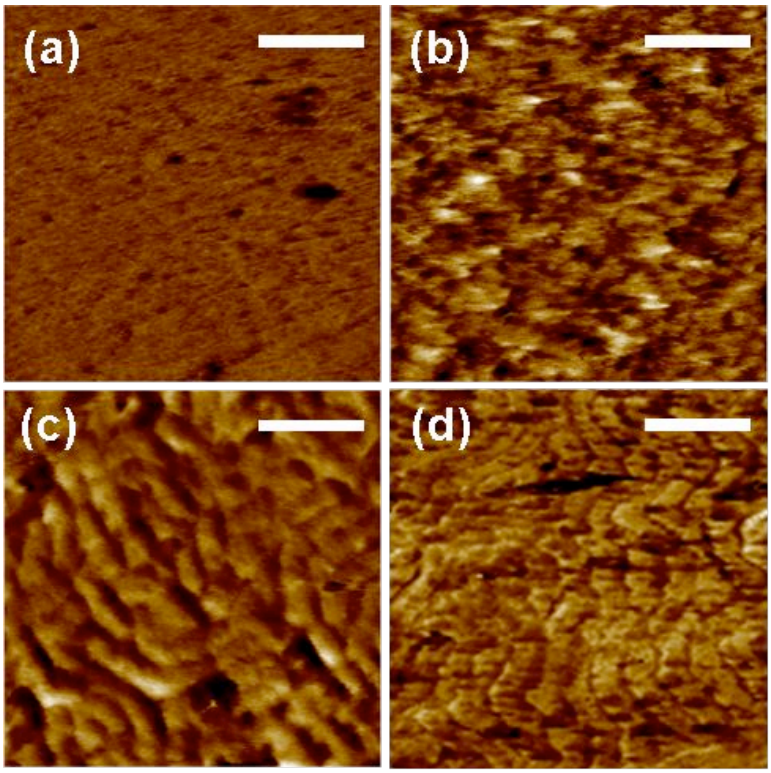

Figure 2.13. AFM phase images of fully hydrated membranes: (a) 6FSH32 ~70 kg/mol, and BPSH100-PI series (b) 5k-5k, (c) 10k-10k, and (d) 15k-15k. Setpoint ratios = 0.38, 0.52, 0.54, 0.46. Scale bar = 100 nm.

When fully hydrated, the randomly distributed hydrophilic domains of the 6FSH32 membrane swell so much that phase separation is lost and the surface morphology of the membrane becomes very homogenous (Figure 2.13a). This result matches an earlier observation made by Kim et al. [29] for BPSH40 membranes, in which high ion content induced swelling produced featureless morphology. Whether this effect occurs only on the surface or in the bulk as well is not clear from these data. The multiblock copolymers, in contrast, appear to retain their phase separated morphology to a greater degree as block length increases (Figure 2.13b-d). This occurs despite an increase of 60 mol% disulfonation in the hydrophilic blocks of BPSH100 compared to the BPSH40 imaged by Kim et al. [29] These data show that the phase separated morphology of the multiblock copolymers, which increases with block length, enhances the membranes' ability to resist swelling when hydrated.

2.4 Conclusions

From the data above, it can be concluded that changes in molecular weight above a minimum value have little effect on the morphologies, water uptake, proton conductivities, and glass transition temperatures of random copolymers. Changes in block length do, however, have a pronounced effect on multiblock copolymers, affecting surface and bulk morphologies as well as water uptake, proton conductivity, and hydrolytic stability. Data suggest that multiblock copolymer glass transition temperature is independent of block length, but more study is required before a definitive conclusion can be made, especially regarding the absence of a second glass transition. Interestingly, the multiblock membrane properties affected by block length appear to improve as the degree of nanophase separation increases, suggesting that PEM properties may be optimized by changes in morphology. The authors thus recommend that future research into multiblock copolymers as PEMs should also include alternative methods of casting multiblock films to manipulate their morphologies.

2.5 Acknowledgements

The authors wish to thank the National Science Foundation "Partnership for Innovation" Program (HER-0090556) and IGERT Program (DGE-0114346), the Department of Energy (DE-FG36-06G016038), and the Nissan Motor Company for supporting this research.

2.6 References

1. Winter, M. and R.J. Brodd, *What are batteries, fuel cells, and supercapacitors?* Chem. Rev., 2004. **104**(10): 4245-4269.

2. Perry, M.L. and T.F. Fuller, *A historical perspective of fuel cell technology in the 20th century.* J Electrochem. Soc., 2002. **149**(7): S59-S67.

3. Hickner, M.A., H. Ghassemi, Y.S. Kim, B.R. Einsla, and J.E. McGrath, *Alternative polymer systems for proton exchange membranes (PEMs).* Chem. Rev., 2004. **104**(10): 4587-4611.

4. Mauritz, K.A. and R.B. Moore, *State of understanding of Nafion.* Chemical Reviews, 2004. **104**(10): 4535-4585.

5. Savadogo, O., *Emerging membranes for electrochemical systems: (i) solid polymer electrolyte membranes for fuel cell systems.* J. New Mater. Elect. Sys., 1998. **1**(1): 47-66.

6. Kim, Y.S., F. Wang, M. Hickner, S. McCartney, Y.T. Hong, W. Harrison, T.A. Zawodzinski, and J.E. McGrath, *Effect of acidification treatment and morphological stability of sulfonated poly(arylene ether sulfone) copolymer proton-exchange membranes for fuel-cell use above 100 degrees C.* J. Polym. Sci.: Part B: Phys, 2003. **41**(22): 2816-2828.

7. Wang, F., M. Hickner, Y.S. Kim, T.A. Zawodzinski, and J.E. McGrath, *Direct polymerization of sulfonated poly(arylene ether sulfone) random (statistical) copolymers: Candidates for new proton exchange membranes.* J. Memb. Sci., 2002. **197**(1-2): 231-242.

8. McGrath, J.E., *Progress in alternate proton exchange membrane materials for fuel cells.* Abstracts of Papers, 234th ACS National Meeting, Boston, MA, United States, August 19-23, 2007, 2007: POLY-068.

9. Wang, H., A.S. Badami, A. Roy, and J.E. McGrath, *Synthesis of poly(arylene ether sulfone)-poly(benzophenone) multiblock copolymers for proton exchange membrane.* PMSE Preprints, 2006. **95**: 202-203.

10. Yu, X., A. Roy, and J.E. McGrath, *Perfluorinated-sulfonated hydrophobic-hydrophilic multiblock copolymers for proton exchange membranes (PEMs).* PMSE Preprints, 2006. **95**: 141-142.

11. Li, Y., A. Roy, A.S. Badami, M. Hill, J. Yang, S. Dunn, and J.E. McGrath, *Synthesis and characterization of partially fluorinated hydrophobic–hydrophilic multiblock copolymers containing sulfonate groups for proton exchange membranes.* J. Power Sources, 2007. **172**(1): 30-38.

12. Roy, A., M.A. Hickner, H.-S. Lee, A. Badami, X. Yu, Y. Li, T. Glass, and J.E. McGrath, *Transport properties of proton exchange membranes.* ECS Transactions, 2007. **2**(24, Direct Methanol Fuel Cells): 45-54.

13. Roy, A., X.A. Yu, A. Badami, and J.E. McGrath, *Multiblock hydrophilic-hydrophobic proton exchange membranes for fuel cells.* Abstracts of Papers of the American Chemical Society, 2006. **231**.

14. Li, Y.X., F. Wang, J. Yang, D. Liu, A. Roy, S. Case, J. Lesko, and J.E. McGrath, *Synthesis and characterization of controlled molecular weight disulfonated poly(arylene ether sulfone) copolymers and their applications to proton exchange membranes.* Polymer, 2006. **47**(11): 4210-4217.

15. Li, Y., J. Yang, A. Roy, B. Einsla, and F. Wang, Prepr. Pap--Am. Chem. Soc., Div. Fuel Chem., 2005. **50**(2): 573.

16. Lee, H.-S., A. Roy, A.S. Badami, and J.E. McGrath, *Segmented sulfonated poly(arylene ether sulfone)-b-polyimide copolymers for proton exchange membrane fuel cells. I. Copolymer synthesis and fundamental properties.* J. Polym. Sci. Part A: Polym. Chem., 2007. **45**: 4879-4890.

17. Wang, H., A.S. Badami, A. Roy, and J.E. McGrath, *Multiblock copolymers of poly(2,5-benzophenone) and disulfonated poly(arylene ether sulfone) for proton-exchange membranes. I. Synthesis and characterization.* J. Polym. Sci.: Part A: Polym. Chem., 2007. **45**(2): 284-294.

18. Yang, J., Y. Li, X. Yu, H. Wang, K.B. Wiles, M. Hill, H.-S. Lee, and J.E. McGrath, *Viscometric behavior and molecular weight characterization of sulfonated poly(arylene ether sulfone) copolymers.* Abstracts of Papers of the American Chemical Society, 2005. **230**: U1689-U1689.

19. James, P.J., M. Antognozzi, J. Tamayo, T.J. McMaster, J.M. Newton, and M.J. Miles, *Interpretation of contrast in tapping mode AFM and shear force microscopy. A study of Nafion.* Langmuir, 2001. **17**(2): 349-360.

20. Eisenberg, A., M. King, and M. Navratil, *Secondary relaxation behavior in ion-containing polymers.* Macromolecules, 1973. **6**(5): 734-737.

21. Hara, M., P. Jar, and J.A. Sauer, *Dynamic mechanical-properties of sulfonated polystyrene ionomers.* Polymer, 1991. **32**(9): 1622-1626.

22. Weiss, R.A., J.J. Fitzgerald, and D. Kim, *Viscoelastic behavior of lightly sulfonated polystyrene ionomers.* Macromolecules, 1991. **24**(5): 1071-1076.

23. Hird, B. and A. Eisenberg, *Sizes and stabilities of multiplets and clusters in carboxylated and sulfonated styrene ionomers.* Macromolecules, 1992. **25**(24): 6466-6474.

24. Johnson, R.N., A.G. Farnham, R.A. Clendinning, W.F. Hale, and C.N. Merriam, *Poly(aryl ethers) by nucleophilic aromatic substitution. I. Synthesis and properties.* J. Polym. Sci.: Polym. Chem., 1967. **5**: 2375.

25. Johnson, B.C., I. Yilgor, C. Tran, M. Iqbal, J.P. Wightman, D.R. Lloyd, and J.E. McGrath, *Synthesis and characterization of sulfonated poly(arylene ether sulfones).* J. Polym. Sci.: Part A: Polym. Chem., 1984. **22**(3): 721-737.

26. Drzewinski, M. and W.J. MacKnight, *Structure and properties of sulfonated polysulfone ionomers.* J. Appl. Polym. Sci., 1985. **30**(12): 4753-4770.

27. Harrison, W.L., F. Wang, J.B. Mecham, V.A. Bhanu, M. Hill, Y.S. Kim, and J.E. McGrath, *Influence of the bisphenol structure on the direct synthesis of sulfonated poly(arylene ether) copolymers. I.* J. Polym. Sci.: Part A: Polym. Chem., 2003. **41**(14): 2264-2276.

28. Noshay, A. and J.E. McGrath, *Block copolymers: Overview and critical survey*. 1977, New York: Academic Press. 516.

29. Kim, Y.S., L. Dong, M.A. Hickner, B.S. Pivovar, and J.E. McGrath, *Processing induced morphological development in hydrated sulfonated poly(arylene ether sulfone) copolymer membranes.* Polymer, 2003. **44**(19): 5729-5736.

Chapter 3. Morphological Investigations of Disulfonated Poly(arylene ether sulfone)-*b*-Naphthalene Dianhydride-Based Polyimide Multiblock Copolymers as Potential High Temperature Proton Exchange Membranes

Anand S. Badami,[1] Abhishek Roy,[1] Hae-Seung Lee,[1] Yanxiang Li,[1,2] and James E. McGrath[1]

[1]*Department of Chemistry, Macromolecular Science and Engineering Program, Macromolecules and Interfaces Institute, Virginia Polytechnic Institute and State University, Blacksburg, VA 24061, USA*

[2]*Present Address: The Dow Chemical Company, 1710 Building, Midland, MI 48674*

Abstract

A major goal of the current research effort into proton exchange membrane fuel cells (PEMFCs) has been focused on developing high temperature membranes that can operate at ~120 °C and low humidities. The benefits of operation at these temperatures include an increased driving force for heat rejection, greater tolerance to impurities in the fuel stream, improved electrode kinetics yielding enhanced performance, and improved water management and gas transport. Nafion®, the current state-of-the-art membrane, lacks the ability to retain enough water to maintain its proton conductivity over an extended time at 120 °C, prompting the need to develop alternative high temperature membranes. Multiblock copolymers synthesized from hydrophilic 100% disulfonated poly(arylene ether sulfone) (BPSH100) and hydrophobic naphthalene dianhydride-based polyimide (PI) oligomers may be an alternative. The high temperature behavior of BPSH100-PI multiblock copolymers was evaluated in terms of morphology and water retention and compared to that of BPSH-based random copolymers, Nafion 112, and new recast Nafion (NRE211). Atomic force microscopy (AFM) imaging performed at elevated temperatures with a hot stage demonstrated that the multiblock copolymer with block lengths of ~15 kg/mol displayed no morphological changes up to 120 °C or even higher. Changes observed in the micrographs with increasing temperature were attributed to water desorption, which was less for the phase separated multiblock copolymers than the random copolymers and Nafion. Thermogravimetric analyses confirmed that the observed changes were indeed the result of a continuous loss of water from the bulk of the membranes with increasing

temperature. Water desorption was observed to decrease with an increase in block length. The multiblock copolymers exhibited little to no loss of water during an isotherm at 200 °C, unlike the random copolymers and Nafion which continued to lose water. From this study, it appears a BPSH100-PI multiblock copolymer with large block length has some morphological stability and retains water (likely strongly bound) at temperatures exceeding 120 °C, suggesting its candidacy as a high temperature PEM.

3.1 Introduction

Much research has recently been focused on improving membranes for proton exchange membrane fuel cells (PEMFCs), as described in several recent reviews [1-5]. A great deal of the motivation behind PEMFC research is the goal of replacing the internal combustion engine in automobiles with this highly efficient energy conversion device. The U.S. Department of Energy has established an operating target of 120 °C at 25% relative humidity for automotive PEMFCs by 2010 to surmount the factors that prevent widespread commercialization of PEMFCs at their current operating temperature of 80 °C [6]. The benefits of operating at 120 °C include: (1) an increased driving force for improved heat rejection enabling 50% smaller radiators and conventional coolants to be used, (2) greater tolerance of electrodes to impurities like carbon monoxide in the hydrogen feed, (3) improved electrode reaction kinetics translating into enhanced performance, and (4) improved water management and gas transport because of less liquid water in the system [6-9].

Unfortunately, the current state-of-the-art proton exchange membranes (PEMs) do not perform well at 120 °C. The current PEM standard for commercial use is Nafion®, a poly(perfluorosulfonic acid) random copolymer manufactured by the E. I. DuPont Company [3, 10]. Nafion possesses several desirable characteristics for PEM use at low temperatures, including oxidative stability, good proton conductivity, and mechanical strength. However, it displays poor proton conductivity at low hydration levels and above 80°C as it loses water, and low mechanical strength at higher temperatures (e.g. 120 °C). These limitations have prompted efforts to develop alternative membranes for high temperature operation [11, 12]. To be successful at this temperature, membranes must be both thermally stable and retain sufficient water to maintain proton conductivity.

It is hypothesized that a multiblock copolymer synthesized from 100% disulfonated poly(arylene ether sulfone) (BPSH100) and naphthalene dianhydride-based six-membered ring polyimide (PI) oligomers [13] (Figure 3.1) may be an alternative. BPSH-based random copolymers have been demonstrated to be protonically conductive at elevated temperatures [14]. Naphthalene dianhydride-based polyimide oligomers are anticipated to provide the multiblock copolymer with dimensional stability and enhance thermal stability [15]. The six-membered ring structure of a naphthalenic dianydride-based polyimide is preferable to the five-membered ring structure of a phthalic polyimide because the former is much more resistant to hydrolysis [15] . In addition to minimizing hydrolysis, the phase separation of the multiblock structure may enhance water retention over BPSH-based random copolymers. The phase separated morphology of BPSH100-PI multiblock copolymers has already been shown to facilitate water transport [16], limit swelling of ionic domains at fully hydrated conditions [17], and display competitive conductivities to Nafion at 80 °C over a range of relative humidities [13]. The current study examines the higher temperature behavior of BPSH100-PI multiblock copolymers in terms of morphology and water retention compared to BPSH-based random copolymers and Nafion.

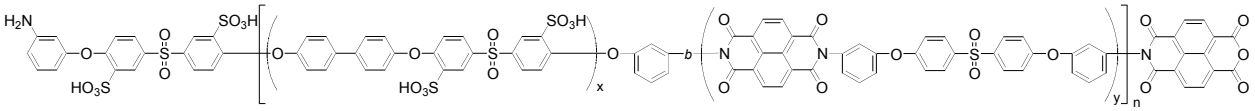

Figure 3.1. Idealized structure of BPSH100-PI multiblock copolymer

3.2 Experimental

3.2.1 Materials

Disulfonated poly(arylene ether sulfone) random copolymers with 35 mol% disulfonation (BPS35) at varying target molecular weights (20, 30, and 50 kg/mol) were synthesized as previously reported [18]. Multiblock copolymers comprised of oligomers of 100 mol% disulfonated poly(arylene ether sulfone) and naphthalene polyimide at three different target block lengths ($BPSH100_x$-PI_y, where x and y = 5, 10, or 15 kg/mol) were synthesized as described elsewhere [13]. 1-Methyl-2-Pyrrolidinone (NMP; EMD Chemicals), N,N-Dimethyl-acetamide (DMAc; EMD Chemicals), HPLC water (Fisher), and Nafion 112 (Dupont) in its acid

form were used as received. Nafion 211 (Dupont) was separated from its backing layers by immersion in DI water, pretreated for 3 h in 1 M HCl at 80 °C followed by 3 h in DI water at 80 °C and 12 h in fresh DI water at 25 °C. Double/Bubble® Epoxy (Elementis Specialties) was used as received.

3.2.2 Membrane preparation

BPS35 films were first prepared by dissolving the copolymers in their potassium sulfonate salt form in DMAc at 7.5% (w/v). Solutions were syringe filtered through 0.45 μm Teflon® filters and cast onto clean glass substrates. The transparent solutions were dried under a 120V, 250W infrared lamp for 24 h and the resultant films were dried under vacuum at 100 °C for 24 h. Films were lifted from their substrates by immersion in deionized water. All films were converted to their acid form (BPSH35) by boiling in 0.5 M sulfuric acid for 2 h, rinsing in deionized (DI) water, and then boiling in DI water for 2 h, termed "Method 2" [14]. Samples were dried under vacuum at 60 °C for 12 h.

$BPSH100_x$-PI_y films were prepared identically to the random copolymer films with a few exceptions. Copolymers in their potassium sulfonate salt form were dissolved in NMP at 10% (w/v). The cast solutions were dried under the infrared lamp for 48 h and the resultant films were dried under vacuum at 120 °C for 24 h. Acidified films were equilibrated in DI water for 24 h twice.

3.2.3 Atomic force microscopy (AFM)

Tapping mode AFM was performed using a Digital Instruments MultiMode atomic force microscope with a NanoScope IVa controller. Samples were mounted to stainless steel pucks with epoxy and cured overnight at 100 °C. Samples were equilibrated at 50% relative humidity (RH) for at least 12 h before imaging. A silicon probe (Veeco) with an end radius of <10 nm and a force constant of 5 N/m was used to image samples at temperatures ranging from ambient to 180 °C. A Digital Instruments thermal applications controller was used to control the temperature of both the sample stage and probe. The stage and probe temperatures were held constant for 30 min prior to imaging to ensure that each sample was at the desired temperature during imaging.

3.2.4 Thermogravimetric analysis (TGA)

Thermogravimetric analyses were performed on a TA Instruments TGA Q-500. Membrane samples analyzed by thermogravimetric analysis were initially placed in a desiccator at 30% RH for at least 48 h. During analysis, the samples were heated in air at 2.5 °C/min from ambient temperature to 200 °C. Immediately following this heated drying run, the samples were held at 200 °C for 1 h.

3.2.5 Differential scanning calorimetry (DSC)

Water depressed glass transition temperature (T_g) experiments were conducted with a TA Instruments DSC Q-1000. The samples were placed in thermally sealed TA Instruments high volume DSC pans capable of withstanding pressure up to about 600 psi. Samples were cooled to -70 °C and then heated at a rate of 5 °C/min under a nitrogen atmosphere.

3.2.6 Fourier transform infrared (FTIR) spectroscopy

FTIR spectroscopy measurements on a thin, homogeneous cast film were recorded using a Bruker Tensor 27 FTIR spectrometer with OPUS software version 5.0. The membrane was initially placed in a desiccator at 30% RH for at least 48 h. A heating cell was used to heat the film in-situ during imaging at 20 °C intervals from 80 °C to 120 °C. The membrane was allowed to equilibrate at each temperature for 30 min before measurements were taken.

3.3 Results and Discussion

3.3.1 Hot stage AFM imaging

Hot stage AFM imaging at elevated temperatures was performed on two BPSH100-PI multiblock copolymers with different block lengths (approximately 5 kg/mol (5k-5k) and 15 kg/mol (15k-15k)) to verify the morphological stability of the copolymers at elevated temperatures and evaluate the influence of block length on their thermal stability. The resulting images for the 5k-5k copolymer (Figure 3.2) indicate that both its topography and its phase separated morphology observed at room temperature appear to remain more or less consistent until 100 °C. At 100 °C and above, the sharpness of the phase separation decreased. At 150 °C the topography appears blurred and the phase separation appears to disappear. Whether this is

related to an order-disorder transition is not known. The images for the copolymer with the larger block lengths of 15 kg/mol (Figure 3.3) show that its topography and phase separated morphology observed at room temperature remain consistent until at least 145 °C with some slight distortion observed at 155 °C. In contrast to the 5k-5k membrane, the topography and phase separation of this 15k-15k membrane do not start to blur and disappear respectively until around 160 °C. This is a difference of at least 10 °C, possibly attributable to the difference in block length of the membranes. By 180 °C, no phase separation or differences in topography are discernable in the 15k-15k membrane.

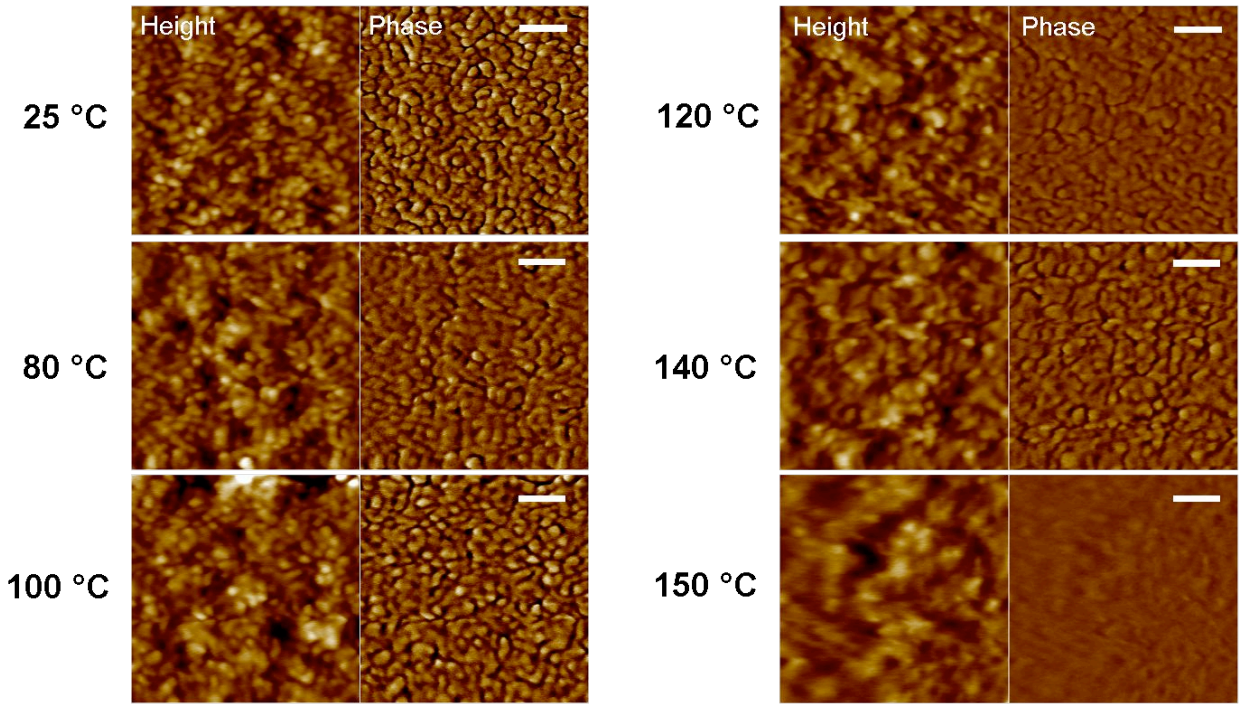

Figure 3.2. Hot stage AFM micrographs of BPSH100-PI with block lengths of ~5 kg/mol. Setpoint Ratios: 0.91, 0.82, 0.79, 0.87, 0.84, 0.69; Height images: z = 10 nm; Phase images: z = 25°. Scale bars = 100 nm.

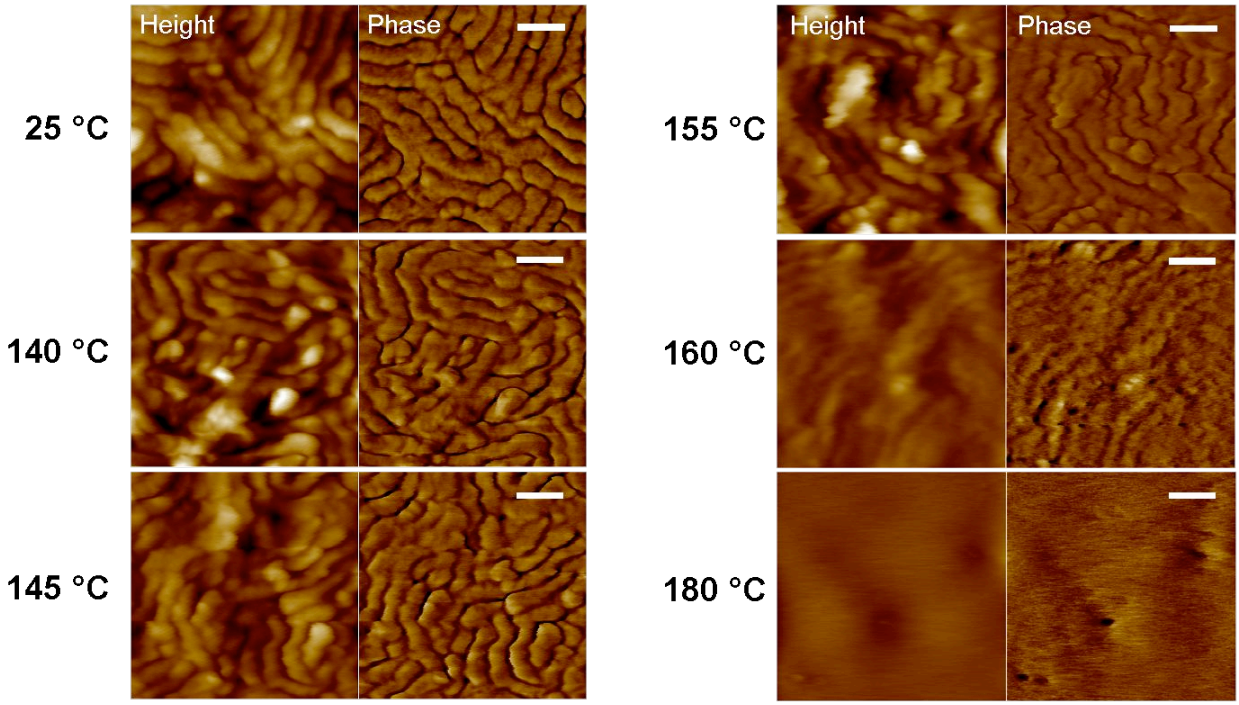

Figure 3.3. Hot stage AFM micrographs of BPSH100-PI with block lengths of ~15 kg/mol. Setpoint Ratios: 0.86, 0.81, 0.86, 0.87, 0.84, 0.73; Height images: z = 25 nm; Phase images: z = 40°. Scale bars = 100 nm.

AFM imaging at elevated temperatures was also performed on BPSH35 random copolymers and Nafion 112 in order to compare their elevated temperature behavior to that of the BPSH100-PI copolymers. Figure 3.4 shows the images obtained for BPSH35 with a molecular weight of 19.9 kg/mol (BPSH35-20k).

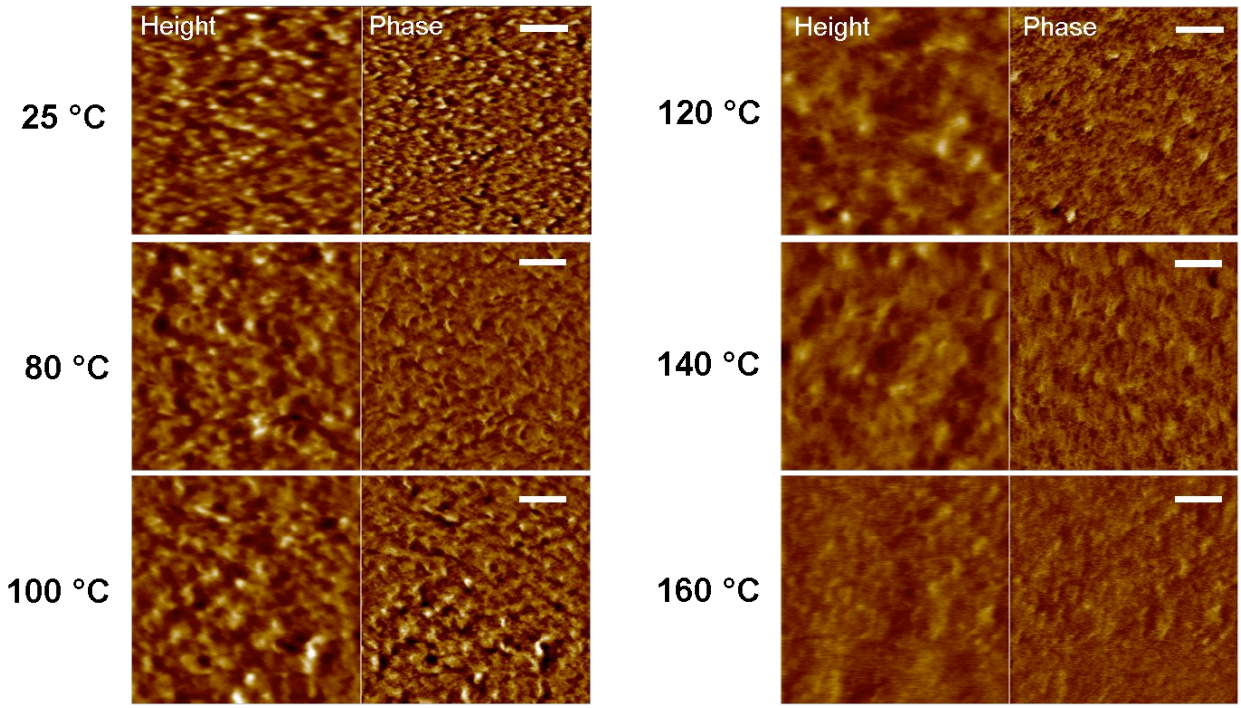

Figure 3.4. Hot stage AFM micrographs of BPSH35 with molecular weight of 19.9 kg/mol (BPSH35-20k). Setpoint Ratios: 0.72, 0.76, 0.63, 0.33, 0.58, 0.56; Height images: z = 10 nm; Phase images: z = 30°. Scale bars = 100 nm.

The topography and phase separation of this membrane begin changing at 80 °C. As temperature increases, the topography appears to become more homogenous and the phase separation appears to decrease. The molecular weight of this random copolymer was not thought to influence its thermal stability or water retention because its ionic domains are randomly distributed throughout the membrane. An increase in total molecular weight might only be expected to increase the number of ionic domains, but not their size, tendency to aggregate, ability to hydrogen bond water, etc. This thought was verified by imaging BPSH35 with a weight of 48.0 kg/mol (BPSH35-50k; Figure 3.5). The behavior of this membrane at elevated temperature appears nearly identical to that of BPSH35-20k, supporting the idea that molecular weight does not impart any advantage in terms of elevated temperature stability to random copolymers.

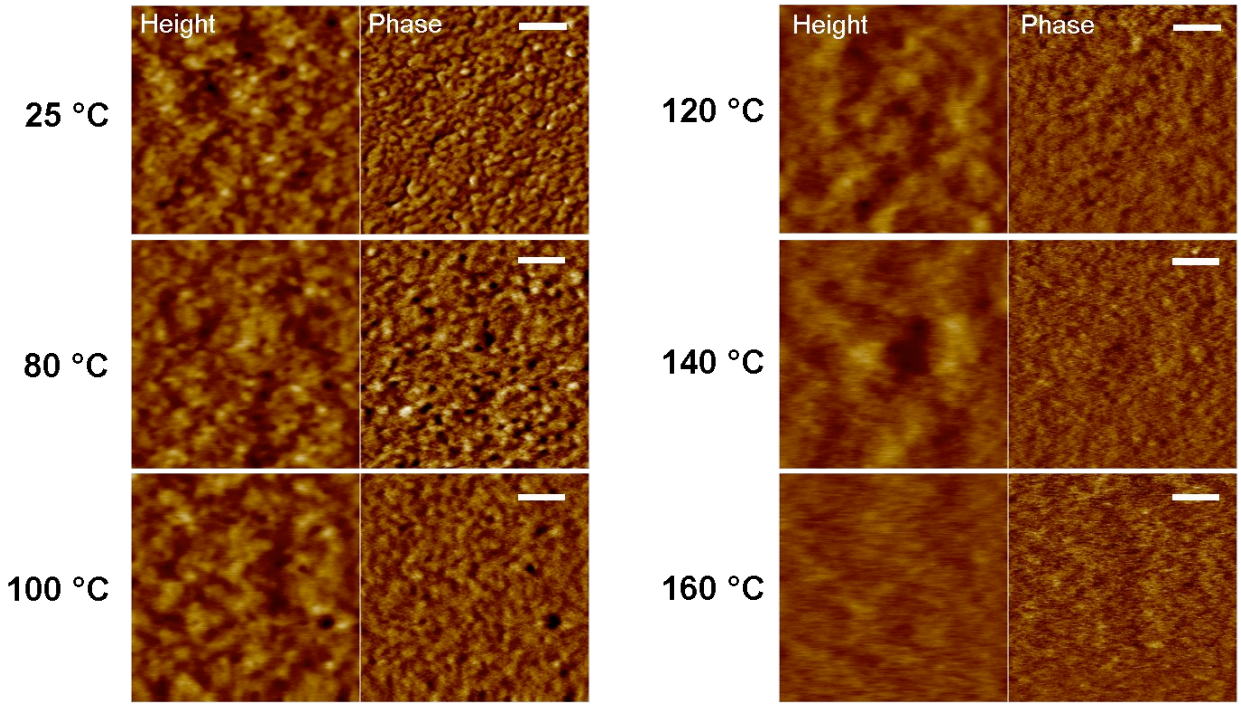

Figure 3.5. Hot stage AFM micrographs of BPSH35 with molecular weight of 48.0 kg/mol (BPSH35-50k). Setpoint Ratios: 0.94, 0.76, 0.83, 0.78, 0.82, 0.76; Height images: z = 6 nm; Phase images: z = 8° (25 °C), 15° (rest). Scale bars = 100 nm.

Nafion 112 displays even poorer elevated temperature stability than BPSH35 (Figure 3.6). At 80 °C, it appears to lose virtually all of its phase separation. Its topography appears to also become more homogenous by 140 °C. It is not clear from these data whether these observed changes occur in the bulk as well as the surface, but it is speculated that they may. Using variable temperature small-angle X-ray scattering, Page et al. [19] have observed decreased anisotropy in the morphologies of oriented Nafion films during heating to elevated temperatures. These observations support the idea that the changes observed on the membrane surface in Figure 3.6 may also be occurring in the membrane bulk.

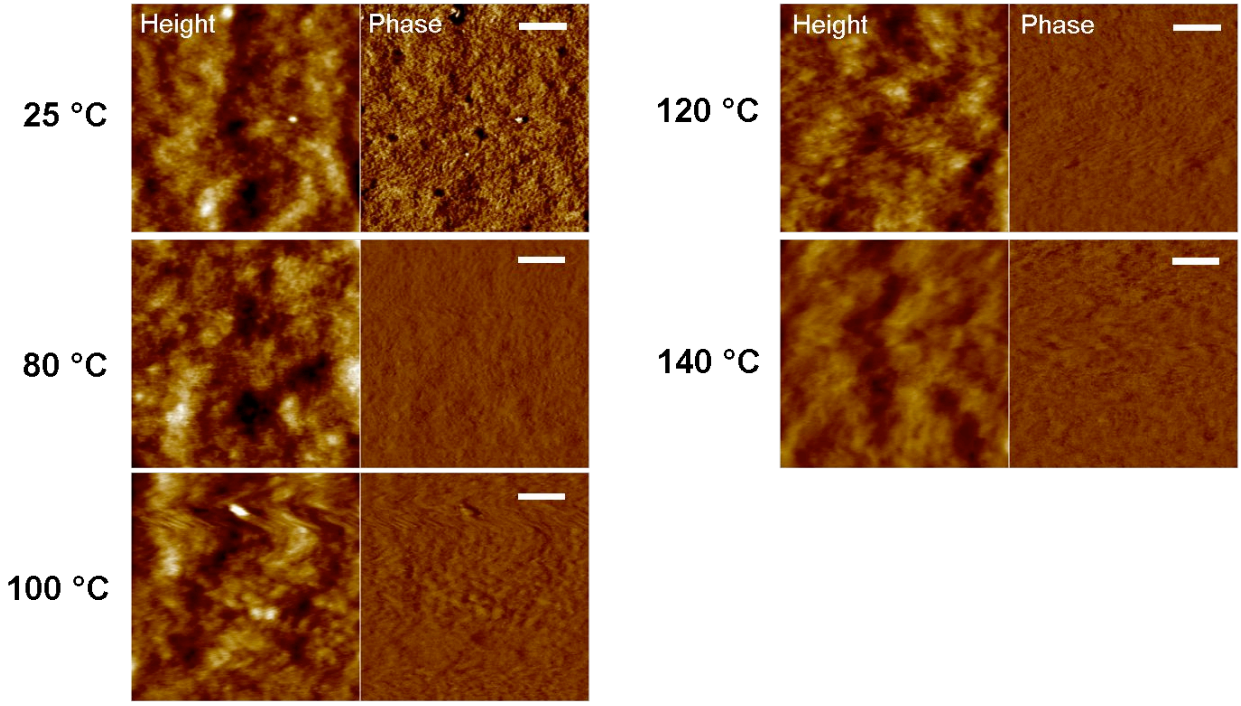

Figure 3.6. Hot stage AFM micrographs of Nafion 112. Setpoint Ratios: 0.85, 0.83, 0.85, 0.86, 0.84; Height images: z = 10 nm; Phase images: z = 15°. Scale bars = 100 nm.

It has been shown previously that observable differences in the phase micrographs of Nafion are caused by water adsorbed on those regions as it dampens the oscillation of the AFM cantilever [20]. This is true not only for Nafion, but all of the ion-containing copolymers in this study. The regions with adsorbed water are the ones that appear darker in the phase micrographs. It can be easily reasoned that the loss of observable contrast in the phase micrographs with temperature may likely be associated with a loss of water. In particular, the loss of phase separation in Nafion by 80 °C matches well with the reports that Nafion's performance decreases above 80 °C from a loss of hydration. Based on the images above, the

qualitative conclusion can be made that the BPSH100-PI multiblock copolymers appear to lose less water at higher temperatures than BPSH35 random copolymers and BPSH35 copolymers lose less water than Nafion 112 at high temperatures. In addition, the observation that phase separation is lost at different temperatures for different block lengths suggests that block length may enhance the thermal utility of the BPSH100-PI membranes by postponing water desorption.

Nevertheless, it was still unclear by only looking at these AFM images, whether these observed changes in morphology are the result of changes in temperature or moisture or both. The time required to both equilibrate the samples at each temperature and obtain each image prevents continuous imaging of the membranes with temperature, so it is uncertain if the observed changes happen continuously or at fixed temperatures. Also, the time required to obtain an artifact-free image at each temperature can vary, resulting in subtle variations in heating rates of the samples. Several hypotheses were proposed to explain the images. The observed changes in the multiblock copolymers might be the result of exceeding an order-disorder transition temperature [21], although this was doubtful. The observed changes might be the loss of water liberated at specific temperatures corresponding with thermal transitions of the polymers. Alternatively, the changes in the surface morphology might be a result of the loss of water in stages--free water might be lost first, followed by loosely bound water, and finally tightly bound water. This loss of water might be throughout the membranes or just limited to the surface. Several additional experiments were performed to further elucidate the observations.

3.3.2 Hot stage AFM reversibility testing

Reversibility testing of a BPSH100-PI membrane at elevated temperatures was performed to determine the reversibility of the effects of elevated temperature as well as gaining additional knowledge about whether these effects are caused more by temperature or water desorption (Figure 3.7). A BPSH100-PI 15k-15k film sample (Figure 3.7a) was heated to 155 °C in the same way it was heated in the first study, pausing for 30 minutes at several increasing temperatures. The sample was then cooled to ambient temperature and kept at 30% RH for over a week.

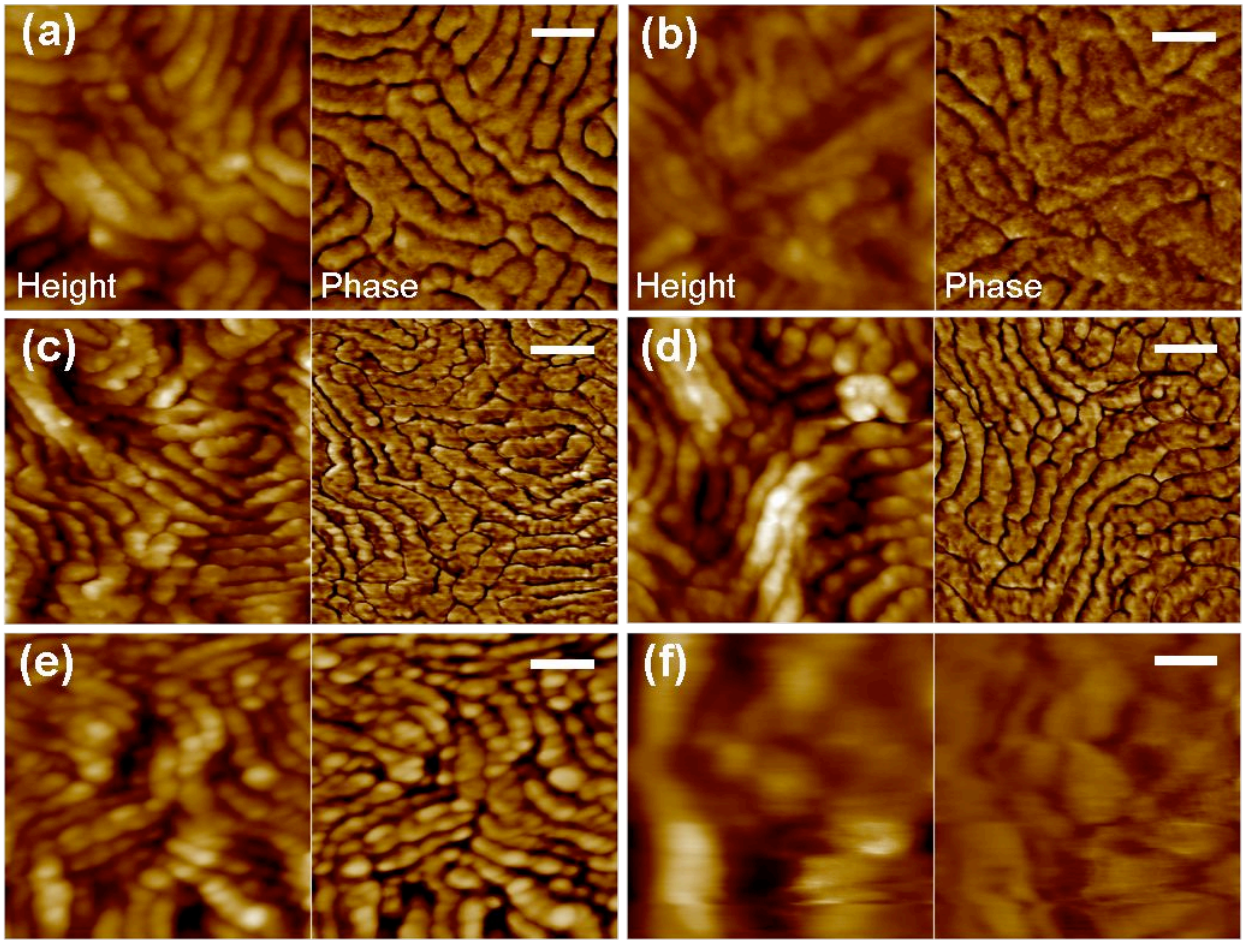

Figure 3.7. A BPSH100-PI 15k-15k multiblock copolymer: (a) at ambient conditions, (b) at ambient conditions after heating to 155 °C, (c) at ambient conditions following rehydration in HPLC water, (d) at ambient conditions after a 45 minute isotherm at 180 °C. A second sample: (e) at ambient conditions following extensive hydration in HPLC water, (f) after a 1 h isotherm at 180 °C. Setpoint ratios: (0.86, 0.85, 0.79, 0.82, 0.95, 0.97); Height images: z = 30 nm; Phase images: z = 30° (a-d), 40° (e,f); Scale bars = 100 nm.

The sample was imaged at room temperature and ambient humidity (63% RH; Figure 3.7b). The resulting image displayed fair phase separation, but not quite as sharp as its original image (Figure 3.7a), suggesting that some moisture had been lost from the surface. The membrane was rehydrated by immersion in HPLC water for three days, dried under vacuum at 60 °C for three hours to remove surface moisture, kept at 30% RH for over 12 hours, and then imaged at 25 °C and ambient humidity (49% RH; Figure 3.7c). Its appearance was very close to what was expected for the membrane at ambient conditions. The image is slightly different than the original one, suggesting there may be some hysteresis effects involved with drying and rehydrating. Such hysteresis has been observed before in the conductivity measurements of

proton exchange membranes taken at ascending versus descending relative humidities. This membrane was then heated at 180 °C for 45 minutes, equilibrated at ambient temperature for 30 minutes, and imaged again at room temperature and ambient humidity (47% RH; Figure 3.7d). Despite maintaining the temperature at which phase separation was lost in Figure 3.3, the AFM micrograph of this membrane was virtually identical to how it looked before heating to 180 °C. Thus, there was less change observed in the phase image for the sample heated to a higher temperature for a shorter time at a faster rate than for the sample heated to a lower temperature for a longer time at a slower rate. These data suggest that the changes in the micrographs of this copolymer at elevated temperature are more the result of heating rate, and not specifically temperature alone. To further confirm this, another BPSH100-PI 15k-15k sample was hydrated in HPLC water for over one week, dried under vacuum at 60 °C for three hours, kept at 30% RH for over 12 hours, and then imaged at 25 °C and around 55% RH (Figure 3.7e). The phase separation observed was sharp, but the hydrophilic phase appeared a little larger than before, likely because of the longer hydration time. The membrane was heated at 180 °C for one hour and imaged (Figure 3.7f). The topography and phase separation were completely distorted, but the observable phase shift was far more prominent than the previous image at 180 °C in Figure 3.3. These results further indicate that the changes observed at each temperature are not directly a result of temperature, but rather a direct result of heating rate.

3.3.3 Thermal transitions

Considerable thought was given to the thermal transitions of the copolymers while contemplating the cause of the changes in the AFM images at elevated temperature. However, it was known from DMA testing that partially fluorinated 6FSH32 random copolymers, whose molar ion concentration is similar to that of BPSH35, do not display any sort of relaxation above room temperature until their glass transition temperature around 220 °C [22]. There is no reason to believe that BPSH35 would display additional transitions beyond the one observed for 6FSH32. This idea is supported by the knowledge that BPSH30 and BPSH40 random copolymers have been reported by DSC to have single glass transition temperatures of 260 °C and 271 °C, respectively [23], suggesting that BPSH35 displays transitions within this range. The transition(s) of the BPSH100-PI were not known because attempts to characterize the thermal transitions of the acid form of the multiblock copolymer without degrading the acid

groups proved impossible. More recently, it has been shown that the salt form of the multiblock copolymer displays a single distinct transition above ambient temperature roughly around 350 °C [17]. These data strongly disprove the notion that a glass transition may be responsible for the observed phenomena. Nevertheless, a question remained about whether moisture within the multiblock copolymer membranes might be plasticizing them, enabling the possibility of a lower hydrated glass transition.

Differential scanning calorimetry was performed on the BPSH100-PI 15k-15k multiblock copolymer to determine its water depressed glass transition temperature (T_{wdg}) as a function of water content (Figure 3.8). The influence of the different states of water on this phenomenon has been reported previously {Kim, 2003 #320}. When the copolymer is fully hydrated with 85 wt% water content, its T_{wdg} is 121 °C. As the membrane becomes less hydrated, its T_{wdg} gradually rises. By the time the membrane water content drops to 11 wt%, the T_{wdg} rises to 218 °C. Based on TGA measurements, the water content of the BPSH100-PI membrane at the start of AFM imaging was around 7 wt%. Consequently, the T_{wdg} of the multiblock copolymer was somewhere between 218 °C and the T_g of 350°C determined for the salt form before imaging began. This T_{wdg} would have risen during the course of the study as temperature increased and more water was liberated from the membrane, so it can be concluded with certitude that the T_{wdg} of the BPSH100-PI was always higher than the imaging temperature. This assertion further disproves the hypothesis that changes in the images observed were a result of thermal transitions in the copolymers.

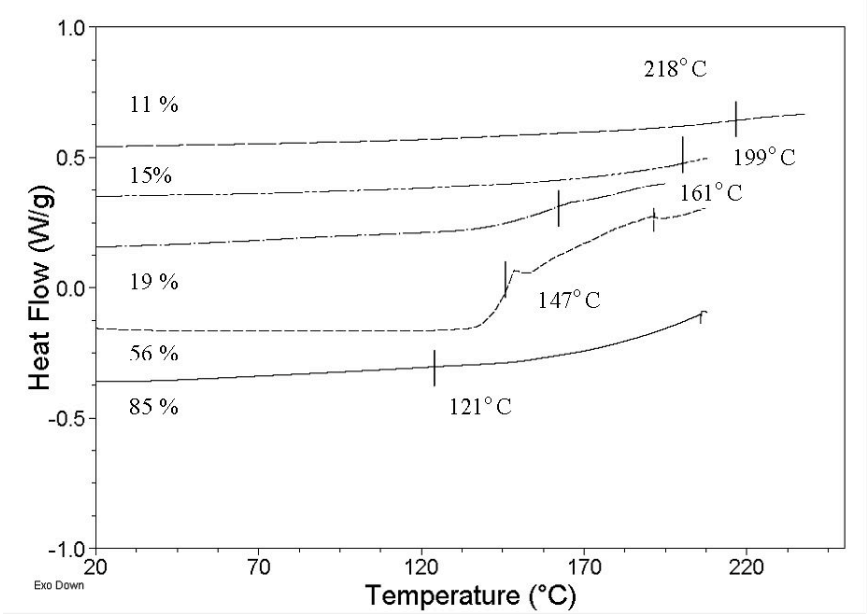

Figure 3.8. The water depressed Tg of BPSH100-PI 15k-15k as a function of its water content. The percentages on the left hand side represent water uptake values (wt% of water within the membrane) and the temperatures on the right represent glass transition temperature.

3.3.4 Water desorption

Thermogravimetic analysis was performed on the membranes in this study in an effort to quantify the relative amounts of water desorbing from the membranes. It is important to note that the ion exchange capacities and water uptake values were not identical for each membrane (Table 1). Ion exchange capacity is defined as the number of ionic sites per gram of dry polymer. As a result, there was the potential for the membranes with the higher water uptake to possess more moisture before analysis and thus lose more during testing. In order to alleviate this disparity, weight loss measured for each membrane at a constant heating rate of 2.5 °C/min was normalized by ion exchange capacity and expressed as the number of water molecules desorbed per ionic site.

Table 3.1. Ion exchange capacities and water uptake values for membranes analyzed by TGA.

Sample	IEC[a] (meq./g)	Water Uptake (%)
BPSH35-20k[b]	1.49	40
BPSH35-30k[b]	1.50	43
BPSH35-50k[b]	1.52	38
Nafion 112	0.91	25
NRE 211	0.91	25
BPSH100-PI 5k-5k[c]	1.65	59
BPSH100-PI 10k-10k[c]	1.57	67
BPSH100-PI 15k-15k[c]	1.55	85

[a]Ion Exchange Capacity determined by titration
[b]Data taken from reference [18].
[c]Data taken from reference [13].

In Figure 3.9, it can be seen that the amount of water lost by the BPSH35 random copolymers and the Nafions at 120 °C were within the same range, between 3.55 and 4.13 water molecules per ionic site. Water loss does not appear to trend with molecular weight, which was anticipated for reasons discussed earlier. Nafion 112, despite its partial crystallinity [10], does not retard water desorption any better than the BPSH35 random copolymers but rather loses it even faster, except between 82 and 98 °C when it loses it at the same rate. Recast Nafion (NRE 211), which is thought to be less crystalline than Nafion 112, retains moisture better than the random copolymers between 50 and 126 °C, but as temperature increases, its water loss is not much different than theirs. Water loss in the BPSH35 random copolymers appears to be continuous, not occurring in discreet stages, disproving the hypothesis that the differences observed in the AFM phase images at different temperatures may be a result of separate desorptions of the different states of water. Both Nafion 112 and Recast Nafion appear to display an increased rate of water loss roughly around 80 °C observed as an inflection in their curves. This may explain why a stark decrease in contrast was observed in the AFM phase micrograph for Nafion at 80 °C in Figure 3.5. The reason for this increased rate of water loss may be the α-transition of Nafion, which has been reported to be around 100 ºC for the H^+-form of Nafion 1100EW [24]. The temperature of this α-transition may be depressed at partially hydrated conditions like the ones in this study. Consequently, it is possible that the Nafion films in this study are experiencing greater molecular mobility at 80 ºC as a result of the water-

depressed α-transition resulting in the increased water desorption observed in Figure 3.9. This speculation is bolstered by the observation that increased water desorption occurs at the same temperature for both Nafion 112 and Recast Nafion, which suggests that this behavior is independent of morphology.

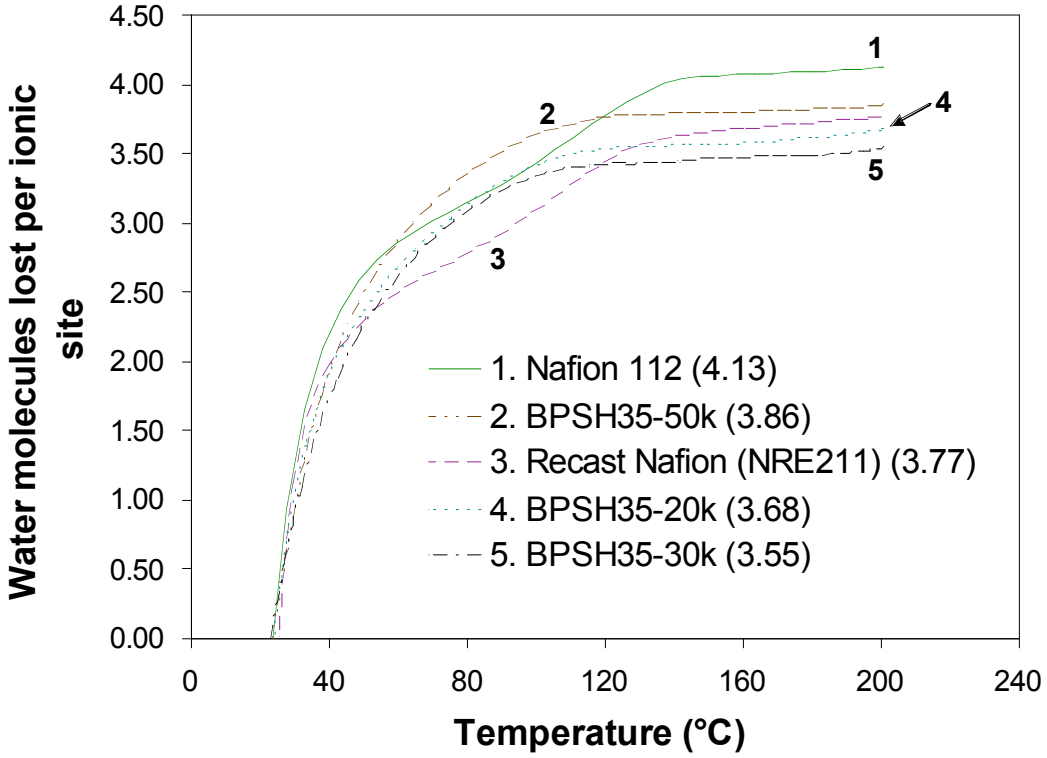

Figure 3.9. Water molecules lost per ionic unit as a function of time for BPSH35 random copolymers, Nafion 112 and recast Nafion (NRE 211). Numbers in parentheses denote maximum number of water molecules lost at 120 °C.

The water loss with temperature of the multiblock copolymers is displayed in Figure 3.10, with recast Nafion inserted to provide a means of comparison with Figure 3.9. Recast Nafion retains more water than the BPSH100-PI multiblock copolymer with the smallest block length, 5k-5k, from 50 °C until just above 100 °C, but as the temperature increases past 100 °C, recast Nafion continuously loses more water than the 5k-5k multiblock copolymer. The curves for the other two multiblock copolymers indicate that water retention increases with block length. This is a noteworthy observation because water uptake also increases with block length. Therefore, even though the water uptake of the 15k-15k multiblock copolymer is 44% higher than that of the 5k-5k copolymer, it retains about 22% more moisture per ionic site. Stated in a different way, the 5k-5k copolymer loses 28% more moisture per ionic site than the 15k-15k copolymer which has more adsorbed water ab initio. These data corroborate the AFM images

obtained for these multiblock copolymers in Figures 3.2 and 3.3. Less water loss at elevated temperatures than the random copolymers and Nafion explains why moisture induced contrast in the phase micrographs was observed up to higher temperatures for the multiblocks compared to the random copolymers and Nafion.

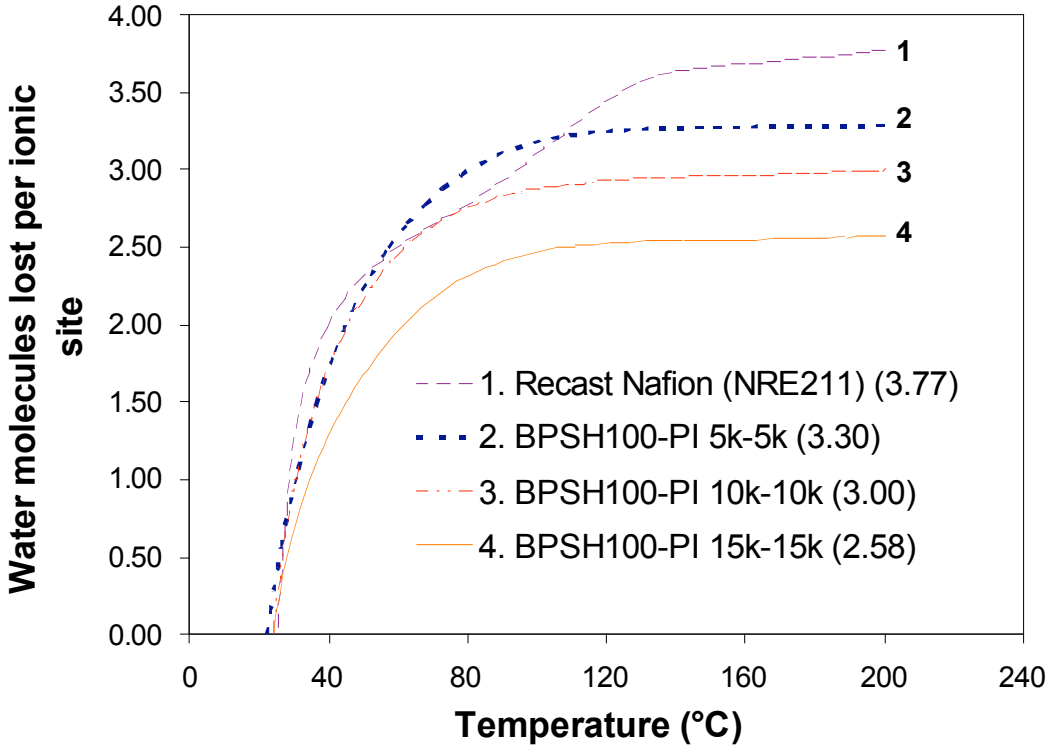

Figure 3.10. Water molecules lost per ionic unit as a function of time for BPSH100-PI multiblock copolymers and recast Nafion (NRE 211). Numbers in parentheses denote maximum number of water molecules lost at 120 °C.

It is important to recognize that the rate and amount of water loss during heating will not only be a function of morphology, but also, of course, of the relative humidity of the environment during heating. Therefore, any precisely quantitative measurement of water loss must account for relative humidity during testing. Although this parameter could not be controlled during any part of this study, the qualitative conclusions about water loss decreasing with block length can still be made.

Measurements of water desorption from the membranes were also made at constant temperature in addition to constant heating rate. Immediately after the membranes in Figures 3.9 and 3.10 were heated to 200 °C, they were subjected to an isotherm at 200 °C for one hour to evaluate their ability to retain moisture at constant elevated temperature. This temperature was higher than any of those at which all contrast was observed to disappear in the AFM images. In

addition it was assumed that if the moisture content of a membrane was stable at 200 °C, it should conceivably be stable at lower temperatures as well. The results of these measurements are summarized in Figure 3.11. All of the random copolymers and the two Nafion samples lose additional water during the hour-long isotherm. There is no observable effect of molecular weight on the water loss of the random copolymers, which was expected based on the results of observed at constant heating rate. The Nafion samples lose an equal amount of water during the isotherm. This data matches well with the data in Figure 3.9 in which recast Nafion retains more water than Nafion 112 but their water loss behaviors parallel each other. Two out of three of the BPSH100-PI multiblock copolymers do not lose any water during the isotherm. The 10k-10k copolymer loses an additional 0.08 water molecules per ionic site which is still less than the amount lost by the BPSH35 copolymers and Nafions. These data suggest that the phase separated morphologies of the BPSH100-PI multiblock copolymers not only allow these copolymers to retain more moisture during heating to elevated temperatures, but may also aid in water retention at elevated temperatures for extended periods.

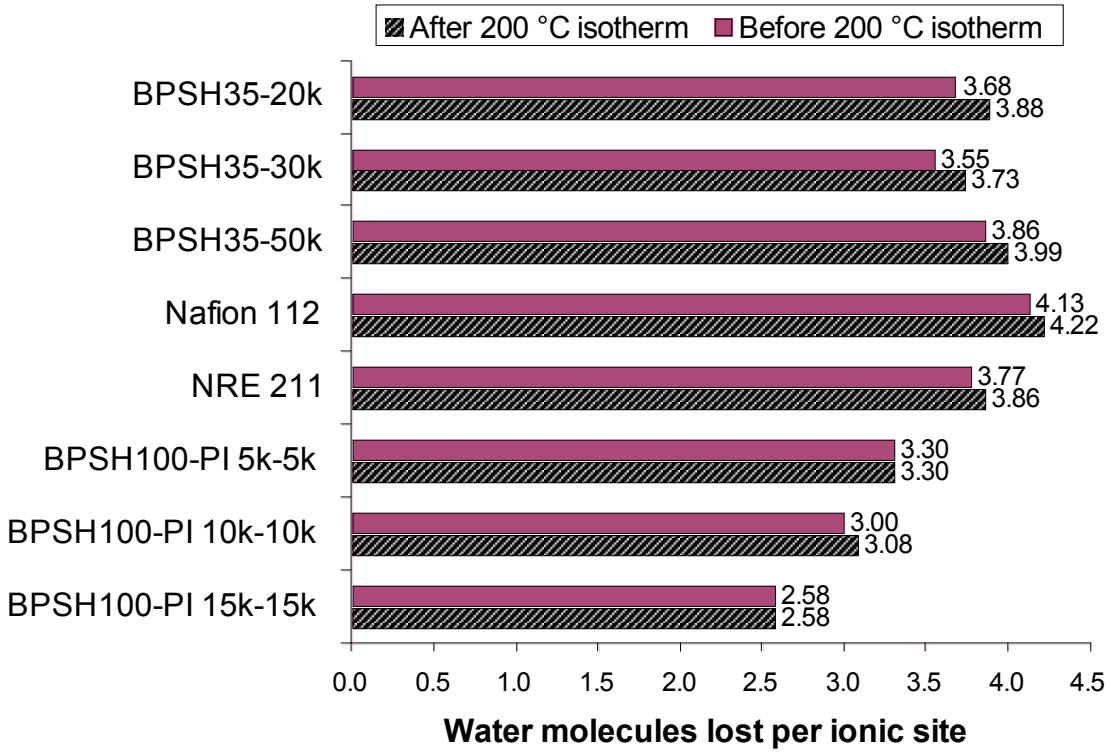

Figure 3.11. Water molecules lost per ionic unit before and after an isotherm of 200 °C for 1 h.

One question remaining after thermogravimetric analysis was whether the observed water desorption was limited to the surface of the membranes or if water was lost from the bulk of the membranes. FT-IR spectroscopy was performed on the random BPSH35-50k membrane to clarify this issue. In Figure 3.12 the water peak at 3500 cm^{-1} appears clearly in the spectrum obtained at 25 °C. This peak decreases almost completely as the temperature is increased to 80 °C and can no longer be seen in the spectrum at temperatures above 80 °C.

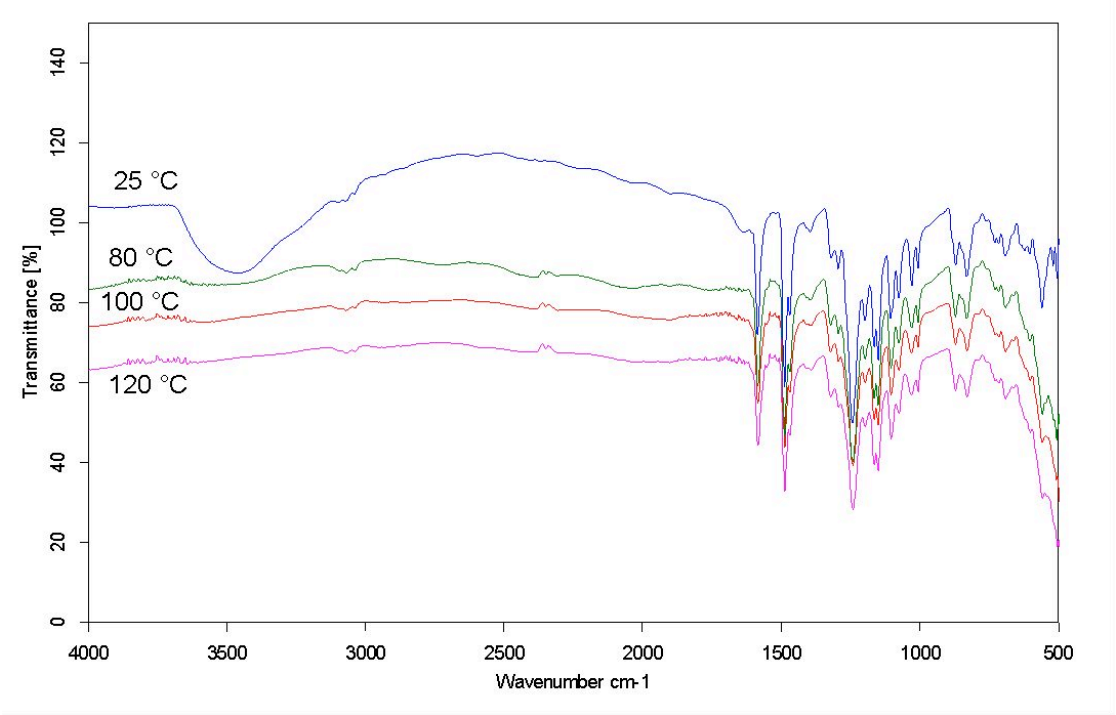

Figure 3.12. FT-IR spectra of BPSH35-50k showing loss of water with increasing temperature.

These results confirm that water is indeed being lost from the bulk of the membrane. The water loss observed in these spectra correlate fairly well with the AFM images for BPSH35-50k in which the contrast in the phase image begins decreasing by 100 °C. Water desorption may likely have occurred faster in the film used for FT-IR measurements because it was much thinner than the one used for AFM imaging. FT-IR measurements were not performed for the BPSH100-PI multiblock copolymers because they were too thick to obtain good spectra and recasting and acidifying them at a thickness thin enough for FT-IR measurements proved extremely difficult. Had thinner membranes been recast successfully, it was still questionable if their phase-separated morphologies and thus their water retention ability would have been identical to the original membranes whose thickness ranged from 0.6 to 1.3 mils (15 to 33 μm).

3.4 Conclusions

The high temperature behavior of BPSH100-PI multiblock copolymer membranes in terms of morphological stability and water retention was evaluated and compared to that of BPSH-based random copolymers and Nafion. Atomic force micrographs of the membranes obtained at elevated temperatures revealed a loss of topography and phase separation that increased with temperature, attributed to water desorption from the membranes. However, this desorption was observed to be much less for the multiblock copolymers than for the random copolymers and Nafion. No changes to the BPSH100-PI 15k-15k multiblock copolymers were observable at 145 °C and phase separation was still observable at 155 °C. A study of the reversibility of the observed changes to the BPSH100-PI 15k-15k multiblock copolymer at high temperature revealed that these changes are more a function of the rate at which the sample is heated than merely temperature. DSC and DMA measurements ruled out thermal transitions of the copolymer membranes as the cause of the observable changes in their micrographs at elevated temperature. Thermogravimetric analysis confirmed the suspicion that the high temperature behavior observed by AFM was a result of a continuous loss of water from the membranes with increasing temperature. The TGA results indicate that the phase separated morphologies of the BPSH100-PI multiblock copolymers not only allow these copolymers to retain more moisture during heating to elevated temperatures, but may also aid in the retention of water at elevated temperatures for extended periods, especially as block length increases. FT-IR spectroscopy measurements indicated that the loss of water, and thus the retention of water, at elevated temperatures is a bulk phenomenon, not limited to just the surface of the membranes. The results of this study indicate that BPSH100-PI multiblock copolymers are thermally stable and retain water at 120 °C and higher, suggesting that these copolymers, especially the one with the largest block length, are candidates for high temperature PEMs. The conductivity and MEA performance of BPSH100-PI 15k-15k will be addressed in a future publication.

3.5 Acknowledgements

The authors wish to thank the National Science Foundation “Partnership for Innovation” Program (HER-0090556) and IGERT Program (DGE-0114346), the Department of Energy (DE-FG36-06G016038), and the Nissan Motor Company for supporting this research.

3.6 References

1. Roziere, J. and D.J. Jones, *Non-fluorinated polymer materials for proton exchange membrane fuel cells.* Ann. Rev. Mat. Res., 2003. **33**: 503-555.

2. Alberti, G. and M. Casciola, *Composite membranes for medium-temperature PEM fuel cells.* Ann. Rev. Mat. Res., 2003. **33**: 129-154.

3. Hickner, M.A., H. Ghassemi, Y.S. Kim, B.R. Einsla, and J.E. McGrath, *Alternative polymer systems for proton exchange membranes (PEMs).* Chem. Rev., 2004. **104**(10): 4587-4611.

4. Miyatake, K. and M. Watanabe, *Recent progress in proton conducting membranes for PEFCs.* Electrochem., 2005. **73**(1): 12-19.

5. Hamrock, S.J. and M.A. Yandrasits, *Proton exchange membranes for fuel cell applications.* Polym. Rev., 2006. **46**(3): 219-244.

6. *R&D plan for the high temperature membrane working group*. 2003, Department of Energy Office of Efficiency and Renewable Energy's Hydrogen, Fuel Cells & Infrastructure Technologies Program

7. Yang, C., P. Costamagna, S. Srinivasan, J. Benziger, and A.B. Bocarsly, *Approaches and technical challenges to high temperature operation of proton exchange membrane fuel cells.* J. Power Sources, 2001. **103**(1): 1-9.

8. Shao, Y.Y., G.P. Yin, Z.B. Wang, and Y.Z. Gao, *Proton exchange membrane fuel cell from low temperature to high temperature: Material challenges.* J. Power Sources, 2007. **167**(2): 235-242.

9. Zhang, J.L., Z. Xie, J.J. Zhang, Y.H. Tanga, C.J. Song, T. Navessin, Z.Q. Shi, D.T. Song, H.J. Wang, D.P. Wilkinson, Z.S. Liu, and S. Holdcroft, *High temperature PEM fuel cells.* J. Power Sources, 2006. **160**(2): 872-891.

10. Mauritz, K.A. and R.B. Moore, *State of understanding of Nafion.* Chem. Rev., 2004. **104**(10): 4535-4585.

11. Li, Q.F., R.H. He, J.O. Jensen, and N.J. Bjerrum, *Approaches and recent development of polymer electrolyte membranes for fuel cells operating above 100 degrees C.* Chem. Mater., 2003. **15**(26): 4896-4915.

12. Jannasch, P., *Recent developments in high-temperature proton conducting polymer electrolyte membranes.* Curr. Op. Colloid & Interf. Sci., 2003. **8**(1): 96-102.

13. Lee, H.-S., A. Roy, A.S. Badami, and J.E. McGrath, *Segmented sulfonated poly(arylene ether sulfone)-b-polyimide copolymers for proton exchange membrane fuel cells. I. Copolymer synthesis and fundamental properties.* J. Polym. Sci. Part A: Polym. Chem., 2007. **45**: 4879-4890.

14. Kim, Y.S., F. Wang, M. Hickner, S. McCartney, Y.T. Hong, W. Harrison, T.A. Zawodzinski, and J.E. McGrath, *Effect of acidification treatment and morphological stability of sulfonated poly(arylene ether sulfone) copolymer proton-exchange membranes for fuel-cell use above 100 degrees C.* J. Polym. Sci.: Part B: Phys, 2003. **41**(22): 2816-2828.

15. Cornet, N., O. Diat, G. Gebel, F. Jousse, D. Marsacq, R. Mercier, and M. Pineri, *Sulfonated polyimide membranes: A new type of ion-conducting membrane for electrochemical applications.* J. New Mater. Elect. Sys., 2000. **3**(1): 33-42.

16. Roy, A., M.A. Hickner, H.-S. Lee, A. Badami, X. Yu, Y. Li, T. Glass, and J.E. McGrath, *Transport properties of proton exchange membranes.* ECS Transactions, 2007. **2**(24, Direct Methanol Fuel Cells): 45-54.

17. Badami, A.S., H.-S. Lee, Y. Li, A. Roy, H. Wang, and J.E. McGrath, *Molecular weight effects upon poly(arylene ether sulfone)-based random and multiblock copolymers for fuel cells.* Polymer, 2008: *submitted*.

18. Li, Y.X., F. Wang, J. Yang, D. Liu, A. Roy, S. Case, J. Lesko, and J.E. McGrath, *Synthesis and characterization of controlled molecular weight disulfonated poly(arylene ether sulfone) copolymers and their applications to proton exchange membranes.* Polymer, 2006. **47**(11): 4210-4217.

19. Page, K.A., F.A. Landis, A.K. Phillips, and R.B. Moore, *SAXS analysis of the thermal relaxation of anisotropic morphologies in oriented Nafion membranes.* Macromolecules, 2006. **39**(11): 3939-3946.

20. James, P.J., M. Antognozzi, J. Tamayo, T.J. McMaster, J.M. Newton, and M.J. Miles, *Interpretation of contrast in tapping mode AFM and shear force microscopy. A study of Nafion.* Langmuir, 2001. **17**(2): 349-360.

21. Bates, F.S. and G.H. Fredrickson, *Block copolymer thermodynamics - theory and experiment.* Ann. Rev. Phys. Chem., 1990. **41**: 525-557.

22. Badami, A.S., H.-S. Lee, Y. Li, A. Roy, H. Wang, and J.E. McGrath, *Morphological analysis of molecular weight effects upon non- and partially-fluorinated disulfonated poly(arylene ether sulfone)-based random and multiblock copolymers for fuel cells.* Prepr. Pap. - Am. Chem. Soc., Div. Fuel Chem, 2006. **51**(2): 612-614.

23. Wang, F., M. Hickner, Y.S. Kim, T.A. Zawodzinski, and J.E. McGrath, *Direct polymerization of sulfonated poly(arylene ether sulfone) random (statistical) copolymers: Candidates for new proton exchange membranes.* J. Memb. Sci., 2002. **197**(1-2): 231-242.

24. Page, K.A., K.M. Cable, and R.B. Moore, *Molecular origins of the thermal transitions and dynamic mechanical relaxations in perfluorosulfonate ionomers.* Macromolecules, 2005. **38**(15): 6472-6484.

Chapter 4. Fundamental Investigations of the Effect of the Linkage Group on the Behavior of Hydrophilic-Hydrophobic Poly(arylene ether sulfone) Multiblock Copolymers for Proton Exchange Membrane Fuel Cells

Anand S. Badami, Ozma Lane, Hae-Seung Lee, Abhishek Roy, and James E. McGrath

Department of Chemistry, Macromolecular Science and Engineering Program, Macromolecules and Interfaces Institute, Virginia Polytechnic Institute and State University, Blacksburg, VA 24061, USA

Abstract

A growing number of research efforts in the field of alternative proton exchange membranes involve multiblock copolymer chemistries. Virtually all of this research has exclusively focused on the effects of oligomer chemistry and block length with little emphasis placed on the methods used to couple the oligomers. Fluorine-terminated linkage groups are desirable for these coupling reactions because they can lower reaction temperatures, minimizing side reactions like randomization. While the choice of such linkage groups may have obvious economic consequences, the potential effect on membrane morphology, proton conductivity, and other properties is not as well-known. The current study evaluates the effect of two different fluorine-containing linkage groups, hexafluorobenzene (HFB) and decafluorobiphenyl (DFBP), on the morphology and PEM properties of multiblock copolymers comprised of disulfonated and unsulfonated poly(arylene ether sulfone) oligomers of varied block lengths. Data from AFM, TEM, XPS, DMA, TGA, Instron, and proton conductivity testing indicate that the choice of linkage type appears to have some small but observable influences on the multiblock copolymers. The higher fluorine content of the DFBP linkage promotes greater phase separation than the HFB linkage, resulting in increased stiffness and decreased ductility. The DFBP linkage also appears to promote more surface enrichment of fluorine, causing changes in surface morphology and slightly increased water desorption. The lack of perfect correspondence between the microscopy and proton conductivity data is attributed to the differences inherent in the measurements and the ability of ionic domains to swell with hydration. The biggest effect of linkage type appears to be increased proton conductivity at partially hydrated conditions for DFBP-containing copolymers.

4.1 Introduction

The desire to develop an alternative source of energy to reduce the consumption of fossil fuels is a global concern. One of the many fields in which research to achieve this objective is being conducted is proton exchange membrane fuel cells (PEMFCs). These energy conversion devices have the potential to power automobiles, homes and other buildings, and portable electronic devices in a manner that is both environmentally friendly as well as potentially very efficient (60-70% or more) [1, 2]. An essential component of every PEMFC is its proton exchange membrane (PEM). A successful PEM must possess several characteristics including high protonic conductivity, impermeability to fuel and oxidant feed streams, good mechanical properties to ensure its durability, good water management, and cost effectiveness [3]. The current PEM standard is Nafion®, a poly(perfluorosulfonic acid) manufactured by the E. I. duPont Company, which provides good proton conductivity, chemical stability, and mechanical stability at temperatures up to 80 °C with sufficient hydration. In addition to its strengths, however, Nafion® also exhibits formidable limitations including cost, fuel permeability, and decreased performance accompanying loss of hydration above 80 °C [3].

Given the deficiencies of Nafion®, a variety of different chemistries have been explored for use as alternative PEMs over the last few decades as outlined in several reviews [3-8]. The majority these alternative membrane solutions have traditionally been focused on copolymers with randomly or statistically assembled comonomers. In our laboratory we have recently begun to investigate the possibility that thermally stable hydrophilic-hydrophobic multiblock copolymers may show some advantages over random and statistical copolymers [9-17]. Multiblock copolymers may prove more advantageous than random copolymers for several reasons. First, higher proton conductivity at low relative humidities is possible with multiblock copolymers [15-19], possibly due to higher water self-diffusion rates. Second, the nanophase separated morphology of multiblocks can be precisely controlled by synthesis (e.g. the relative amounts and chemistries of the hydrophobic and hydrophilic domains). This may enable the formation of a cocontinuous lamellar morphology in which the hydrophobic domains provide mechanical strength while the hydrophilic domains form channels through which protons can easily be conducted. Third, this flexibility in multiblock copolymer synthesis should allow further tuning of the mechanical strength, water uptake, and swelling, among other membrane properties.

The focus of the published literature to date regarding multiblock copolymers as alternative PEMs has been on manipulating the chemistries or block lengths of the oligomers used to synthesize the multiblock copolymers. Very little to no emphasis has been placed on the ramifications of the methods by which the oligomers are coupled together. Some oligomers are synthesized with reacting endgroups to facilitate coupling, while others need to be endcapped with small "linker" molecules. Fluorinated molecules like hexafluorobenzene and decafluorobiphenyl are attractive candidates for such linkages because their terminal fluorine groups act as good leaving groups to enhance the kinetics of the oligomer coupling reaction, allowing the reaction to proceed at lower temperatures. This is very desirable for the coupling reaction because side reactions including randomization (i.e. ether-ether interchange) are minimized at lower temperatures. In other words, lowering the temperature of the coupling reaction by using fluorinated linker molecules will help maximize the block efficiency of the coupling reaction.

Given that the use of fluorinated linker molecules yields better multiblock copolymers, the question regarding multiblock copolymer synthesis strategy shifts from whether or not to use these molecules to which fluorinated linker molecule is the best choice for multiblock copolymer coupling, hexafluorobenzene (HFB) or decaflurobiphenyl (DFBP). At first glance, HFB seems appealing because it is commercially available and would thus be a more economical choice. DFBP, on the other hand, would be more costly, but it is a larger molecule with more fluorine atoms that would increase the effective size of the linkage group by one tetrafluorobenzene molecule. Even though this size difference is small, it is not necessarily trivial.

While the size of a fluorinated linker molecule is negligible compared to the molecular weight of the resulting multiblock copolymer, its effect upon the multiblock copolymer's nanophase separated morphology may or may not have some significance. Introducing additional hydrophobic fluorine moieties into a multiblock copolymer may disrupt the original balance of hydrophilic and hydrophobic components in the copolymer. If large enough, this disruption may increase the Flory-Huggins χ parameter of the copolymer which may increase the driving force for nanophase separation within the copolymer [20-22]. It is important to note that classical theory of phase separation in block copolymers is not fully applicable in ion-containing polymers. "Specific interactions" between ionic charges within these polymers may increase the attractive forces between polymer chains, thereby reducing the χ parameter and the resulting

degree of phase separation. At present, there is no accepted method to calculate the χ parameter for novel ion-containing PEMs, so it is not possible to quantifiably predict the effect of linkage group on PEM morphology. Nevertheless, there is a possibility that a linkage group induced change in nanophase separation may affect the performance characteristics of the PEM that are influenced by morphology including, but not limited to, proton conductivity, water retention, and mechanical strength. This fact warrants a study of the effect of linkage group choice on multiblock copolymer morphology and related PEM properties, especially considering that research in multiblock copolymer PEMs is very active.

The present study evaluates the effect of two different fluorine-containing linkage groups on the morphology and PEM properties of multiblock copolymers comprised of disulfonated and unsulfonated poly(arylene ether sulfone) oligomers of varied block lengths. Disulfonated poly(arylene ether sulfone) (BPSH) random copolymers have been demonstrated to display good proton conductivity and chemical/mechanical stability as well as reduced fuel permeability [23]. Unsulfonated poly(arylene ether sulfone) (BPS0) oligomers should also display good chemical/mechanical stability and reduced fuel permeability because of their chemical similarity to the disulfonated copolymers. Fully disulfonated (BPSH100) and unsulfonated oligomers were coupled into multiblock copolymers [24] based on the hypothesis that the segmented hydrophilic BPSH100 block would promote phase separation with unsulfonated BPS0 block to a greater degree than what is possible in random copolymers of BPSH. Hexafluorobenzene (HFB) and decafluorobiphenyl (DFBP) were employed as the linkage groups in this study of two series of BPSH100-BPS0 multiblock copolymers. In one series the hydrophobic BPS0 oligomers were terminated with HFB endgroups (Figure 4.1) and in the other series the hydrophobic BPS0 oligomers were terminated with DFBP endgroups (Figure 4.2).

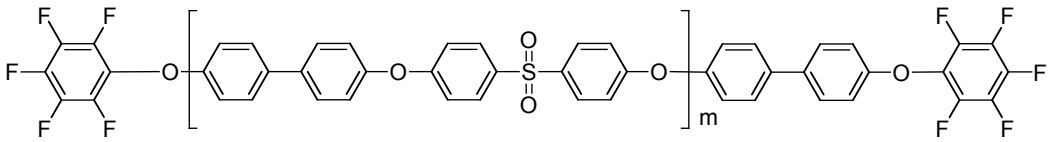

Figure 4.1. Structure of hexafluorobenzene-terminated BPS0 oligomer

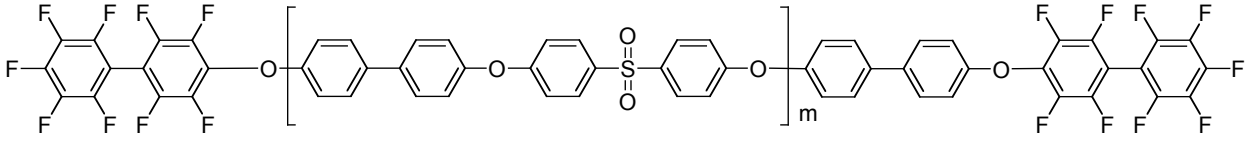

Figure 4.2. Structure of decafluorobiphenyl-terminated BPS0 oligomer

In both series, the hydrophobic BPS0 oligomers were coupled with hydrophilic phenoxide-terminated BPS100 oligomers (Figure 4.3).

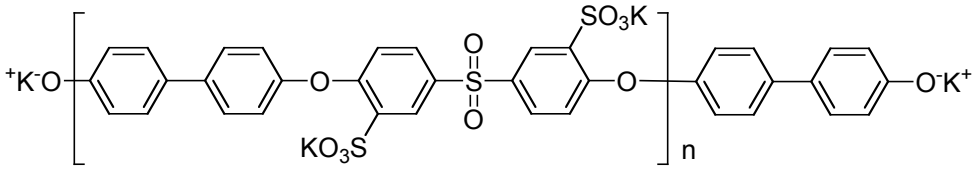

Figure 4.3. Structure of phenoxide-terminated BPS100 oligomer

Oligomer block lengths ranged from ~3 to ~20 kg/mol. Each series was comprised of multiblock copolymers with systematically increasing equal block lengths of BPS100 and BPS0. The DFBP series also contained multiblock copolymers having longer BPS100 block lengths as block length increased. The surface and bulk phase separated morphologies of the copolymers were characterized by atomic force microscopy and transmission electron spectroscopy, respectively. Elemental surface analysis was performed by x-ray photoelectron spectroscopy. Mechanical property data was obtained by tensile testing of the samples. Dynamic mechanical analysis was used to characterize thermal transitions. Water retention was evaluated by thermogravimetric analysis measurements.

4.2 Experimental

4.2.1 Materials

Oligomers of 100 mol% disulfonated poly(arylene ether sulfone) (BPS100) and unsulfonated poly(arylene ether sulfone) (BPS0) random copolymers at target molecular weights ranging from 3 to 20 kg/mol were prepared and coupled together to synthesize multiblock copolymers [24]. This coupling reaction was achieved by first endcapping the phenoxide end groups of a batch of hydrophobic BPS0 oligomers with fluorinated molecules to act as linking agents. One half of the batch was endcapped with hexafluorobenzene (HFB; Figure 4.1) and the other half was endcapped with decafluorobiphenyl (DFBP; Figure 4.2). The target molecular weights of the HFB-terminated BPS0 oligomers were 5, 10, and 15 kg/mol. The target molecular weights of the DFBP-terminated BPS0 oligomers were 3, 5, 10, and 15 kg/mol. Each of these endcapped oligomer groups was separately reacted with a phenoxide-terminated 100 mol% disulfonated poly(arylene ether sulfone) oligomer (BPS100; Figure 4.3) to produce

BPS100-BPS0 multiblock copolymers. The target molecular weights of the phenoxide-terminated BPS100 oligomers were 3, 5, 10, 15, and 20 kg/mol. Each group of BPS0 oligomers was reacted with the BPS100 to produce a series of multiblock copolymers with equal block lengths. The HFB-terminated oligomers were synthesized into BPS100-BPS0 copolymers with block lengths of 5k-5k, 10k-10k, and 15k-15k (e.g. 5k-5k indicates two equal block lengths of 5 kg/mol). The DFBP-terminated oligomers were synthesized into copolymers with block lengths of 3k-3k, 5k-5k, and 10k-10k as well as a series of copolymers with slightly larger block lengths of BPS100 (10k-5k, 15k-10k, and 20k-15k). Further details of the oligomer syntheses and block copolymerization coupling reactions will be described in a forthcoming publication [25].

1-Methyl-2-Pyrrolidinone (NMP; EMD Chemicals) and N,N-Dimethyl-acetamide (DMAc; EMD Chemicals) were used as received. Epofix cold-setting embedding epoxy resin and hardener (Electron Microscopy Sciences) were used as received.

4.2.2 Membrane preparation

Sample films were first prepared by dissolving the copolymers in their potassium sulfonate salt form in NMP at 7% (w/v). Solutions were syringe filtered through 0.45 μm Teflon® filters and cast onto clean glass substrates. The transparent solutions were dried under a 120V, 250W infrared lamp for 48 h and the resultant films were dried under vacuum at 110 °C for 24 h. Films were lifted from their substrates by immersion in deionized water. All films were converted to their acid form (BPSH100-BPS0) by boiling in 0.5 M sulfuric acid for 2 h, rinsing in deionized (DI) water, and then boiling in DI water for 2 h, termed “Method 2” [26]. Acidified films were equilibrated in DI water for 24 h twice. Samples were dried under vacuum at 60 °C for 3 h. While it was difficult to be completely certain this preparation method yields membranes at equilibrium conditions, unpublished AFM data suggest that the morphology of these and other membranes prepared similarly remain consistent over several months.

4.2.3 Intrinsic viscosity

Intrinsic viscosity measurements were determined in NMP at 25 ºC with 0.05M LiBr using an Ubbelohde viscometer [27].

4.2.4 Proton conductivity

Conductivity measurements of acidified membranes were performed at 30 °C in water using a Solartron 1252A + 1287 impedance/gain-phase analyzer over a frequency range of 10 Hz-1 MHz. The cell geometry was chosen to ensure that the membrane resistance dominated the response of the system. The resistance of the film was taken at the frequency that produced the minimum imaginary response.

4.2.5 Water uptake

To obtain water uptake values, membranes were dried for 24 h at 100 °C, weighed, and immersed in deionized water at room temperature for 24 h. The wet membranes were blotted dry and immediately weighed again. Water uptake was calculated as the ratio of the difference between wet and dry membrane weight divided by dry membrane weight and expressed as a weight percent.

4.2.6 Atomic force microscopy (AFM)

Tapping mode AFM was performed using a Digital Instruments MultiMode scanning probe microscope with a NanoScope IVa controller. A silicon probe (Veeco) with an end radius of <10 nm and a force constant of 5 N/m was used to image samples. Samples were equilibrated at 30% relative humidity (RH) for at least 12 h before being imaged immediately at ambient temperature and humidity.

4.2.7 Transmission electron microscopy (TEM)

Electron density contrast within the membrane samples was enhanced by quantitatively titrating the membranes with CsOH solution to exchange the acidic protons with cesium. Membranes were embedded in epoxy and ultramicrotomed into 50-70 nm thin sections with a diamond knife. Transmission electron micrographs were obtained using a Philips EM 420 transmission electron microscope (TEM) operating at an accelerating voltage of 100 kV.

4.2.8 X-ray photoelectron spectroscopy (XPS)

Following equilibration in DI water mentioned above, samples for XPS were placed under vacuum at 80 ºC for ≥ 24 h and then placed in a sealed container at room temperature before characterization. Samples were kept under vacuum in a Perkin Elmer 5400 X-ray photoelectron spectrometer (XPS) at room temperature for 1 h before they were analyzed for surface fluorination. A magnesium filament with a 13 kV source and 0.100 eV broad scan/0.025 eV narrow scan resolution was used in all acquisitions. Samples were oriented to achieve an electron take-off angle of 45º corresponding to a sampling depth of 5 nm.

4.2.9 Dynamic mechanical analysis (DMA)

A TA Instruments DMA 2980 was utilized for dynamic mechanical analysis using a frequency of 1 Hz. An initial drying run to 200 °C for 10 min followed by cooling with liquid nitrogen to 0 °C for 10 min preceded the temperature sweep for each sample. Samples were heated at 5 °C/min to 250 °C. Displacement for each sample was set at approximately 0.1% of sample length.

4.2.10 Tensile testing

Uniaxial load tests were performed using an Instron 5500R universal testing machine equipped with a 200 lb load cell at room temperature and 44-54% relative humidity (RH). Crosshead displacement speed was 5 mm/min and gauge lengths were set to 25 mm. A dogbone die was used to punch specimens 50 mm long with a minimum width of 4 mm. Prior to testing, specimens were dried under vacuum at 100 °C for at least 12 h and then equilibrated at 40% RH and 30 °C. All specimens were mounted in manually tightened grips. At least five replicates were tested for each membrane. Modulus values for each specimen were calculated based on the stress and elongation values for the specimen at the first data point at or above 2% elongation.

4.2.11 Thermogravimetric analysis (TGA)

Thermogravimetric analysis (TGA) was performed on a TA Instruments TGA Q-500. Membrane samples analyzed by TGA were initially placed in a desiccator at 30% RH for at least

48 h. During analysis, the samples were heated in air at 2.5 °C/min from ambient temperature to 200 °C. Immediately following this heated drying run, the samples were held at 200 °C for 1 h.

4.3 Results and Discussion

4.3.1 Morphological characterization

Images of the surface and bulk morphologies of the BPSH100-BPS0 multiblock copolymer series with HFB linkages are presented in Figure 4.4.

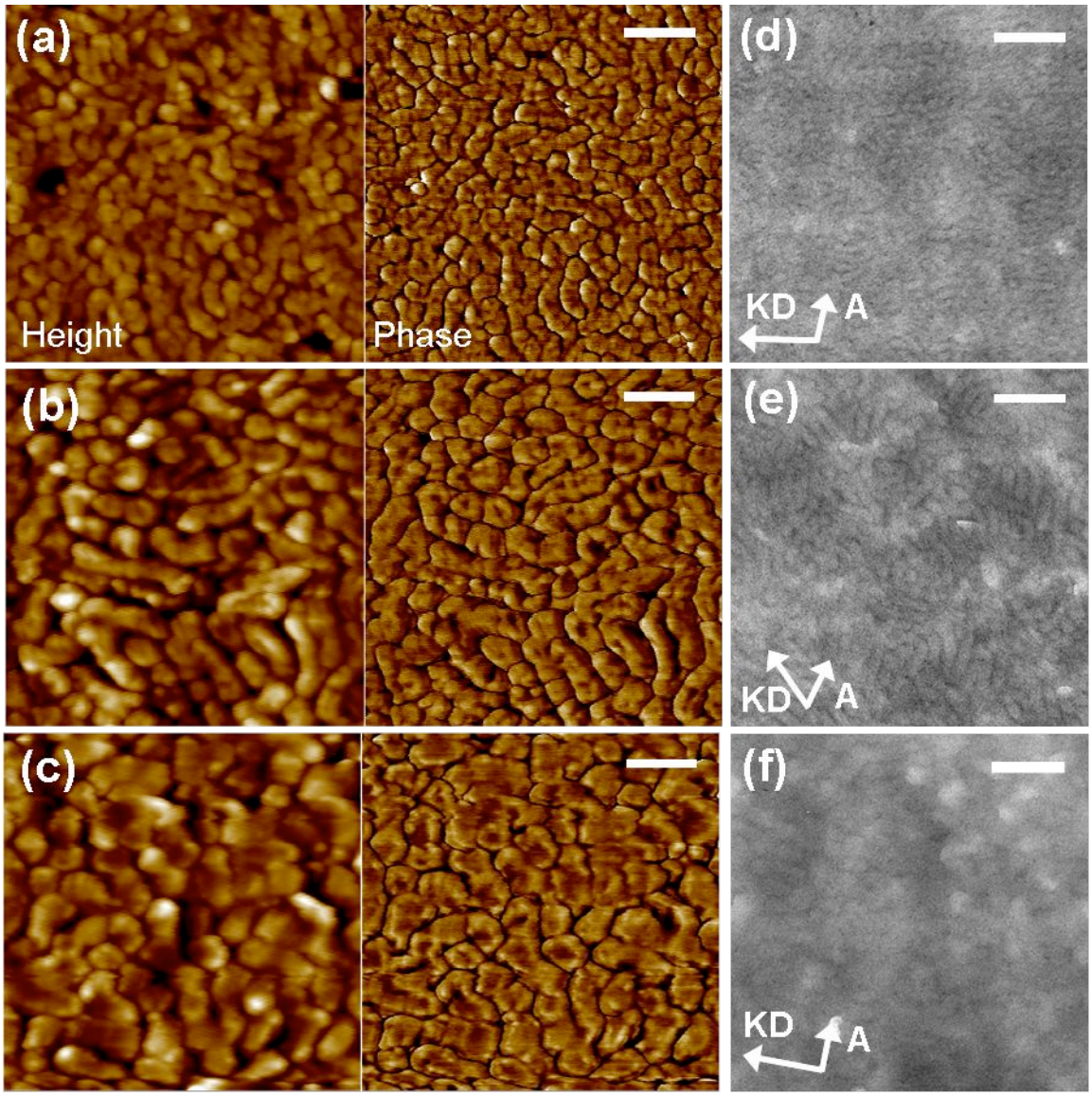

Figure 4.4. AFM and TEM micrographs of BPSH100-BPS0 membranes with hexafluorobenzene linkages and equal block lengths. AFM micrographs: (a) 5k-5k, (b) 10k-10k, (c) 15k-15k; Setpoint ratios: 0.78, 0.85, 0.86; Z ranges: 20 nm, 25°. TEM micrographs: (d) 5k-5k, (e) 10k-10k, (f) 15k-15k. "A" denotes direction of air side. "KD" denotes the knife direction during microtoming. Scale bars = 100 nm.

The phase separated morphologies of the surfaces of the copolymers are represented in the phase images of the AFM micrographs. It has been shown previously that adsorbed water on ion-rich regions of Nafion dampen the oscillation of an AFM cantilever, causing an observable phase shift [28]. Since the ionic domains of the membranes in this study have adsorbed water, the darker regions in the AFM phase images correspond to their aggregated ionic groups and the lighter regions to their hydrophobic backbones. The phase images in Figure 4.4a-c reveal that the degree of phase separation on the surface changes with block length. As block length increases from 5 to 15 kg/mol, the lighter hydrophobic domains appear to aggregate and increase in size. The darker ionic domains appear to increase in length, especially from 5 to 10 kg/mol. This increase in domain size with block length can also be observed in the TEM images for this series (Figure 4.4d-f). The lighter hydrophobic domains appear as slightly elongated circles with diameters roughly around 14 nm in the 5k-5k copolymer (Figure 4.4d), then elongate and enlarge to a width of around 20 nm in the 10k-10k copolymer (Figure 4.4e), finally enlarging to a width of approximately 24 nm in the 15k-15k copolymer (Figure 4.4f). This increase in domain size with block length is expected for block copolymers and has been observed previously for multiblock copolymers containing BPSH100 blocks [12, 13]. Like domain size, the water uptake and proton conductivity values for these copolymers (Table 4.1) also increase with block length. These trends match those observed for other BPSH100-containing multiblock copolymers [23].

Table 4.1. Proton conductivities and water uptake values of BPSH100-BPS0 membranes with HFB linkages

Sample	I.V.[a] (dL/g)	IEC[b] (meq./g)	Water Uptake (%)	Proton Conductivity (S/cm)[c]
5k-5k	0.62	1.30	35	0.080
10k-10k	0.76	1.38	68	0.100
15k-15k	0.94	1.40	79	0.110

[a]Determined in NMP at 25 ºC with 0.05 M LiBr
[b]Ion Exchange Capacity determined by titration
[c]Measured at 30 ºC in DI water

Images of the surface morphologies of the BPSH100-BPS0 multiblock copolymer series with DFBP linkages and equal block lengths are presented in Figure 4.5.

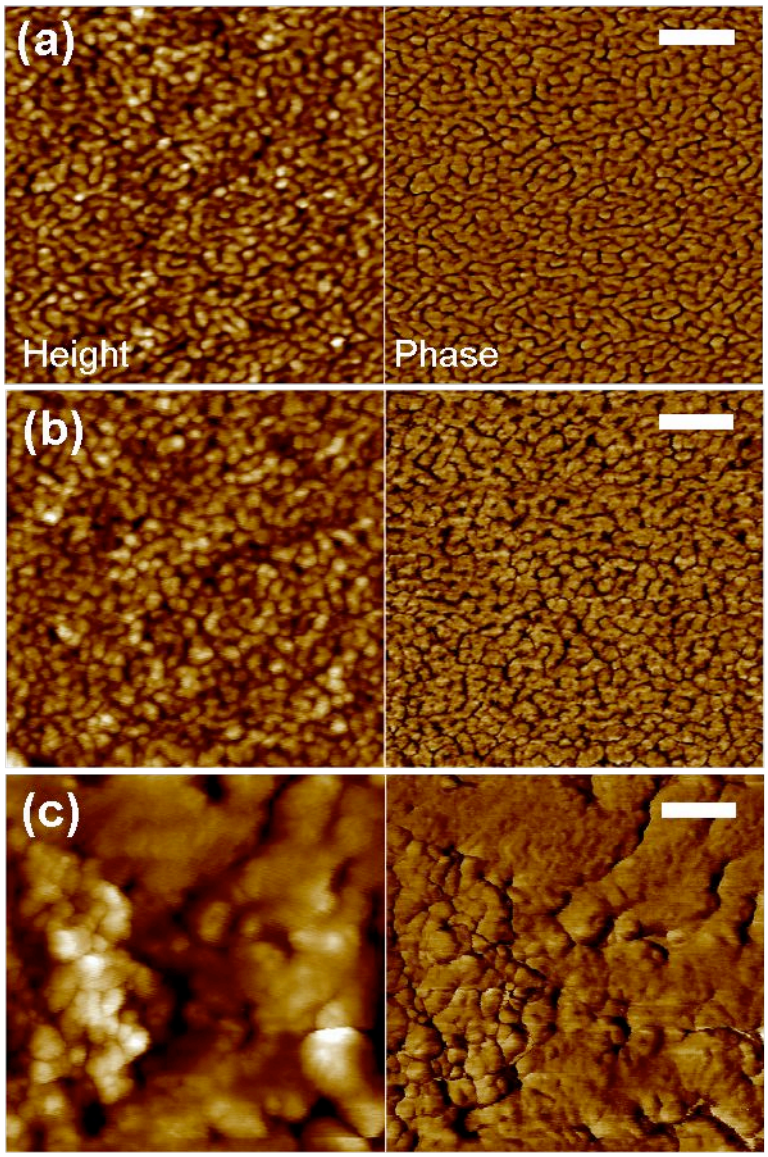

Figure 4.5. AFM micrographs of BPSH100-BPS0 membranes with decafluorobiphenyl linkages and equal block lengths: (a) 3k-3k, (b) 5k-5k, (c) 10k-10k; Setpoint ratios: 0.91, 0.95, 0.89; Z ranges: 12, 12, 25 nm and 30°. Scale bars = 100 nm

The phase images in Figure 4.5 show that unlike the multiblock copolymers with HFB linkages, the copolymers with DFBP linkages do not entirely display surface morphologies whose degree of phase separation changes proportionally with block length. Phase separation can be clearly observed in both the 3k-3k and 5k-5k copolymers. The sizes of both the lighter hydrophobic and darker hydrophilic regions appear to increase slightly as block length increases from 3 to 5 kg/mol. This increase in domain size is paralleled by an increase in the size of the topographical features in the height images. This trend does not appear to persist as block length

increases to 10 kg/mol (Figure 4.5c). The morphology of the 10k-10k copolymer does not even resemble that of the 5k-5k copolymer. There appears to be a disproportionately larger amount of lighter hydrophobic regions than darker ionic regions and they are far more continuous than the ionic regions, suggesting that phase separation may not be as good in the 10k-10k sample as the other two.

Transmission electron microscopy (TEM) performed on the 10k-10k sample showed just the opposite, however (Figure 4.6). The ionic groups of the multiblock copolymer appear to have phase separated into a cocontinuous morphology. Unfortunately, the morphologies of the 3k-3k and 5k-5k multiblock copolymers were not able to be resolved sufficiently by TEM to compare with the 10k-10k bulk morphology. Even without micrographs of the other samples in the series, the 10k-10k copolymer micrograph still yields important information when compared to the TEM micrograph of the HFB-containing copolymer with the same block lengths in Figure 4.4e. Both multiblock copolymers were synthesized from the same oligomers, yet the 10k-10k copolymer with HFB linkages in Figure 4.4e possesses a far less developed nanophase bulk morphology than the 10k-10k copolymer with DFBP linkages in Figure 4.6. This suggests that the higher fluorine content of the DFBP linkages compared to the HFB linkages may be responsible for increased phase separation within the DFBP-containing membranes.

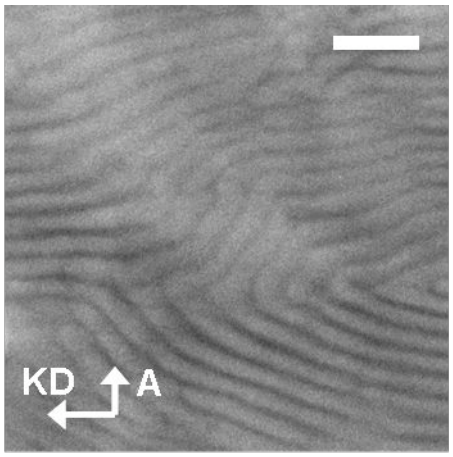

Figure 4.6. TEM micrograph of 10k-10k BPSH100-BPS0 membrane with decafluorobiphenyl linkages. "A" denotes direction of air side. "KD" denotes the knife direction during microtoming. Scale bar = 100 nm.

The HFB- and DFBP-containing 10k-10k copolymers both have comparable IEC, proton conductivity, and water uptake values (Tables 4.1 and 4.2). The same can be said for the 5k-5k copolymers with HFB and DFBP linkages.

Table 4.2. Proton conductivities and water uptake values of BPSH100-BPS0 membranes with DFBP linkages

Sample	I.V.[a] (dL/g)	IEC[b] (meq./g)	Water Uptake (%)	Proton Conductivity (S/cm)[c]
3k-3k	0.78	1.33	30	0.065
5k-5k	1.01	1.39	33	0.088
10k-10k	0.68	1.28	60	0.095
10k-5k	0.94	1.83	100	0.160
15k-10k	0.97	1.71	90	0.140
20k-15k	1.12	1.71	70	0.120

[a]Determined in NMP at 25 ºC with 0.05 M LiBr
[b]Ion Exchange Capacity determined by titration
[c]Measured at 30 ºC in DI water

This suggests that while the type of linkage does appear to affect both the surface and bulk morphologies, these morphological changes do not appear to have an appreciable effect on proton conductivity at the block lengths tested. The reason for this may be in the way the measurements were made. The proton conductivity and water uptake measurements were made at fully hydrated conditions, while the AFM images of surface morphology were taken at partially hydrated conditions and the TEM images of bulk morphology were obtained in a vacuum. While each characterization technique provides valuable systematic data about the copolymer series, there is not perfect correspondence between the techniques because of the differences in hydration inherent in the measurements. This also offers an explanation for why the domain sizes in the TEM image of a copolymer appear smaller than the domain sizes in the AFM image of the same copolymer since the ionic domains can swell in the presence of water [29] and shrink in its absence.

In order to better compare surface and bulk morphologies, another series of BSPH100-BPS0 multiblock copolymers with DFBP linkages synthesized with slightly larger block lengths was characterized by AFM and TEM (Figure 4.7). Unlike the first series, these multiblock copolymers were synthesized with unequal block lengths, the hydrophilic BPSH100 oligomers being longer than the BPS0 oligomers. The two samples with the shortest block lengths, the 10k-5k (Figure 4.7a) and the 15k-10k (Figure 4.7b), appear to increase in degree of phase separation and domain size as block length increases. This trend of domain size increasing with block length does not appear to extend to the 20k-15k copolymer (Figure 4.7c). Just as in the previous DFBP-containing series, the phase separation of its surface morphology does not seem

greater than the phase separation of the rest of the series. This is not the case for the bulk morphology, though. TEM micrographs of the series (Figure 4.7d-f) clearly show the evolution of phase separated domains with block length, from small circles to more elongated domains to finally cocontinuous lamellae. Once again, as in the previous DFBP-containing series, there appears to be a difference in surface and bulk morphologies, especially for the 20k-15k copolymer.

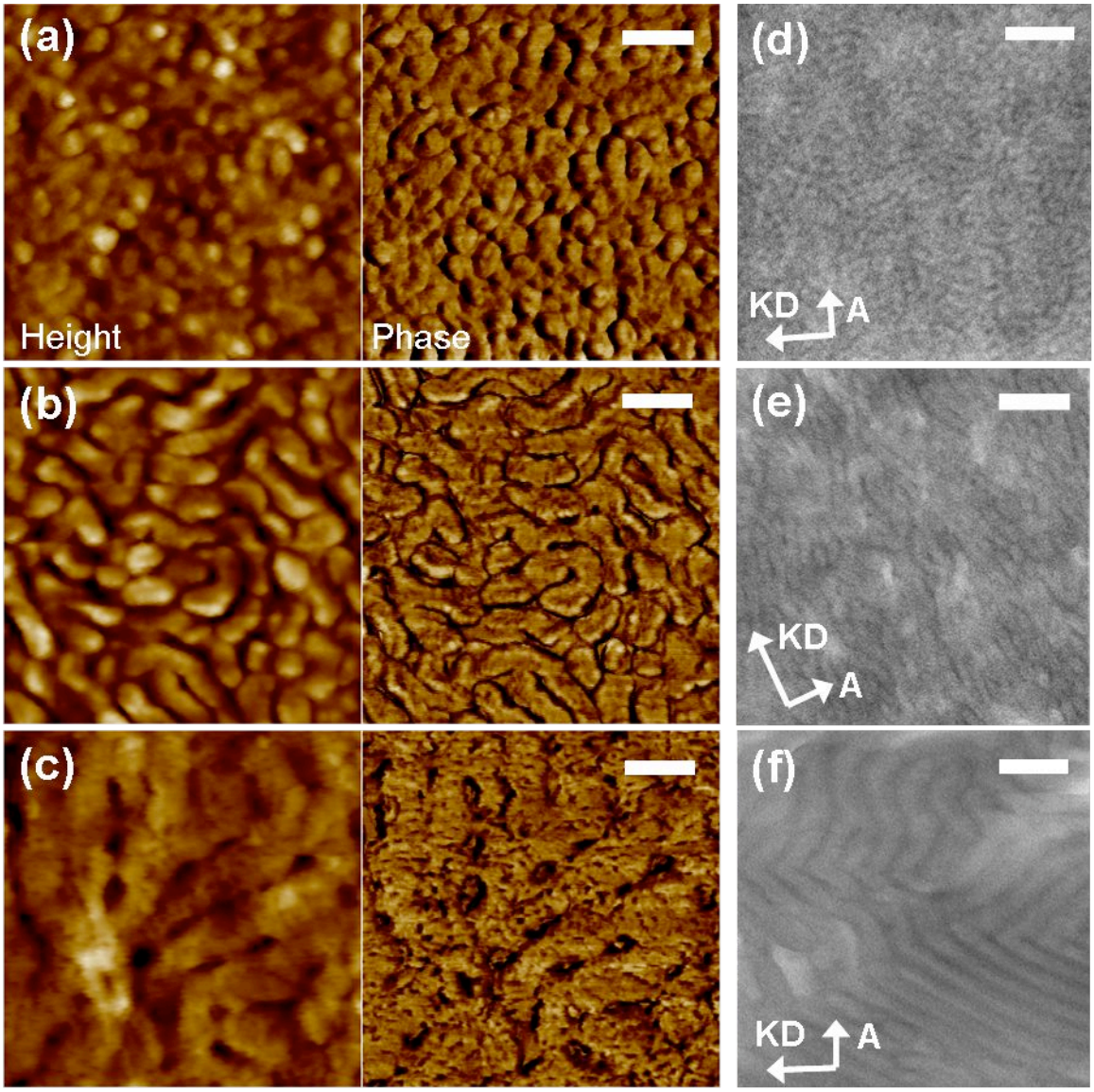

Figure 4.7. AFM and TEM micrographs of BPSH100-BPS0 membranes with decafluorobiphenyl linkages and unequal block lengths. AFM micrographs linkages: (a) 10k-5k, (b) 15k-10k, (c) 20k-15k; Setpoint ratios: 0.74, 0.90, 0.94; Z ranges: 25, 25, 45 nm and 30, 40, 20°. TEM micrographs: (d) 10k-5k, (e) 15k-10k, (f) 20k-15k. "A" denotes direction of air side. "KD" denotes the knife direction during microtoming. Scale bars = 100 nm.

4.3.2 Surface characterization

The question of why a discrepancy between the surface and bulk morphologies exists for the DFBP-containing multiblock copolymers but not the HFB-containing copolymers still lingered following morphological analysis by microscopy. Considering that the linkages are highly fluorinated, it was hypothesized that this observed discrepancy might be a result of surface enrichment of fluorine during membrane casting. It is well established in both diblock and triblock copolymers cast from hydrophobic solvents in air that the blocks with the lower surface energy migrate to the upper 50 Å (5 nm) of the membrane, resulting in concentration differences between the bulk and the surface [30, 31]. A surface enrichment of fluorine was observed by Ghassemi et al. [10] for multiblock copolymers with highly fluorinated blocks. It thus seemed plausible that the same phenomenon may be occurring with these low surface energy fluorinated linkage groups. Furthermore, the distance of 50 Å exactly matches the depth range (~0-5 nm) at which ionic domains can be reportedly sensed by a low oscillating AFM cantilever in tapping mode [29]. If the fluorine-rich DFBP linkages are migrating to the top 5 nm of the sample surface and suppressing the hydrophilic ionic domains to lower depths in the process, this would explain why less phase separation is observed in the AFM phase micrographs of the DFBP-containing copolymers than the HFB-containing copolymers. The low surface energy fluorine-containing DFBP linkages may be effectively displacing the higher surface energy ionic groups of the membrane out of the resolution range of the AFM.

To verify this hypothesis, x-ray photoelectron spectroscopy (XPS) was used to measure the fluorine contents of the two series of multiblock copolymers with equal block lengths. The results displayed in Table 4.3 show that the surface fluorine contents of the DFBP-containing copolymers are slightly larger than their theoretically calculated bulk fluorine contents, whereas the surface fluorine contents of the HFB-containing copolymers are about the same or a little less than their bulk fluorine contents. These data are consistent with the speculation that surface enrichment of fluorine is influencing surface morphology, however the values may be within the statistical error of the XPS measurements. The data also indicate that the amount of fluorine on the surface of the copolymers decreases with increasing block length. This is expected because the number of linkage molecules in a multiblock copolymer should decrease as block length (i.e. oligomer size) increases because there are fewer end groups present which can link together the macromolecule. The values in Table 4.3 represent fluorine atomic percentage values

corresponding to a depth of 5 nm obtained with an electron take-off angle of 45º. An angular dependence investigation would be of additional value in this study, but was not done here.

Table 4.3. Surface fluorine atomic percentage for BPSH100-BPS0 multiblock copolymers with DFBP and HFB linkages

	Fluorine atomic percentage			
	DFBP linkages		HFB linkages	
Sample	Air	Bulk[a]	Air	Bulk[a]
3k-3k	2.3	2.1		
5k-5k	1.6	1.5	0.9	0.7
10k-10k	1.1	1.0	0.3	0.5
15k-15k			0.4	0.46

[a]Calculated from the chemical structure.

4.3.3 Viscoelastic and mechanical property characterization

The 10k-10k copolymers with HFB and DFBP linkages were subjected to a single frequency temperature sweep by dynamic mechanical analysis (DMA) to evaluate if their different bulk morphologies might affect chain mobility and ultimately glass transition temperature. The results are presented in Figure 4.8. The storage modulus and tan delta curves for the two multiblock copolymers appear to virtually overlap, indicating that the type of linkage in these copolymers does not appear to impact their molecular relaxations and thermal transitions.

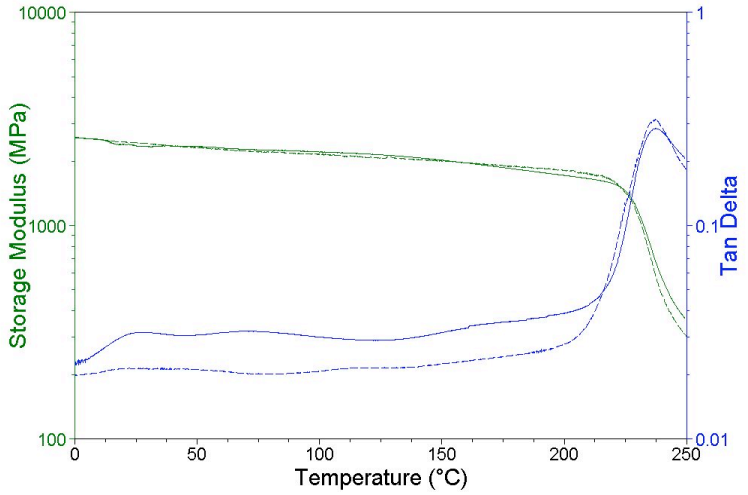

Figure 4.8. Storage modulus and tan delta curves for 10k-10k BPSH100-BPS0 multiblock copolymers. Solid line represents the HFB-containing copolymer and the dashed line represents the DFBP-containing copolymer.

Both HFB- and DFBP-containing multiblock copolymer series with equal block lengths were subjected to uniaxial tensile testing to compare the effects of linkage type on mechanical properties. The results for the 5k-5k and 10k-10k copolymers are presented in Table 4.4. Although the results for the two series are very similar, some small but real differences exist between them. The yield stress values suggest there is a real linkage-induced effect upon the mechanical properties of these BPSH100-BPS0 multiblock copolymers. The 5k-5k and 10k-10k copolymers with DFBP linkages appear to have 24% and 35% higher respective yield stress values than their counterparts with HFB linkages. Both 10k-10k copolymers have approximately the same intrinsic viscosity values, pointing to linkage type and not molecular weight as the potential cause of the higher values. Higher values for yield stress for the DFBP-containing copolymers agree with their more developed phase separation. The longer hydrophobic domains in the bulk of the copolymers are likely responsible for the small yet real increase in stiffness reflected in these data. The ultimate properties in the rest of the table are fairly similar between series with the exception of the break elongation. The 10k-10k copolymer with HFB linkages has an elongation to break twice as large as the copolymer with DFBP linkages. The average break elongation for the 5k-5k DFBP-containing copolymer is also lower than the break elongation for the HFB-containing copolymer, but this difference is not significant. The morphological differences between the two copolymers may also be responsible for these results. If this is the case, it appears that an increase in the amount of fluorination of a multiblock copolymer linkage molecule is accompanied by a modest increase in stiffness as well as a decrease in ductility.

Table 4.4. Ultimate mechanical properties of 5k-5k and 10k-10k BPSH100-BPS0 multiblock copolymers.

Sample	Apparent Young's Modulus (MPa)	Yield Stress (MPa)	Yield Elongation (%)	Stress at Break (MPa)	Elongation at Break (%)
5k-5k HFB	980 ± 160	34.0 ± 2.5	6.0 ± 0.6	43.2 ± 4.4	83.4 ± 17.9
10k-10k HFB	1320 ± 230	39.0 ± 1.5	6.8 ± 1.4	52.0 ± 9.5	95.8 ± 1.5
5k-5k DFBP	1450 ± 90	46.0 ± 2.0	7.0 ± 0.4	51.9 ± 7.5	61.7 ± 20.9
10k-10k DFBP	1480 ± 70	48.2 ± 1.8	6.4 ± 0.5	50.2 ± 5.7	40.5 ± 18.3

Testing performed at room temperature and 44-54% relative humidity

4.3.4 Water desorption behavior

Water desorption from BPSH100-BPS0 multiblock copolymers was measured by TGA to determine the effect, if any, the linkage-induced surface morphology differences have on water retention. Any changes in water retention that result from changes in surface hydrophobicity/hydrophilicity should be able to be quantified by TGA because it is very sensitive to changes in sample surface relative to sample volume [32]. The weight loss data obtained from the experiments were normalized by sample weight and ion exchange capacity and graphed as water molecules lost per ionic site versus temperature. Results for both linkage series with equal block lengths are depicted in Figure 4.9. The copolymers with DFBP linkages appear to lose slightly more water per ionic site than the ones with HFB linkages. There is also somewhat of an observable trend of water retention increasing with block length. This has been observed previously to a greater degree for another BPSH100-based multiblock copolymer system [33].

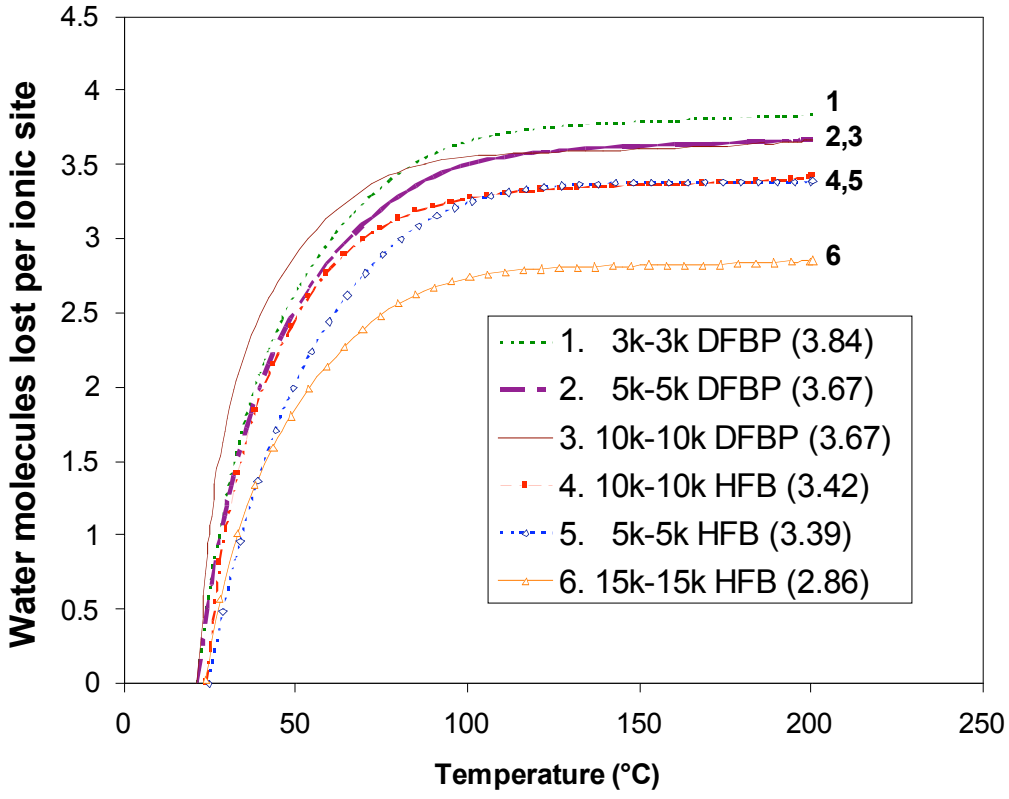

Figure 4.9. Water retention behavior of BPSH100-BPS0 multiblock copolymers of equal block lengths in terms of water molecules lost per ionic site at a constant heating rate of 2.5 °C/min. Numbers in parentheses denote number of molecules lost per ionic site at 200 °C.

Following the temperature ramp to 200 ºC shown in Figure 4.9, the multiblock copolymer samples were kept at 200 ºC for one hour to evaluate the effect of linkage type on water desorption at sustained elevated temperature. The number of water molecules lost per ionic site at the beginning and end of the isotherm for the 5k-5k and 10k-10k copolymers are presented in Figure 4.10. During the isotherm, just as during constant heating, the DFBP-containing copolymers appear to lose more water than the HFB-containing copolymers, suggesting as before that linkage type has some effect on the water retention ability of these multiblock copolymers.

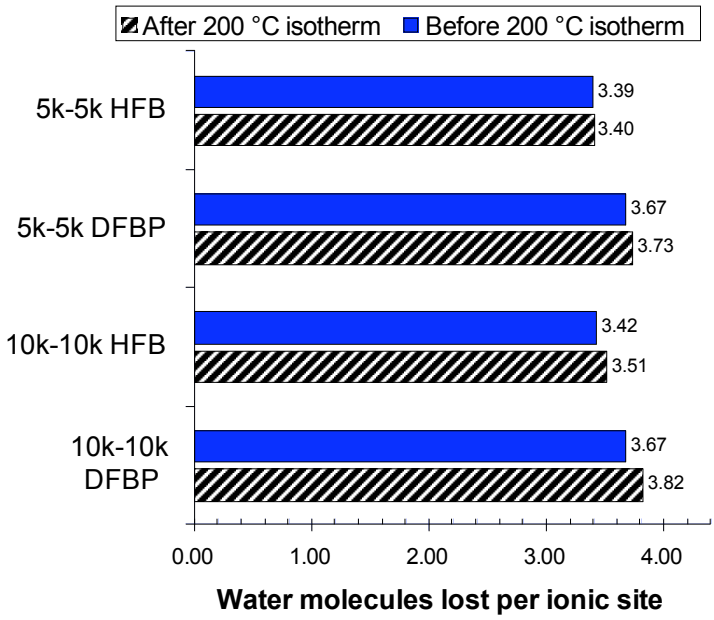

Figure 4.10. Graph of water loss as a function of block length and linkage type during 1 h at 200 °C

It is speculated that the results in Figures 4.9 and 4.10 are the result of the increased fluorine content of the surface of the DFBP-containing copolymers. Water is less likely to hydrogen bond with the hydrophobic fluorine units, leading to its increased desorption from surfaces as the degree of fluorination increases. This decrease of water on the surfaces of a DFBP-containing membrane may establish a decreasing gradient of water content from the bulk to the surface of the membrane larger than the gradient that may exist in a HFB-containing membrane. The result would be an increased driving force for mass transport of water from the more fluorinated membrane as temperature increases. For the block lengths tested here, it appears that linkage type may have a small effect on the water desorption of BPSH100-BPS0 multiblock copolymers. Conclusions drawn from these TGA data must remain tentative at

present since they reflect only one replicate for each sample and not an average of several replicates. Additional study with more sample replicates and a wider range of block lengths and linkages would probably clarify the extent of this effect. Whether this effect has any measurable consequence on the fuel cell performance of these membranes also remains to be seen.

4.4 Proton conductivity vs. relative humidity

After all the characterizations described above were performed, it was still unclear as to why the conductivities of the 10k-10k multiblock copolymers with different linkages were virtually the same despite the very different phase separated morphologies observed for the two copolymers. As stated earlier, the lack of correlation between conductivity and morphology was hypothesized to be because conductivity measurements were conducted at fully hydrated conditions and microscopy images were taken at partially hydrated conditions. Consequently, it was reasoned that conductivity measurements taken at partially hydrated conditions might better correlate with the differences observed by microscopy at partially hydrated conditions. Figure 4.11 displays a graph of proton conductivity versus relative humidity at 80 ºC for the two 10k-10k multiblock copolymers with different linkage groups. The graph indicates that at around fully hydrated conditions (95% RH), the conductivities of the two multiblock copolymers are virtually identical. As relative humidity decreases, however, the multiblock copolymer with DFBP linkages appears to display better proton conductivity than the copolymer with HFB linkages. It is speculated that the increased degree of phase separation in the DFBP-containing multiblock copolymer enables better conduction of protons at 80 ºC because the ionic domains through which the protons travel are less tortuous than the ones in the HFB-containing multiblock copolymer. These data along with the water desorption data suggest that BPSH100-BPS0 multiblock copolymers with both DFBP and HFB linkages are good candidates for MEA fabrication and evaluation in a fuel cell test stand to further determine how linkage type affects fuel cell performance both at partially hydrated and elevated temperature conditions.

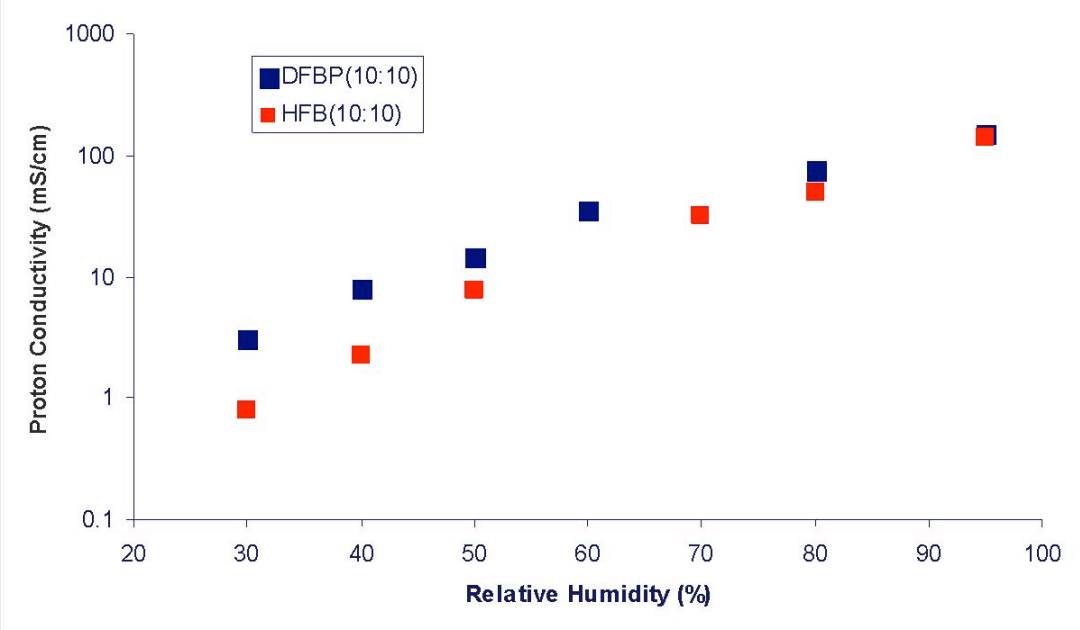

Figure 4.11. Graph of proton conductivity vs. relative humidity at 80 ºC for 10k-10k BPSH100-BPS0 multiblock copolymers with DFBP and HFB linkage groups

4.5 Conclusions

The choice of linkage type between hexafluorobenzene (HFB) and decafluorobiphenyl (DFBP) appears to have an influence on the phase separated morphologies of BPSH100-BPS0 multiblock copolymers. The degree of phase separation in the bulk morphologies of all the series evaluated in this study appears to increase with block length as expected, but the same trend is not observed for surface morphologies. While a similar trend of increasing domain sizes is observed for the series with the HFB linkage, this does not appear to be the case for the series with the DFBP linkage. XPS data supports the idea that this disruption of surface morphology trending with block length is the result of fluorine enrichment of the surface, although the data are not statistically significant. The amount of fluorine in the HFB linkage is not sufficient to cause changes in the surface morphology, but the amount in the more highly fluorinated DFBP is. The linkage-induced differences in morphology do not appear to affect the in-plane conductivity measurements taken of the membranes. This lack of correspondence between the microscopy and conductivity data is attributed to the differences in hydration during the measurements and the ability of ionic domains to change size with hydration. More study is

required to determine if the linkage-induced differences in morphology may influence the through-plane conductivity occurring in an actual fuel cell.

The different linkages do not appear to have any appreciable effect upon the thermal transitions of the BPSH100-BPS0 multiblock copolymers but they do influence mechanical properties. DMA curves of the two different series indicate that glass transition varies very little as a function of linkage type. Mechanical testing data reveals that an increase in the amount of fluorination of a multiblock copolymer linkage is accompanied by a modest increase in stiffness as well as a decrease in ductility.

Water desorption studies suggest that the ability of the BPSH100-BPS0 multiblock copolymers to retain water at elevated temperatures may be influenced by linkage type. When heated from room temperature to 200 °C, the copolymers with the HFB linkage appear to retain slightly more water than the copolymers with the DFBP linkage. Data from an isotherm at 200 °C suggests that the HFB series also loses less moisture than the DFBP series at sustained elevated temperature.

Proton conductivity data at partially hydrated conditions indicate that linkage type affects proton conductivity at low relative humidities. The DFBP linkage appeared to enable higher proton conductivity at partially hydrated conditions than the HFB linkage. These conductivity results may be a function of the increased nanophase separation induced by the more fluorinated DFBP linkage.

4.6 Future Work

In situ studies of multiblock copolymer membranes in an actual fuel cell are required to further elucidate the degree to which these linkage-induced effects impact fuel cell performance. These studies currently being investigated in our laboratory and will be discussed in a future publication.

4.7 Acknowledgements

The authors wish to thank the National Science Foundation “Partnership for Innovation” Program (HER-0090556) and IGERT Program (DGE-0114346), the Department of Energy (DE-FG36-06G016038), and the Nissan Motor Company for supporting this research.

4.8 References

1. Winter, M. and R.J. Brodd, *What are batteries, fuel cells, and supercapacitors?* Chemical Reviews, 2004. **104**(10): 4245-4269.

2. Perry, M.L. and T.F. Fuller, *A historical perspective of fuel cell technology in the 20th century.* Journal of the Electrochemical Society, 2002. **149**(7): S59-S67.

3. Hickner, M.A., H. Ghassemi, Y.S. Kim, B.R. Einsla, and J.E. McGrath, *Alternative polymer systems for proton exchange membranes (PEMs).* Chem. Rev., 2004. **104**(10): 4587-4611.

4. Hamrock, S.J. and M.A. Yandrasits, *Proton exchange membranes for fuel cell applications.* Polym. Rev., 2006. **46**(3): 219-244.

5. Miyatake, K. and M. Watanabe, *Recent progress in proton conducting membranes for pefcs.* Electrochem., 2005. **73**(1): 12-19.

6. Alberti, G. and M. Casciola, *Composite membranes for medium-temperature PEM fuel cells.* Ann. Rev. Mat. Res., 2003. **33**: 129-154.

7. Roziere, J. and D.J. Jones, *Non-fluorinated polymer materials for proton exchange membrane fuel cells.* Ann. Rev. Mat. Res., 2003. **33**: 503-555.

8. Savadogo, O., *Emerging membranes for electrochemical systems: (I) solid polymer electrolyte membranes for fuel cell systems.* J. New Mater. Elect. Sys., 1998. **1**(1): 47-66.

9. Lee, H.S., A. Roy, A.S. Badami, and J.E. McGrath, *Synthesis and characterization of sulfonated poly(arylene ether) polyimide multiblock copolymers for proton exchange membranes.* Macromolecular Research, 2007. **15**(2): 160-166.

10. Ghassemi, H., J.E. McGrath, and T.A. Zawodzinski, *Multiblock sulfonated-fluorinated poly(arylene ether)s for a proton exchange membrane fuel cell.* Polymer, 2006. **47**(11): 4132-4139.

11. Ghassemi, H., G. Ndip, and J.E. McGrath, *New multiblock copolymers of sulfonated poly(4 '-phenyl-2,5-benzophenone) and poly(arylene ether sulfone) for proton exchange membranes. II.* Polymer, 2004. **45**(17): 5855-5862.

12. Lee, H.-S., A. Roy, A.S. Badami, and J.E. McGrath, *Segmented sulfonated poly(arylene ether sulfone)-b-polyimide copolymers for proton exchange membrane fuel cells. I. Copolymer synthesis and fundamental properties.* J. Polym. Sci. Part A: Polym. Chem., 2007. **45**: 4879-4890.

13. Wang, H., A.S. Badami, A. Roy, and J.E. McGrath, *Multiblock copolymers of poly(2,5-benzophenone) and disulfonated poly(arylene ether sulfone) for proton-exchange membranes. I. Synthesis and characterization.* J. Polym. Sci.: Part A: Polym. Chem., 2007. **45**(2): 284-294.

14. McGrath, J.E., *Progress in alternate proton exchange membrane materials for fuel cells.* Abstracts of Papers, 234th ACS National Meeting, Boston, MA, United States, August 19-23, 2007, 2007: POLY-068.

15. Yu, X., A. Roy, and J.E. McGrath, *Perfluorinated-sulfonated hydrophobic-hydrophilic multiblock copolymers for proton exchange membranes (PEMs).* PMSE Preprints, 2006. **95**: 141-142.

16. Li, Y., A. Roy, A.S. Badami, M. Hill, J. Yang, S. Dunn, and J.E. McGrath, *Synthesis and characterization of partially fluorinated hydrophobic–hydrophilic multiblock copolymers containing sulfonate groups for proton exchange membranes.* J. Power Sources, 2007. **172**(1): 30-38.

17. Roy, A., M.A. Hickner, X. Yu, Y.X. Li, T.E. Glass, and J.E. McGrath, *Influence of chemical composition and sequence length on the transport properties of proton exchange membranes.* J. Polym. Sci.: Part B: Phys, 2006. **44**(16): 2226-2239.

18. Roy, A., M.A. Hickner, H.-S. Lee, A. Badami, X. Yu, Y. Li, T. Glass, and J.E. McGrath, *Transport properties of proton exchange membranes.* ECS Transactions, 2007. **2**(24, Direct Methanol Fuel Cells): 45-54.

19. Roy, A., X.A. Yu, A. Badami, and J.E. McGrath, *Multiblock hydrophilic-hydrophobic proton exchange membranes for fuel cells.* Abstracts of Papers of the American Chemical Society, 2006. **231**.

20. Noshay, A. and J.E. McGrath, *Block copolymers: Overview and critical survey*. 1977, New York: Academic Press. 516.

21. Leibler, L., *Theory of microphase separation in block copolymers.* Macromolecules, 1980. **13**(6): 1602-1617.

22. Bates, F.S. and G.H. Fredrickson, *Block copolymers - designer soft materials.* Physics Today, 1999. **52**(2): 32-38.

23. Badami, A.S., H.-S. Lee, Y. Li, A. Roy, H. Wang, and J.E. McGrath, *Molecular weight effects upon poly(arylene ether sulfone)-based random and multiblock copolymers for fuel cells.* Polymer, 2008: *submitted*.

24. Roy, A., H.-S. Lee, A. Badami, and J.E. McGrath, ECS Transactions, 2007: *submitted*.

25. Lee, H.-S., A. Roy, O. Lane, S. Dunn, and J.E. McGrath, *Hydrophilic-hydrophobic multiblock copolymers based on poly(arylene ether sulfone) via low temperature coupling reactions for proton exchange membrane fuel cells.* Polymer, 2008: *submitted*.

26. Kim, Y.S., F. Wang, M. Hickner, S. McCartney, Y.T. Hong, W. Harrison, T.A. Zawodzinski, and J.E. McGrath, *Effect of acidification treatment and morphological stability of sulfonated poly(arylene ether sulfone) copolymer proton-exchange membranes for fuel-cell use above 100 degrees c.* J. Polym. Sci.: Part B: Phys, 2003. **41**(22): 2816-2828.

27. Yang, J., Y. Li, X. Yu, H. Wang, K.B. Wiles, M. Hill, H.-S. Lee, and J.E. McGrath, *Viscometric behavior and molecular weight characterization of sulfonated poly(arylene ether sulfone) copolymers.* Abstracts of Papers of the American Chemical Society, 2005. **230**: U1689-U1689.

28. James, P.J., M. Antognozzi, J. Tamayo, T.J. McMaster, J.M. Newton, and M.J. Miles, *Interpretation of contrast in tapping mode AFM and shear force microscopy. A study of Nafion.* Langmuir, 2001. **17**(2): 349-360.

29. McLean, R.S., M. Doyle, and B.B. Sauer, *High-resolution imaging of ionic domains and crystal morphology in ionomers using AFM techniques.* Macromolecules, 2000. **33**(17): 6541-6550.

30. Thomas, H.R. and J.J. O'Malley, *Surface studies on multicomponent polymer systems by x-ray photoelectron-spectroscopy - polystyrene - poly(ethylene oxide) diblock copolymers.* Macromolecules, 1979. **12**(2): 323-329.

31. O'Malley, J.J., H.R. Thomas, and G.M. Lee, *Surface studies on multicomponent polymer systems by x-ray photoelectron-spectroscopy - polystyrene poly(ethylene oxide) triblock copolymers.* Macromolecules, 1979. **12**(5): 996-1001.

32. Hatakeyama, T. and F.X. Quinn, *Thermal analysis: Fundamentals and applications to polymer science*. 1994, New York: John Wiley & Sons. 158.

33. Badami, A., A. Roy, H.-S. Lee, Y. Li, and J.E. McGrath, *Morphological investigations of disulfonated poly(arylene ether sulfone)-b-naphthalene dianhydride-based polyimide multiblock copolymers as potential high temperature proton exchange membranes.* J. Memb. Sci., 2008: *submitted*.

Recommendations for Future Research

Currently, direct correlations between microscopy images of PEM morphology and proton conductivity are difficult to make because of the difference in hydration levels between conductivity testing and microscopy imaging. Conductivity tests are either performed in liquid water or at fixed relative humidities. In contrast, TEM imaging is performed in a vacuum and AFM imaging is either done in pure liquid or at ambient humidity. While little can be done to reduce the vacuum to which TEM samples are subjected, it is possible to change the atmosphere under which AFM operates. Given the increasing interest in operating PEM fuel cells at elevated temperatures and low relative humidities, it may be helpful to fabricate a humidity source which can be calibrated with precision to match the range of humidities at which conductivity testing is performed. This would enable better correspondence between morphology images and performance data. Currently NIST-traceable or equivalent humidifiers are not manufactured with outlet ports that can be connected to the commercially available environmental chamber hood for the AFM. A large chamber with a humidifier, fan, and control system would be required to supply a stream of humidified air to the samples.

AFM imaging of membrane cross-sections may be a helpful complement to TEM imaging, especially if humidity control is achieved with the AFM. This would allow imaging of the bulk of the membrane at controlled humidity levels that match the ones at which conductivity measurements are made. The membranes imaged by this method could conceivably be far more hydrated than TEM samples, providing a more accurate picture of PEM bulk morphology during testing or operation. The new microtome recently acquired by the university will facilitate sample preparation for this type of image much more than the previous microtome would. Care must be taken, however, to ensure that the microtoming process does not induce artifacts into the imaging surface. It is highly possible that the sample could be scraped by microscopic knife defects or hydrophilic domains compacted together during microtoming.

Small angle x-ray scattering (SAXS) would be an exceedingly beneficial complement to the current morphological characterization methods employed here and available on campus. Ionic block copolymer morphology has been shown in this dissertation and in our lab to be much more promising than random copolymer morphology in obtaining optimum PEM performance. SAXS would help very much to support microscopy characterization of PEMs. In particular,

SAXS may enable the analysis of the degree of phase separation of membranes at varying levels of hydration. This would permit analysis of samples equilibrated in a humidity oven, possibly bridging the gap between AFM images taken at ambient humidity and conductivity measurements in water without having to create a complex humidity apparatus for the AFM.

Previous attempts in our lab to characterize highly fluorinated random and multiblock copolymers by AFM have generated data which has primarily been inconclusive. The work in this dissertation has shed light on surface enrichment of fluorine as a possible reason for these results. It is recommended to use TEM as the primary microscopy technique for characterizing highly fluorinated multiblock copolymers, perhaps in conjunction with SAXS at different levels of hydration. This characterization approach may yield better information about the morphologies of our highest performing fluorinated multiblock copolymers, and help to clarify the relationships between ion exchange capacity, oligomer charge ratios and block lengths, and proton conductivity.

The effect of different casting methods for multiblock copolymers upon PEM performance properties should be investigated. Results in this dissertation suggest that PEM properties scale with morphology. Recent unpublished results obtained in our laboratory indicate that the choice of a different casting solvent can have a substantial influence on the bulk morphology of a multiblock copolymer. These results warrant further study into this area.

Although the data in this dissertation suggest the choice of linkage group will subtly affect the morphology, mechanical properties, and water retention properties of multiblock copolymer TEMs, it is still unclear whether these subtle changes will have any measurable effects on PEM performance in an actual fuel cell. MEAs should be fabricated from these multiblock copolymers with different linkage groups and their performance compared. The results of these tests may provide insight into preferred synthesis methods for multiblock copolymer PEMs in the future.

Appendix A: Standard Operating Procedure for Liquid Cell Attachment of the MultiMode Atomic Force Microscope

Prerequisites: Proficiency with the MultiMode AFM imaging in ambient conditions

Materials Required:

- Appropriate probe (tip) for liquid cell imaging. Veeco's model MPP-3100 has a sufficiently low spring constant (0.9 N/m) and a radius of curvature identical to the tips used for ambient imaging in the lab (<10nm)
- DI or HPLC water in a clean bottle (any foreign matter: dust, lint, etc. may be drawn into cell and catch on cantilever)
- Paper towels

Procedure:

1. Set up microscope for imaging with liquid cell.

    1.1 Place sample puck onto magnetic scanner base. Note that it may be advantageous to mount sample slightly off-center because the o-ring of the liquid cell is not centered in the cell.

    1.2 Align multimode head and sample so o-ring is aligned with the flat sample or its substrate (e.g. mica sheet) and the tip is over the desired region of the sample when liquid cell is inserted into multimode head.

    1.3 Mount tip into liquid cell.

    1.4 Manually lower tip towards surface to get very close without touching (judge by end of tip, not base of tip).

    1.5 Align laser and mirrors to maximize sum and positive RMS.

    1.6 Draw water into the liquid cell chamber without any leaks.

        1.6.1 Place open end of tubing attached to left side of liquid cell into bottle of DI water.

        1.6.2 Open BOTH clamps on tubing and pull syringe to draw water half-way up left side of tubing. ***IMPORTANT: Ensure clamp on tubing in water is open to prevent sucking tip into the sample surface.***

        1.6.3 Check for leaks by closing clamp on tubing with syringe and watching water level on left. If a leak is present, water will flow back into bottle. If leak

present, readjust o-ring relative to sample using knobs on base of multimode head and repeat step 1.6. If no leak present or water level dropping extremely slowly, proceed to step 1.7.

1.7 Realign laser and mirrors to maximize sum.

2. Manually Tune Cantilever

2.1 Click Tuning fork icon at top of screen.

2.2 Adjust parameters to display tip resonance peak.

2.2.1 Drive frequency = 8 kHz

2.2.2 Sweep width = 10 kHz

2.2.3 Data Scale = 0.5 V

2.3 Click "Center Peak" button under top display to center resonance peak.

2.4 Increase drive amplitude to increase peak size. Oscillation frequency of the tip may become audible as drive amplitude is increased.

2.5 Reduce sweep width value (~2 kHz) to isolate peak in display.

2.6 Set drive frequency just below resonance frequency.

2.6.1 Click "Offset" radio button in Cursor Mode box.

2.6.2 Click and drag cursor to desired resonance frequency left of the peak.

2.6.3 Click the "Execute" button in the Cursor Mode box.

2.7 Click "Zero Phase" under lower display to zero phase curve.

2.8 Click "Exit" button.

3. Set drive amplitude so RMS = 0.5 V. Oscillation frequency of tip will be audible.

4. Set initial gain settings.

4.1 Integral gain = 0.5

4.2 Proportional gain = 0.7

5. Engage tip to surface to begin imaging. The rest of the imaging procedure is identical to what is performed for ambient imaging. Be advised, however, that if the waveforms appear to drift continuously in one direction and it is difficult to obtain an image, it is likely that the sample has lifted from its substrate and is floating.

6. Shut-down

    6.1 Ensure both tubing clamps are closed.

    6.2 Ensure that tip is withdrawn and imaging is stopped. Withdraw tip if necessary.

    6.3 Place end of tubing on left side into a container for waste water.

    6.4 Disconnect syringe from tubing on right side and raise end of tubing above the level of the liquid cell.

    6.5 Open the clamp on the left side tubing.

    6.6 Open the clamp on the right side tubing while keeping the tubing elevated above the liquid cell. Immediately all the water in the tubing and the liquid cell should drain into the waster water container without any leaks.

    6.7 Remove liquid cell from the Multimode head and place in the proper storage location to dry. Only a single bead of water should remain on the sample after the liquid cell is removed.

    6.8 Remove water bead on sample with a Kim-wipe before removing sample puck from scanner.

Helpful tips:

- Lay tubing over top of multimode head so bubbles don't float up into the liquid cell.
- Always keep the clamps closed unless filling or emptying liquid cell. Closed clamps reduce the chance of leaking.
- If the vertical and horizontal values for the photodiode sensor are jumping around wildly when you are trying to zero them, the tip is too close to the surface. Lift the tip up and the values will stabilize.
- Be patient when zeroing the vertical and horizontal photodiode values. Always turn the knobs clockwise to increase the value and counter-clockwise to decrease the value regardless of what the fickle display reads. If you follow this rule of thumb, you will not have a problem getting a positive value for the sum.

Vita

Anand Shreyans Badami was born in the Lehigh Valley of Pennsylvania in the fall of 1977. He grew up there and graduated as valedictorian from Northampton Area Senior High School in 1995. Four years later he earned his Bachelor's degree in Chemical Engineering from Villanova University. After graduation Anand worked for Validation and Process Associates, Inc. in Willow Grove, PA as a consultant in the pharmaceutical industry. His passion for learning and science led him to enroll in the Macromolecular Science and Engineering Program at Virginia Polytechnic Institute and State University in the fall of 2002. During his first summer in graduate school, Anand worked at a research internship with 3M in St. Paul, MN as a 3M Engineering Scholar for 2003. In 2005 he earned his M.S. in Macromolecular Science and Engineering under Dr. Aaron Goldstein studying bioresorbable electrospun tissue scaffolds of poly(ethylene glycol-*b*-lactide) copolymers for bone tissue engineering. He then began working toward his Ph.D. in the same program under Dr. James E. McGrath. After graduation, Anand plans to work for the Dow Chemical Company in Midland, MI.